2013

Amorphous selenium (a-Se) gamma camera for image-guided breast brachytherapy

D'Angelo, Alexander Domenic

An amorphous selenium (a-Se) gamma camera for image-guided breast brachytherapy

By

ALEXANDER D'ANGELO

Master of Science in Physics

Lakehead University

Thunder Bay, Ontario

ProQuest LLC.
789 East Eisenhower Parkway
P.O. Box 1346
Ann Arbor, MI 48106 - 1346

An amorphous selenium (a-Se) gamma camera for image-guided breast brachytherapy

Abstract

In the current era of screening mammography, most women are diagnosed with localized, early-stage breast cancer. To avoid protracted radiation treatments and acute skin reactions associated with external-beam irradiation, a less traumatic brachytherapy technique, called Permanent Breast Seed Implantation (PBSI), was developed. This is a one-hour procedure where 60 to 80 radioactive ^{103}Pd seeds (21 keV) are implanted into the surgical cavity of the breast, delivering radiation only to the marginal tissue surrounding that region. A sensitive procedure like this requires an on-line imaging device to identify precisely the location of the seeds and evaluate the dose distribution so that deviations may be promptly corrected. Our approach is to use a gamma camera based on amorphous selenium (a-Se) since it provides high sensitivity at x-ray mammography energy, similar to that of ^{103}Pd and is more cost effective than alternative materials like CdZnTe. The objective is to evaluate the performance of an a-Se based gamma camera. The first stage involves simulating PBSI using GATE (Geant4 Application for Tomographic Emission), a software package offering an extensive physics library dedicated to numerical simulations in medical imaging and radiotherapy. The next step is to examine the efficacy of a-Se photoconversion when irradiated with a low energy gamma emitter. This is accomplished by pulse-height spectroscopy (PHS) experimentation using an ^{241}Am (60 keV) source with a 110 μm a-Se photoconductor target biased at 10-30 V/μm. Results from GATE demonstrate the proof-of-concept, that in 10 s, individual seeds placed 5 cm from the detector can be resolved to 1.3 mm accuracy. From PHS, ^{241}Am signal can be distinguished from background noise at fields 10V/μm and greater where the photoionization energy, $W_{\pm} < 41$ eV. Compton scattering is negligible in both simulation and experiment. In conclusion, a tuned gamma camera with a-Se photoconductor is able to accurately reconstruct positions of ^{103}Pd seeds for PBSI.

Acknowledgements

First and foremost, I wish to thank my supervisor, Alla Reznik and co-supervisor, Apichart Linhananta for the continuous support and motivation to my research; to Giovanni DeCrescenzo, Oleg Rubel and Aram Teymurazyan for the generous assistance in experiments and discussions of results; during his visit to Thunder Bay, Ananth Ravi, for presenting his work on brachytherapy and advice on simulation design. For computation, thanks to Darryl Willick for support in using the Lakehead University High Performance Computing Centre (LUHPCC). Finally, thanks to the advanced detection devices group at Thunder Bay Regional Research Institute (TBRRI) and the Physics Department of Lakehead University for the many engaging conversations and suggestions toward this project.

Table of Contents

List of Acronyms

ACS	American Cancer Society
ADC	analog-to-digital converter
CCD	charge-coupled device
CLHEP	class libraries for high energy physics
CMOS	complementary metal-oxide-semiconductor
CT	computed tomography
CS	cross-section
DOS	density of states
EHP	electron-hole pair
FOV	field of view
FPXI	flat-panel x-ray imager
FWHM	full-width at half-maximum
GATE	Geant4 application for tomographic emission
HDR	high-dose rate
HDRBB	high-dose rate breast brachytherapy
ITO	indium tin oxide
LDR	low-dose rate
LLD	low-level energy discriminator
LUHPCC	Lakehead University High-Performance Computing Centre
MC	Monte Carlo
MCA	multichannel analyzer

MRI	magnetic resonance imaging
NCD	National Cancer Database
PBSI	permanent breast seed implantation
PET	positron emission tomography
PHA	pulse-height analyzer
PHS	pulse-height spectroscopy
PMT	photomultiplier tube
RIL	resistive interface layer
RMSE	root-mean-square error
SI	Système International
SPECT	single-photon emission computed tomography
TFT-AMA	thin-film transistor active-matrix array
XRT	external-beam radiotherapy

List of Symbols

$D(r)$	dose of radiation at distance, r
λ	decay constant of a radionuclide
N_t	number of radionuclides after time, t
N_0	initial number of remaining radionuclides
$t_{1/2}$	half-life of radionuclide
e^-	an electron
ν_e	an electron neutrino
$E_{photoelectron}$	kinetic energy of photoelectron
E_γ	gamma photon energy
E_b	binding energy of orbital electron
σ_p	probability of photoelectric absorption process per unit distance
σ_c	probability of Compton scattering process per unit distance
Z	atomic number
$E_{scatter}$	kinetic energy of scattered photon
$m_e c^2$	rest mass energy of an electron
θ	scattering angle of a photon
μ	linear attenuation coefficient
$W_\pm$	photoconversion gain factor
l_{eff}	effective hole length of collimator
R_{sys}	system resolution of gamma camera

R_{int}	intrinsic resolution of detector
R_{coll}	collimator resolution
λ_m	mass attenuation coefficient
ρ	density of material
$\lambda_{photoelectric}$	mass attenuation coefficient for photoelectric absorption
$\lambda_{scattering}$	mass attenuation coefficient for Compton scattering
E_{eff}	effective energy of a radiation source
E_i	energy of i^{th} photon
y_i	yield of i^{th} photon
$\lambda(E)$	mean free path of a photon for a given energy, E
n_i	number of atoms per volume of i^{th} material
$\sigma(Z_i, E)$	cross-section of a process for atom, i, composing a material
v_{pp}	peak-to-peak voltage
n_o	number of electron-hole pairs
$\langle n_0 \rangle$	average number of electron-hole pairs
E_g	band gap energy
E_{ph}	phonon energy
σ^2	variance in number of electron-hole pairs
R_E	energy resolution of a detector
σ_0	total noise
σ_e	electronics noise
σ_i	intrinsic noise

n_c	number of electron-hole pairs which are created
n_r	number of electron-hole pairs which recombine
n_t	number of electron-hole pairs which are trapped
k_B	Boltzmann constant
E_a	activation energy to release a charge carrier from trap state

List of Figures

Chapter 1

Introduction to breast brachytherapy

1.1. Breast cancer

Breast cancer is one of the most commonly diagnosed cancers in women. Statistically speaking, it's estimated to occur in one out of every nine women and will claim the lives of 30% of those affected [1]. The American Cancer Society (ACS) estimates that this year in the United States: 232,340 new cases of invasive breast cancer will be diagnosed and 39,620 women will die from breast cancer [2]. With the advancement of screening mammography over recent years, there is a related demand for advanced medical technologies to help facilitate early breast cancer detection and treatment planning.

In the current era of screening mammography, most women are diagnosed with localized, early stage breast cancer [1]. Stages are ranked from 0 to 4 and determined based on the size of the tumor, whether or not the tumor has spread to the lymph nodes and whether the tumor has spread to distal parts of the body (metastasized). Stage 0 is associated with a pre-cancerous or marker condition. Stages 1–3 indicate the tumor is within the breast or regional lymph nodes and stage 4 is metastatic cancer in which the tumor has spread away from the breast and localized treatment is much less plausible. Larger tumors, nodal spread and metastasis are assigned a higher stage number and hence come with a worse prognosis.

Survival rates are often used by doctors as a standard way of discussing a patient's prognosis or outlook. The 5-year survival rate refers to the percentage of patients who live at least 5 years after being diagnosed, although many patients live much longer than this period. The data in Table 1.1 is from the *National Cancer Database* (*NCD*) for patients diagnosed in 2001 and 2002 [2]. These rates clearly indicate that as the cancer progresses, survival rate drops and successful treatment is less likely. In addition to screening for breast cancer in the early stages, treatment options must

be carefully chosen to ensure extended remission of the disease, and to retain the quality of life of the patient.

Table 1.1 5-year survival rates from the NCD, categorized by stage [2].

Breast Cancer Stage	5-year Survival Rate
0	93%
1	88%
2	81%
3	67%
4	15%

1.1.1. Localized treatment

The common methods used to treat breast cancer are surgery, radiation therapy and chemotherapy [3]. Local therapy is intended to treat a tumor on-site, without affecting the rest of the body. Surgery and radiation therapy are examples of local therapies. Since these treatments only target a specific region, there are no physiological side effects to the body as a whole, as opposed to chemotherapy, which can have several. Ideally, local treatment options are much more favorable to early stage cancer patients where the tumor is confined to a small area and has not metastasized.

Most women with breast cancer have some type of surgery. Many women at early-stage can choose between breast-conserving surgery and mastectomy (removal of entire breast). Approximately 60% of breast cancer patients are eligible for some form of breast-conserving surgery [2]. Lumpectomy is one type of procedure which removes only the breast lump and a surrounding "safety" margin of normal tissue, illustrated in Fig. 1.1. The main advantage is, of course, that the woman keeps most of her breast. How much is removed primarily depends upon the size and location of the tumor. A disadvantage is the usual need for radiation therapy, most often, for several weeks after surgery. For stages 1 to 3A breast cancer, a lumpectomy followed

by radiation therapy has the same survival rate as a mastectomy. Radiation therapy can sometimes be omitted as a part of breast-conserving therapy, but this is somewhat controversial. Furthermore, the NCD points out that the local cancer recurrence rate is 25% without radiation and only 5% with radiation [2]. Therefore, radiation therapy should always follow-up surgery to ensure long-term remission of breast cancer.

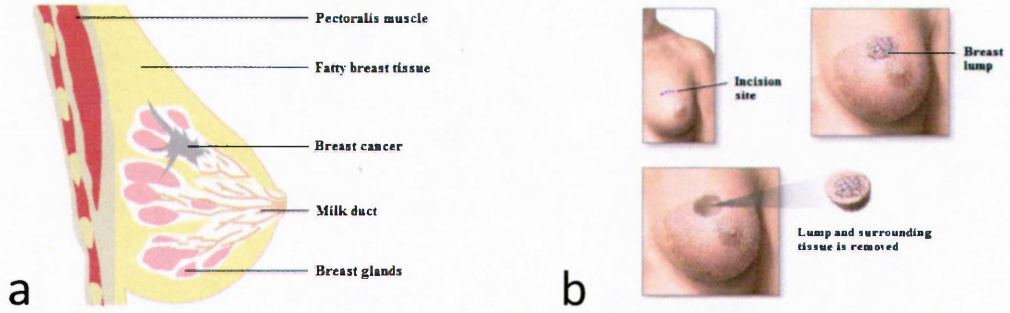

Figure 1.1 Anatomy of the breast with cancer (a) and the lumpectomy procedure (b), where the breast cancer lump is surgically removed (from A.D.A.M. Medical Encyclopedia).

1.1.2. Radiation therapy

Radiation to the breast is often given after breast-conserving surgery to help lower the chance that the cancer will come back in the breast or nearby lymph nodes. In general, radiation therapy uses high energy photons or particles with the intent of destroying cancer cells and eliminating their reproduction. The biological basis is that cancer cells can be killed by a delivery of high energy photons or subatomic particles (ie. a radiation dose). The intensity of this dose is sufficiently enough to ionize electrons in the cellular atomic structure, effectively destroying them entirely. Figure 1.2 shows this principle, demonstrating how a mammalian cell culture behaves when exposed to ionizing radiation. The most important target of the cell is the nuclear DNA, when damaged, will result in non-viable offspring [3]. It has also been shown that rapidly dividing cell populations like tumors, epithelial cells and blood cells, are the most sensitive to ionizing radiation. The amount of cellular damage is also dependent on the dose of radiation, that is, the energy absorbed per unit mass. The Système International (SI) unit for radiation dose is the Gray (Gy), where 1 Gy = 1 Joule per kilogram of matter [3].

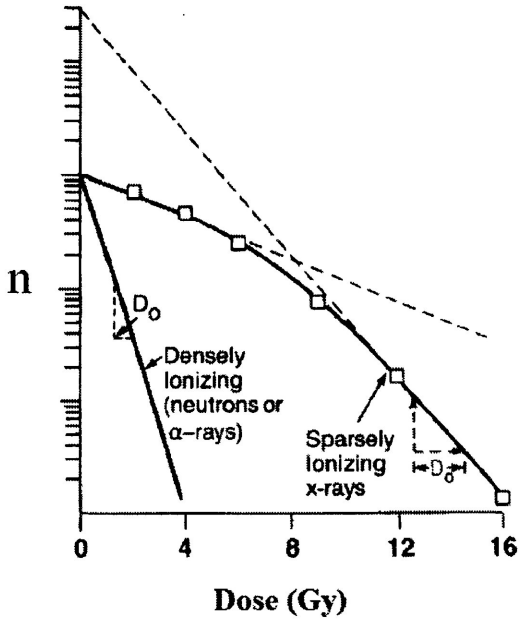

Figure 1.2 The typical survival curves for a culture of mammalian cells exposed to particle sources (neutrons or α-rays) and x-rays. The number of survivors (n), plotted on logarithmic scale, shows how radiation is less effective in killing cells at low doses because the cell is capable of repairing minor radiation damage. At higher doses, however, survival becomes exponential by a factor of 1/e for each dose increment of D_0 [3].

External-beam radiotherapy (*XRT*) is the most common type of radiation therapy administered to women with breast cancer. XRT is much like getting an x-ray, but the radiation intensity is much greater, since ionizing level radiation is required to destroy cancerous tissue. The radiation is focused from a machine outside the body on the area affected by the cancer. As in Fig. 1.3, this machine has a rotating "C-arm" which can focus the radiation beam in multiple orientations. The extent of radiation depends on whether mastectomy or lumpectomy was done and whether or not lymph nodes are involved. If mastectomy was done and no lymph nodes had cancer, radiation is targeted at the chest wall and the places where any drains exited the body. If lumpectomy was done, most often the entire breast gets radiation, and an extra boost of radiation is given to the area in the breast where the cancer was removed to prevent local recurrence. The boost is often given after the treatments to whole breast end. It uses the same machine, but the beams are directed to aim at the site where the cancer was surgically removed.

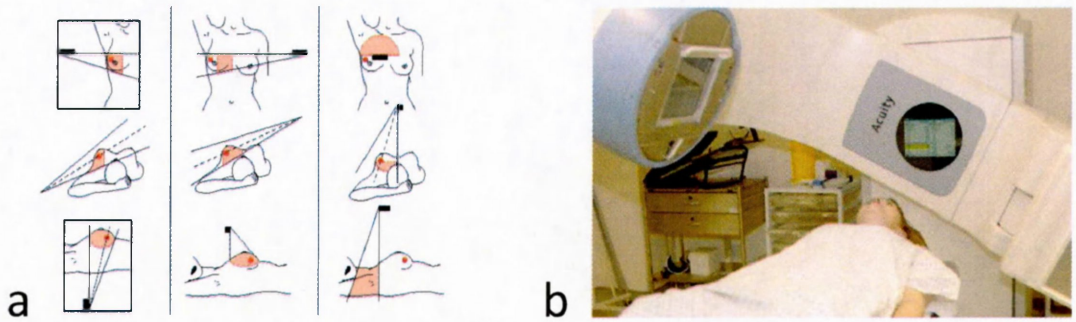

Figure 1.3 An XRT beam diagram (a) illustrates how the radiation can be targeted at the whole breast while focused on the tumor (in red) or lymph nodes. This is accomplished with a rotating C-arm (b) which can align in multiple orientations, utilizing either an x-ray or particle source emitter at one end, while the patient remains stationary.

The procedure itself is painless but the side effects following irradiation can be severe. Moreover, in order to spare normal tissue while destroying cancer cells, the radiation must be delivered in fractions over an extended period of up to 7 weeks [4]. The length of time required for XRT is difficult for some individuals and leads some to refuse XRT, increasing the risk of cancer recurrence. Furthermore, acute skin reactions are frequent, ranging from redness of the skin to a painful skin breakdown. This may result in the patient terminating treatment before an effective dose can be delivered, resulting in an incomplete recovery. Although XRT is the more conventional way to treat breast cancer via radiation, alternative methods such as brachytherapy have proven to be just as effective [4].

1.2. Brachytherapy

Brachytherapy, also known as internal radiation, is another way to deliver radiation therapy. Since it is much less disruptive to the patient, brachytherapy offers an effective alternative to XRT or may be used to add an extra boost of radiation along with XRT.

Initially, brachytherapy was used to solely treat prostate cancer but with new developments has expanded to effectively treat other cancers as well. The most common types of cancer that can be

treated with brachytherapy are: skin, cervical, prostate and breast. Brachytherapy procedures involve temporary placement of *high-dose rate* (*HDR*) radionuclides while others will suffice with *low-dose rate* (*LDR*) small radioactive pellets called *seeds*. The commonly used seeds in brachytherapy are ^{137}Cs, ^{60}Co, ^{192}Ir, ^{125}I, ^{103}Pd, *and* ^{106}Ru [5].

Instead of aiming radiation beams from outside the body, seeds are placed into the breast adjacent to the cancerous region. Their precise placement directly at the cancerous tissue site ensures highly localized target coverage. This results in a much quicker dose delivery, while minimizing unnecessary exposure of healthy regions of the body to harmful radiation. The sources are typically enclosed in a protective casing to deliver dosage to the area without risking the radioactive material to leak into the surrounding tissues. Additionally, the source is able to effectively irradiate the target area over the duration of the treatment since it moves with the organ or body part, whereas the patient would otherwise require precise repositioning each day for the 6 to 7 weeks of XRT. From Equation 1.1, radiation intensity far from an isotropic point source emission decays by the inverse square law [3]. That is, the dose, $D(r)$, is described by the radiation intensity (or number of photons per sec), over the surface area of an isotropic emission ($4\pi r^2$) at a distance, r from the source:

$$D(r)\,\alpha\,\frac{\#\ of\ photons/s}{4\pi r^2}\ \rightarrow\ \frac{D(r_1)}{D(r_2)}\,\alpha\,\frac{\frac{\#\ of\ photons/s}{4\pi {r_1}^2}}{\frac{\#\ of\ photons/s}{4\pi {r_2}^2}}\ \rightarrow\ \frac{D(r_1)}{D(r_2)}\,\alpha\,\left(\frac{r_2}{r_1}\right)^2 \qquad (1.1)$$

While the number of photons remains the same, the density changes as they diverge. Thus, the ratio of the dose at P_1/P_2 in Fig. 1.4 is proportional to the inverse squares of their distances from the source. Therefore, the radiation exposure away from the target volume is significantly reduced from that inside of the volume. In addition, the attenuation of the photons is highly dependent upon the surrounding medium, so by the time the radiation leaves the target volume, the dose would have been attenuated to levels where other parts of the patient and persons in proximity to the patient are at very low exposure.

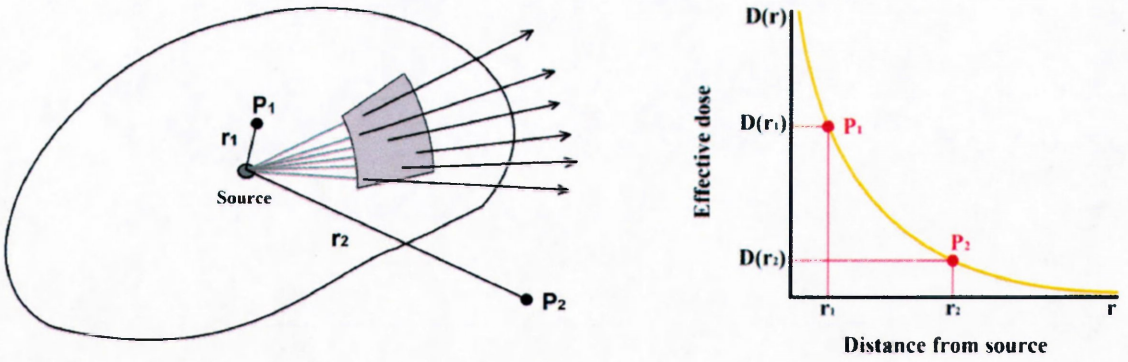

Figure 1.4 The left image illustrates the isotopic photon emissions from the brachytherapy source at two points: P_1 and P_2. At a distance, r, the effective dose, $D(r)$, decays by the inverse square law, shown graphically on the right.

1.2.1. Breast brachytherapy techniques

Breast brachytherapy offers a number of advantages over traditional XRT. At 5 to 7 days duration, HDR brachytherapy procedures are much quicker than 6 to 7 weeks of XRT, but they still require regular hospital visits and can be quite painful [5]. For example, in High Dose Rate Breast Brachytherapy (HDRBB) and Accelerated Partial Breast Irradiation (APBI) in Fig. 1.5, treatment catheters must be inserted into the breast in order to temporarily place the HDR seeds. If the seeds are temporary, the half-life and activity are not a major concern. However, if the seeds will be permanently implanted as in the next procedure, half-life must be short to ensure the patient will not remain radioactive for an extended period of time.

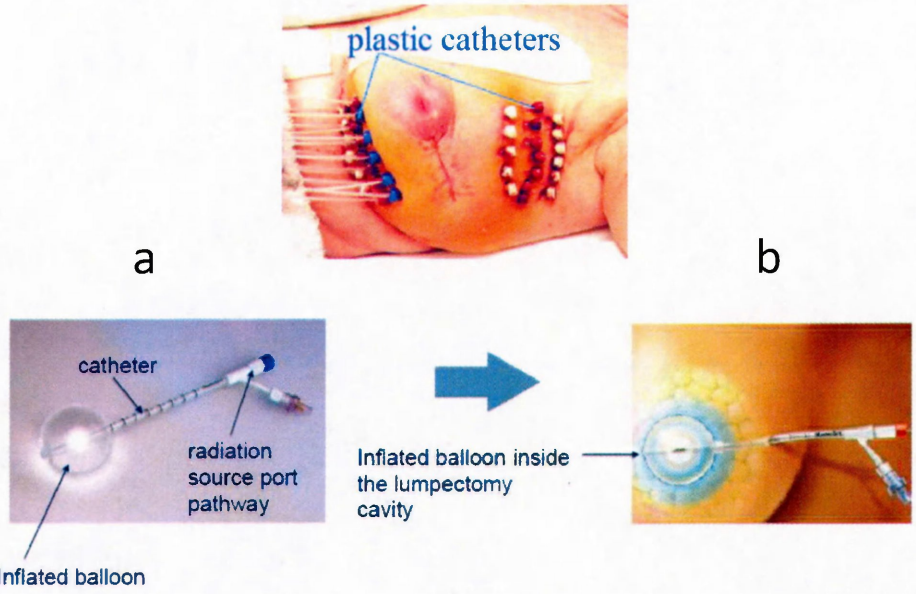

Figure 1.5 HDRBB (top image) involves placing multiple catheters through the breast, then injecting HDR seeds for temporary irradiation. APBI is another application of HDR breast brachytherapy which places a single catheter (a) into the lumpectomy cavity followed by the sources with irradiate from an inflated balloon, expanded to the size of the cavity (b).

1.2.2. Permanent breast seed implantation

To avoid protracted radiation treatments and acute skin reactions, a novel and much less traumatic brachytherapy technique, called *Permanent Breast Seed Implantation* (*PBSI*), was recently developed at Sunnybrook Health Sciences Centre [4]. This procedure is generally one-hour long and involves surgically implanting ^{103}Pd seeds into the surgical cavity of the breast. For breast application, ^{103}Pd is used over the traditional ^{125}I for prostate in which this procedure was initially developed for. With a relatively short half-life of 17 days and LDR of 21 keV at 2 mCi activity [4], ^{103}Pd can effectively deliver brachytherapy treatment while the seeds can permanently remain in the breast. Individual ^{103}Pd seeds, in Fig. 1.6, are approximately 5 mm by 0.8 mm in dimensions, enclosed in a titanium casing with central tungsten marker.

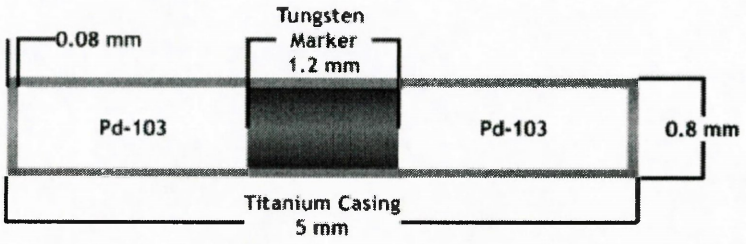

Figure 1.6 The physical dimensions and composition of a single ^{103}Pd seed [6].

Depending on different factors, between 50 and 100 seeds are used. Prior to the procedure, a CT simulation is required to define the extents of the target volume followed by the implantation procedure administered under local anaesthesia. Since the volume of normal tissue irradiated is greatly reduced from XRT, the dose can be delivered more rapidly. Seeds are placed in strands to avoid their motion since seed misplacement greater than 5 mm may lead to under dosage, putting the patient at increased risk of local recurrence. The radioisotope half-life is chosen so that radiation dose is delivered constantly. Thus, PBSI allows patients to be discharged home the same day after a single one-hour treatment session. This dramatically improves the quality of life of the patient during treatment over conventional XRT. Also, due to the low primary emission of the ^{103}Pd isotope, external radiation exposure to other parts of the body and other persons is acceptably minimal as the effective dose remains below 5 mSv (milliSieverts) [6]. The Gray and Sievert are both SI measurements of radiation dose, however, use of the Sievert implies that appropriate biological weighting factors have been applied to the original absorbed dose measurement (in Grays). Essentially, the Sievert is a corrected dose for the specific material which is irradiated [7].

Before the implantation is performed, there is a period of initial planning. This involves getting anatomical information of the breast using x-ray *computerized tomography* (*CT*). The first stage of implantation involves placing a localization, or fiducial, needle through a template into the surgical cavity, under ultrasound guidance. The fiducial needle allows passage of the brachytherapy needle for implanting linear strands of ^{103}Pd seeds into the breast. A post-implant quality assurance screening is then performed, to ensure seeds were positioned correctly. The seeds are delivered to locations within the patient that are fixed in 3D with respect to the location and orientation of the template. Since the template is fixed in space with respect to the anatomic

location for treatment, we simply need to ensure that we know the position of our imaging device with respect to the template in order to compare the planned locations of the seeds and the imaged locations of the seeds in the same space. The stages of the PBSI procedure are illustrated below in Fig. 1.7.

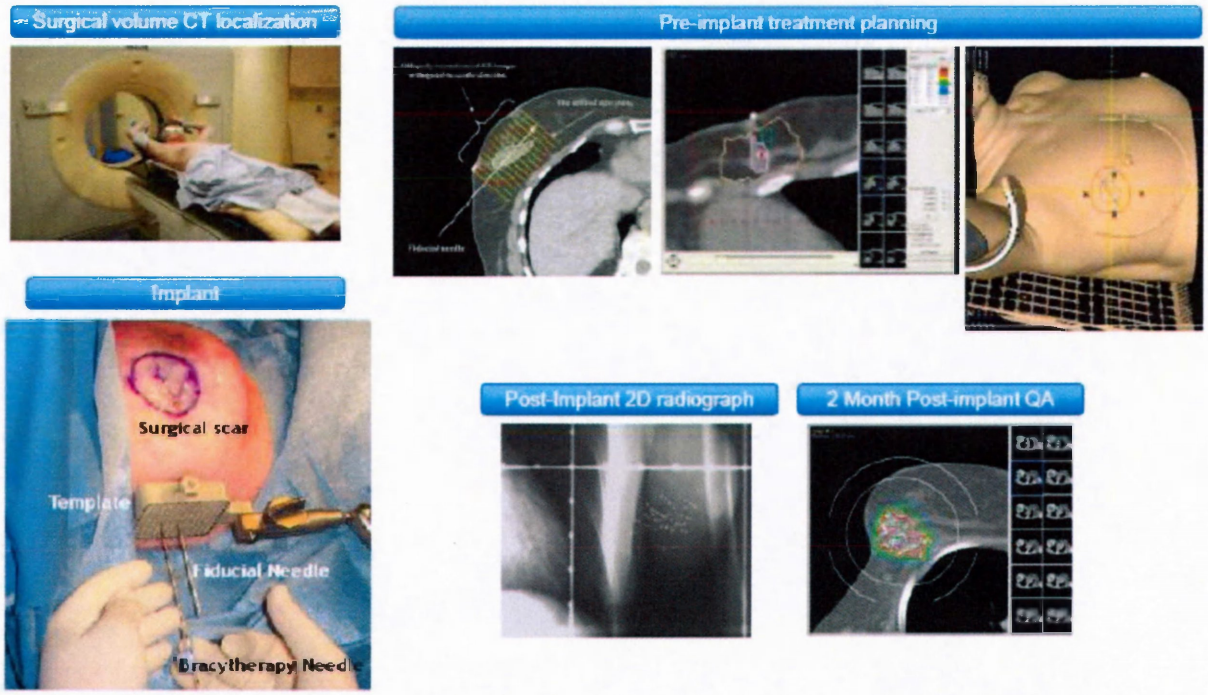

Figure 1.7 The PBSI procedure involves initial planning with CT information, followed by post-implant quality assurance screening. The setup for implantation uses a template for inserting the fiducial needle into the breast, which allows passage of the brachytherapy needle for implanting ^{103}Pd seeds in linear strands [4].

Although the high potential of PBSI has already been proven by clinical studies at Sunnybrook Health Sciences Centre, the limitation in the procedure is that an oncologist is unable to visualize the brachytherapy sources as they are being implanted [4]. This results in the inability for a real-time correction in the event that a seed has been incorrectly positioned. The radiograph in Fig. 1.8 is one such scenario where there is an area with too much irradiation and one with too little. Alternatively, we could call these regions a "hot-spot" and "cold-spot", respectively. Indeed, for one patient among twelve that have been treated with PBSI following breast-conserving surgery, the strands were placed too close to each other and the treated volume was much smaller than

planned [4]. Thus, there is a need for an on-line imaging device to identify precisely the location of the seeds and evaluate the dose distribution during and at the end of the implantation so that a deviation from the planned dose distribution can be corrected. This will ensure that PBSI consistently achieves appropriate target coverage, which translates to a higher cure rate for breast cancer patients.

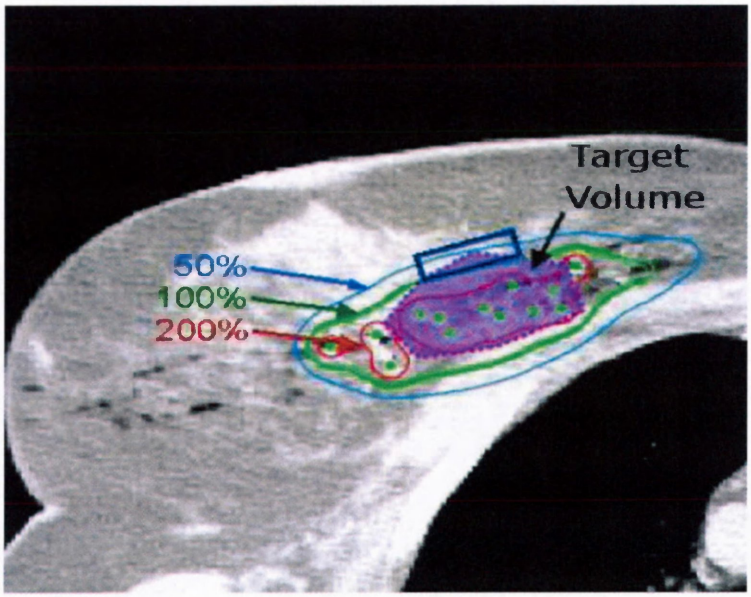

Figure 1.8 An example of inadequate target coverage in a CT image of the breast, demonstrating a "hot-spot" in red and a "cold-spot" in blue. The target volume should have at least 100% of the dose over the entire volume while maintaining the dose to the surrounding tissue at a minimum. This is quite a sensitive task as seeds cannot be removed once implanted [4].

1.3. Physics of brachytherapy

Since the radionuclide sources originate from inside the body (internal radiation), it is important to understand how the radiation behaves within an absorbing medium, so that the mechanisms of interaction may be accounted for. *Gamma-rays* (*γ-rays*) are emitted by a variety of radioactive materials, some of the better known being ^{60}Co and ^{137}Cs. *X-rays*, in contrast, are produced by radiation-producing machines via *Bremsstahlung* process. During the early years of radiography, the x-rays produced by machines were of lower energy than those of typical γ-rays. As machines capable of producing higher energy x-rays were developed, and as scientists gained a deeper

understanding of the full range of energies of the γ-rays emitted by radioactive materials, they realized that the energies of the two types have overlapped. For all intents and purposes, we will keep the γ-ray designation as those photons emitted from radionuclides by radioactive decay process.

A *radionuclide* is an atom with an unstable nucleus which spontaneously undergoes radioactive decay in order to become stable. Radioactive decay is a random process, however, every isotope of the same type of radionuclide has the same probability of undergoing decay at any given time. Therefore, the number of radioactive decays, *dN*, over time, *dt*, is proportional to the total number of radionuclides, *N*:

$$\frac{dN}{dT} = -\lambda N \tag{1.2}$$

where λ is the decay constant of that radionuclide [9]. By solving this differential equation, we acquire an exponential equation as follows:

$$N_t = N_0 e^{-\lambda t} \tag{1.3}$$

where N_0 is the initial number of radionuclides, and N_t is the number of remaining radionuclides after time, t [9]. In place of a decay constant, a radionuclide is more commonly characterized by its half-life, $t_{1/2}$, which is the time for 50% of the radionuclides to decay [9]:

$$t_{1/2} = \frac{\ln 2}{\lambda} \tag{1.4}$$

There are several decay methods which can occur, depending on the radionuclide. Electron capture is the decay mechanism of ^{103}Pd. In this process, a proton is converted into a neutron by capturing an orbital electron, thus resulting in ^{103}Rh as a product element and an *electron neutrino*, ν_e:

$$^{103}_{46}Pd + e^- \rightarrow {}^{103}_{45}Rh + \nu_e \tag{1.5}$$

The vacancy created by the electron capture is then filled by electrons from outer orbitals, resulting in the emission of *21 keV γ-rays*. These photons will travel through the medium and can undergo one of the dominant interaction processes for low energy γ radiation: *photoelectric effect* and *Compton scattering*.

1.3.1. Photoelectric effect

The photoelectric effect in Fig. 1.9, is where a γ-ray is completely absorbed by an atom.

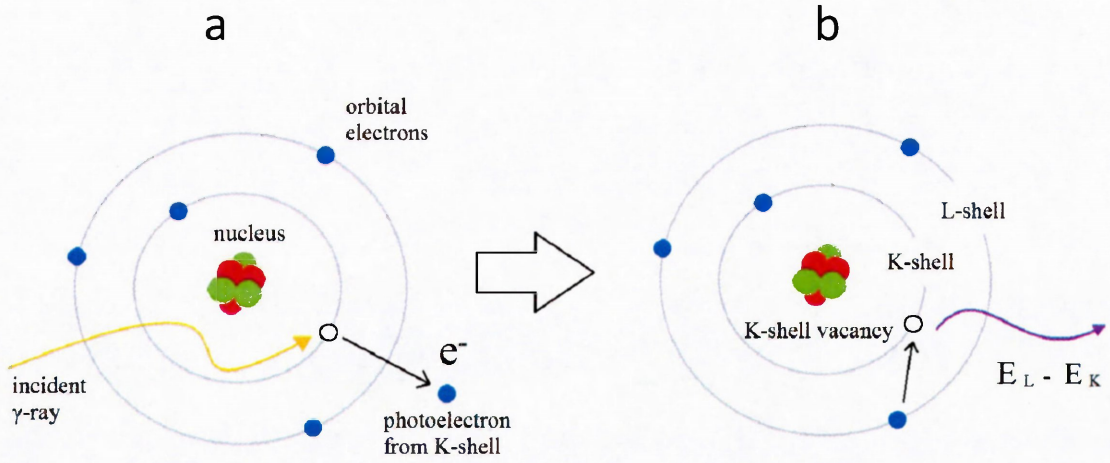

Figure 1.9 The photoelectric effect is a mechanism of full energy deposition in a material. An incident photon transfers all its energy to the ejected photoelectron (a), causing the K-shell hole to be filled by an orbital electron (b). The state change of this electron results in a photon emission with energy equal to the L and K-shell energy difference, denoted by E_L and E_K, respectively.

The energy of the incident γ-ray is transferred to one of the orbital electrons, which causes it to eject as a photoelectron with energy given by:

$$E_{photoelectron} = E_\gamma - E_b \tag{1.6}$$

where $E_{photoelectron}$ is the kinetic energy of the photoelectron, E_γ is the energy of the incident γ-ray, and E_b is the binding energy of the orbital electron [9]. The vacancy left in the atom by the photoelectron is immediately filled by an electron from the outer shells, causing a photon to be

emitted with energy equal to the difference in binding energies of the initial and final shells of the electron. Following ejection, the photoelectron can interact with other electrons in the absorbing medium and will become absorbed within a short distance. Thus, all of the incident γ-ray energy will have been deposited in the material.

The photoelectric effect involves mainly those electrons that are closely bound to the nucleus (inner orbitals) in the K and L-shells. The probability for the effect becomes less for the electrons that are more loosely bound in outer orbitals. The probability of a photon undergoing photoelectric absorption per unit distance, σ_p, depends on photon energy, E_γ, and the atomic number, Z, of the absorbing medium [9]:

$$\sigma_p \propto \frac{Z^3}{E_\gamma{}^3} \tag{1.7}$$

If the energy of the incident photon is less than the ionization potential or binding energy of an electron in a particular inner shell (i.e. if $E_\gamma < E_b$), that electron can not be involved in the photoelectric effect. Those γ-rays with lower energy are more likely to interact by photoelectric absorption, especially in materials with higher Z's. Since soft tissue is generally composed of low Z elements, the probablity of photoelectric absorption is reduced. Instead, a scattering process is much more likely.

1.3.2. Compton scattering

The other way a γ-ray interacts with an absorbing medium is by Compton scattering, as in Fig. 1.10. This is the dominant mechanism in body tissue, where the γ-ray will transfer only part of its energy to an electron. The remaining energy is taken away by a new γ-ray of lower energy, $E_{scatter}$.

This process differs from the photoelectric effect in that: a) the photon transfers only a fraction of its energy to the electron; and b) only the loosely bound electrons in the outer orbitals are involved in the process.

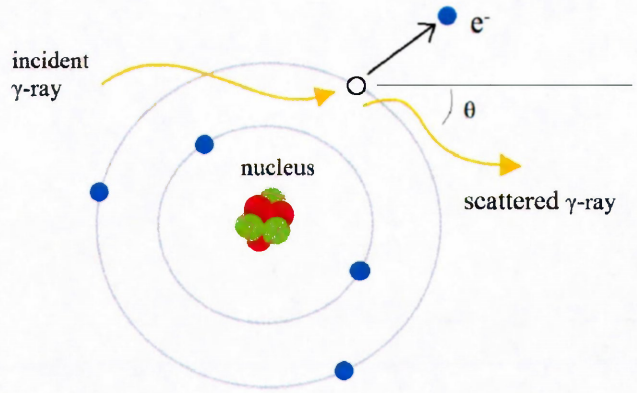

Figure 1.10 Compton scattering is an incomplete energy deposition process in a material. An incident photon transfers part of its energy to a loosely bound electron while the remainder of its energy is scattered at some angle, θ.

The energy transferred to the scattered photon is related to the scattering angle θ by:

$$E_{scatter} = \frac{m_e c^2}{\frac{m_e c^2}{E_\gamma} + 1 - cos\theta} \tag{1.8}$$

where E_γ and $E_{scatter}$ are energies of the incident and scattered photon, respectively, and $m_e c^2$ is the rest-mass energy of an electron [9]. The remainder of the energy is transferred to the recoil electron. The probability of Compton scattering per unit distance, σ_C, decreases gradually with increasing E_γ, and is proportional to density but quite independent of Z.

γ-ray scattering falls into one of two processes; elastic and inelastic. Compton is an inelastic scattering process since the initial kinetic energy of the γ-ray is different than that after interaction with the medium. By conservation of momentum, the γ-ray must change its direction if its energy is not completely absorbed, as in photoelectric effect. Elastic scattering differs in that the kinetic energy of an incident γ-ray is conserved after scattering, along with its momentum. Rayleigh scattering is an example of an elastic process [9].

1.3.3. Attenuation

A γ-ray travelling through a medium are most likely to interact by one of the two processes described and will become completely attenuated. The number of unattenuated photons after a distance of x in an absorbing medium is given by:

$$N = N_0 e^{-\mu x} \tag{1.9}$$

where N is the number of unattenuated photons after travelling a distance x, N_0 is the initial number of photons and μ, the linear attenuation coefficient, is the probability of interaction per unit distance travelled [9]. With the dominant interactions being photoelectric and Compton, μ can be approximated as the sum of the two probabilities [9]:

$$\mu \approx \sigma_p + \sigma_C \tag{1.10}$$

Now that the dominant γ-ray interaction processes have been shown, and by recalling the inverse square law, the number of particles at the detector surface are further reduced. An appropriate imager for PBSI must therefore have good detection efficiency for γ-rays since attenuation will ultimately limit the dose at the detector. Also, due to Compton scattering, the imager requires energy discrimination capability so that positional information lost to scattering within the body can be rejected based on their reduced energy. This principle is called energy-selective counting, which is the very basis *single-photon emission computed tomography* (*SPECT*), a process of image reconstruction in radionuclide imaging.

1.4. Imaging for PBSI

Imaging modalities that have the potential to provide the necessary information required to perform a real-time intervention in PBSI are: a) *3D ultrasound*; b) *C-arm computed tomography (CT)*; and c) *gamma camera imaging* [4].

Although 3D ultrasound is able to generate 3D images in real time, this imaging modality has two main limitations. The first is that the contrast between the seeds and the background anatomy is poor, due to the presence of the seroma and fibrotic tissue, plus air bubbles that are introduced by the brachytherapy needles, making the seeds difficult to identify from the noisy images. The second reason is that to acquire an image of the underlying seed distribution the transducer must be pressed against the breast, thereby deforming the seed distribution and reducing the reproducibility of the image [10].

C-arm CT provides high resolution and good contrast images of the seed distribution. Unfortunately, due to geometric constraints, the template and the fiducial needle that holds the target volume in place has to be removed in order to acquire the images. Once the fiducial needle is removed from the patient, it is extremely difficult for an oncologist to make an accurate intervention even with the high quality images created from the C-arm CT [4]. Since each seed in PBSI is essentially a radiation emitter in itself, it seems only fitting that imaging the γ-rays would be more effective than sending external radiation through the breast as in the ultrasound and CT approach.

Radionuclide imaging is one of the most important applications of radioactivity in nuclear medicine. These imaging laboratories are located in almost every hospital, with hundreds to thousands of imaging procedures each month at larger institutions. The principle of imaging a radionuclide is to acquire a picture of the distribution of a radioactive substance or material within the body. This is done by recording the energetic emissions from the radionuclide with external radiation detectors placed at locations outside of the patient. The preferred emissions for this application are x-rays and γ-rays of energy range *60* to *511 keV*. These energies are sufficiently penetrating in bodily tissues to be detected from deeper organs. Also, they can be stopped efficiently by dense scintillators or other high Z detector materials and can be shielded with reasonable thicknesses of lead.

As the name implies, a *gamma camera* can accomplish this task by imaging the γ-ray emission of each seed. Once specially tuned, this camera will provide the best approach to PBSI imaging, since in contrast to CT, it will not interfere with the equipment required for the implantation. Due to the small size, this device will also be practical for use in a variety of clinical settings.

Furthermore, emission images from the seeds acquired by dedicated gamma camera can be co-registered with anatomic images provided by other imaging modalities. The overall goals of this gamma camera are to enable effective treatment of breast cancer by ensuring the accurate placement of seeds during surgery and evaluating the seed dose distribution during and at the end of the implantation by guiding the seed implantation and allowing for correction of a less than optimal implant while the patient is still in the operating room and anesthetized.

1.4.1. Energy-selective counting

Radiation detectors produce electrical pulses whose amplitudes are proportional to the energies deposited in the detector by individual γ-ray interactions. This experimental technique is called *pulse-height spectroscopy* (*PHS*) which is used to sort out multiple radiation energies striking a radiation detector and then display the results as a histogram. This method is used in all *pulse-height analyzer* (*PHA*) hardware implemented into a gamma camera system. The underlying principle is to examine the amplitude of electrical signals from radiation pulses to determine the radiation energies, or to select for counting only those energies in the desired range (energy-selection). This technique will be detailed further in chapter 3, where PHS experiments are performed. For energy-selection to work in a detector the total collected signal must be large enough such that the detector can perform as a photon counting device, distinguishing single photon emissions from a radiation source and assigning a count to it. In short, energy-selective counting in SPECT can be used to: a) reduce the effects of background radiation; b) reduce the effects of scattering; c) separate events caused by different radionuclides in a mixed radionuclide sample; and d) identify emission energies from unknown radionuclides.

PHA discrimination circuits are incorporated in scintillation cameras and other nuclear medicine imaging devices [11] to reduce effects of scattering by rejecting scattered photons of lower energies (Compton effect). As Fig. 1.11 illustrates, scatter rejection is very important because counting these photons would cause misalignment with their actual positions, resulting in poor spatial resolution. In the energy data, this crops up as a small peak next to the photoelectric absorption energy peak (or "*photopeak*"). By setting an energy window in the PHA, only those energies deposited in the detector will be registered to the image processor and those outside the

energy window are cut out. Therefore, by eliminating these lower energy events from the rest of the histogram, only the photopeak energies will register to the image processor. These correspond to photons which have not been scattered, and so image reconstruction can be accomplished for their linear or nearly linear trajectories. It's important to understand that position signals in PHS are normalized to the total signals, so that the calculated position of interaction is independent of the pulse-height [9].

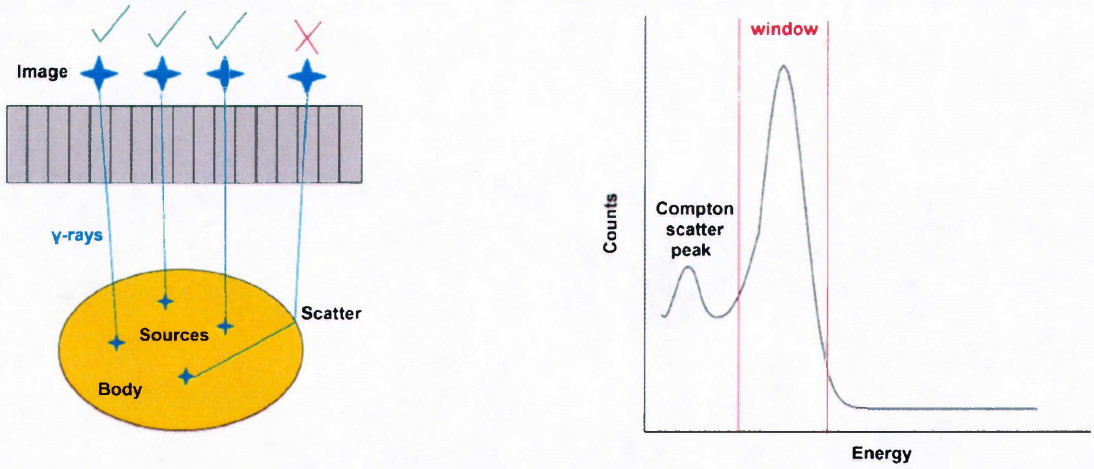

Figure 1.11 The left image shows how some radionuclide emissions from the body will scatter and register an image far out of alignment from the initial source. The green checks indicate images in alignment with their origins while the red X's show misalignments due to scattering. By defining an energy window in the pulse-height data, shown on the right, scattering can be subtracted from the photopeak and photons with those energies will not be passed onto the image processor.

1.4.2. The gamma camera

The SPECT technique uses a gamma camera to record 2D planar images at a series of angles around the patient. These images are then subjected to a form of digital image processing, called image reconstruction, in order to compute images of 2D slices through the patient [7]. Typically, a SPECT device is arranged as several gamma cameras in a ring around the patient to reconstruct γ-ray emission in all directions. For PBSI however, the seeds do not require to be imaged, only their 3D distribution is required. This can be accomplished with a set of just two detector heads, arranged orthogonally, as in Fig. 1.12. Each detector is constructed with similar components: a) the collimator, featuring several parallel-holes which selectively direct γ-rays to the radiation

detector; b) a photoconductor material using highly sensitive semiconductors like *amorphous selenium* (*a-Se*) or *cadmium zinc telluride* (*CdZnTe*); and c) the pixelated electrodes with readout electronics to acquire electrical signal from the radiation detector and process that signal into an image.

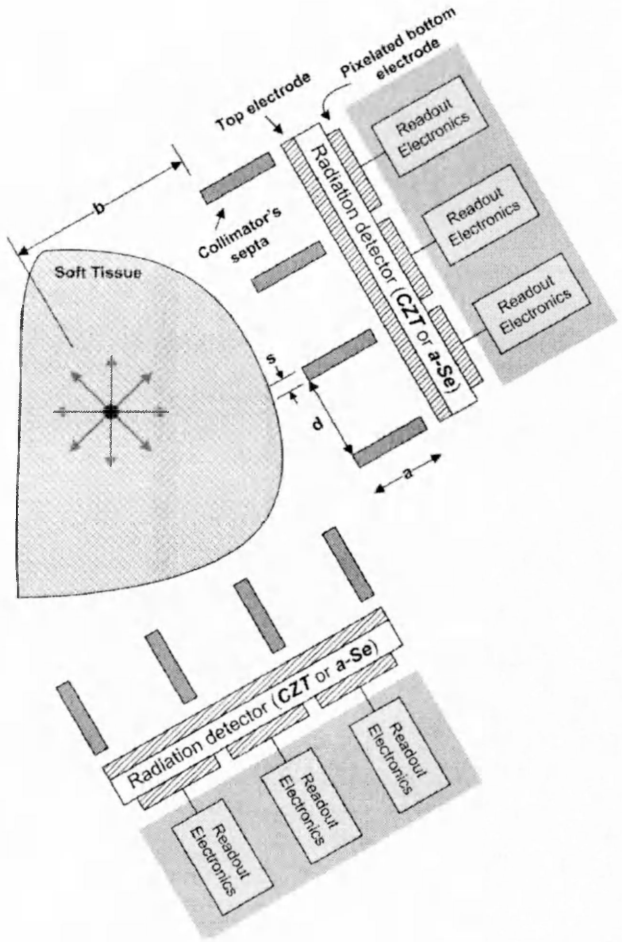

Figure 1.12 The required gamma camera design for PBSI, based on CdZnTe or a-Se photoconductors [12].

In reference to Figs. 1.12 and 1.13, there is a very important component between the gamma camera head and the γ-rays. This is the collimator, which is used to selectively direct the γ-rays onto the camera head. In general, collimation is a way to filter unwanted radiation from particular directions. The most common are optical collimators, which only allow light to pass through a small opening, usually placed in front of a lens. This is a selective way to block certain photons,

yet allow others to pass. Since we are using a similar principle of "absorptive collimation" in this gamma camera system, the collimator is essentially the weak link in the design and must carefully be optimized for the PBSI sensitivity and resolution requirements. This will be detailed in the next chapter, where the collimator is specifically tuned for the PBSI requirements.

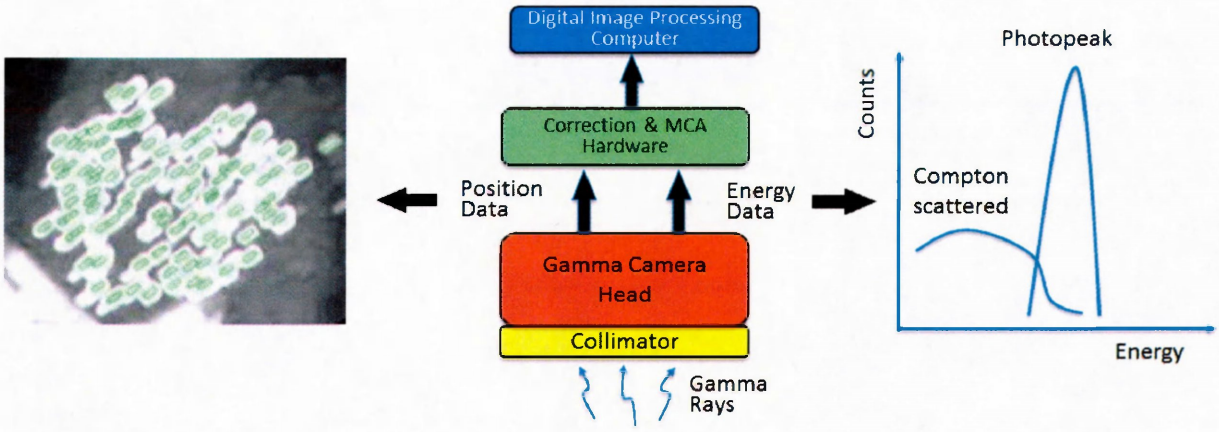

Figure 1.13 A gamma camera consists of a collimator, detector (or gamma camera head), PHA hardware and digital image processor. The two pieces of information that the electronics receive are: position data and related energy data. With scattering processes, the energy data is skewed to the lower end of energy spectra.

As in Fig 1.13, two important pieces of information from the radionuclide are collected by the gamma camera head: *position data* and *energy data* [7]. Both are sent to the correction hardware where digital image processing is done on position data and energy-selective counting on the energy data. In the spatial data, Compton scattering events are misleading, giving incorrect position information to the image processor (see Fig. 1.11) which essentially creates image blur. By rejecting these, both energy and spatial resolution of the gamma camera can be improved. To meet the PBSI technique requirements, the gamma camera must possess: a) high system spatial resolution (< 5 mm at 10 cm from the collimator face) so that significantly misplaced seeds can be identified and promptly corrected [4]; and b) high sensitivity at low γ-ray energies (20-23 keV) to provide a short acquisition time (a few minutes) in order to facilitate correction of seed placement while patient is anesthetized [4].

The standard gamma cameras available are made from *sodium iodide* (NaI) scintillation detectors, which provide both of these features at a reasonable cost [8]. That is why these types of gamma cameras are the choice for radionuclide imaging with energies of 60-300 keV [9].

However, NaI based gamma cameras cannot perform as well if we are interested in imaging lower energy emissions < 60 keV. Due to the hygroscopic nature of the NaI crystal structure it must be enclosed in a thin aluminum casing to prevent exposure to air from which the crystal will readily absorb moisture. Typically, the casing absorbs almost all low energy γ-rays which leaves very little to be detected. Of course, after waiting a long period of time, NaI can acquire an image but at such low energy, this takes about two hours, well beyond the time constraints of the one-hour PBSI procedure [4]. Because of this, we need an alternative detector to image radionuclides in the low energy γ range < 60 keV. Furthermore, the components in these types of detectors are bulky and not very suitable for portable gamma cameras. Use of a semiconductor detector can overcome these issues as the advancements in photoconductors for digital radiography have proven to be sensitive enough to distinguish single photon emissions (or photon counting).

1.4.3. Photoconductors for gamma cameras

A sufficiently large collection of signal can only be accomplished by detectors that can stop incident γ-rays such that those energies can be successfully deposited into the detector to undergo transduction. Transduction is the transformation of one type of energy to another, for instance, electromagnetic radiation into electrical charge, a simple direct-conversion process. In this process, an incident photon will ionize electrons in the photoconductor, resulting in many electron-hole pairs (EHPs) which drift to opposite electrodes with an applied electric field, $\vec{E}$. The EHPs can then be immediately collected as an electrical signal by the detector electronics. Indirect-conversion detectors use a scintillation crystal to convert γ-rays into optical photons. Direct and indirect processes are illustrated in Fig. 1.14. The optical photons are then converted into electrons via photomultiplier tubes (PMTs). PMTs are efficient at converting photons into electrical signal but they require high-voltage, are expensive and bulky. In addition, scattering of the optical photons in the scintillator results in degradation of spatial resolution, signal loss and lowers the overall signal-to-noise ratio (SNR) of the detector. In contrast, in direct-conversion detectors, generated EHPs follow the electric field lines (see left image of Fig. 1.14) prior to being read out. Since there is no intermediary optical stage to contribute to blurring, these systems have the important advantage of providing superior spatial and energy resolution

compared to indirect-conversion detectors. However, the photoconductor needs to be thick enough to yield a reasonable attenuation at required energies.

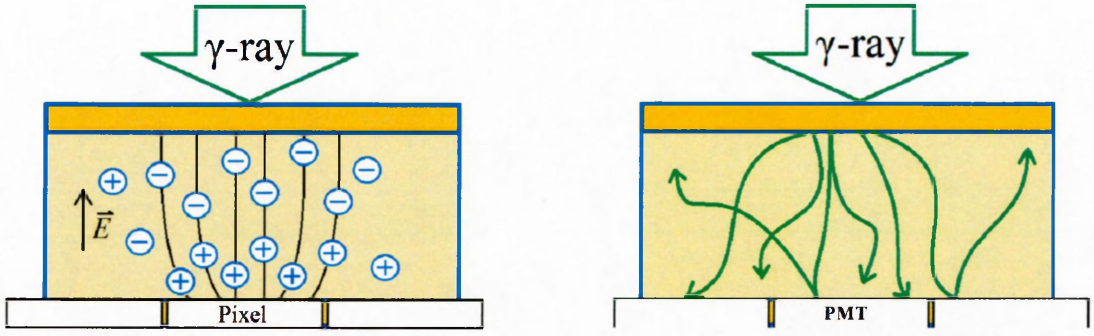

Figure 1.14 The mechanisms of γ-ray transduction in a direct-conversion semiconductor material (left), compared to an indirect-conversion scintillation crystal (right). The first converts a photon to several EHPs via photoelectric absorption while the latter converts to optical photons in the crystal, then to electrons in the PMTs. Scattering of the optical photons within the crystal results in degradation of spatial resolution, signal loss and thus, lowers SNR.

Commonly used semiconductors in nuclear medicine include: *silicon* (*Si*), *germanium* (*Ge*), *cadmium telluride* (*CdTe*), *cadmium zinc telluride* (*CdZnTe*) and *amorphous selenium* (*a-Se*), with their properties listed Table 1.2. The $W_{\pm}$ is the photoionization energy of a photoconductor, which measures the typical ionization energy required to generate a single EHP. The $W_{\pm}$ is highly electric field dependent and takes the values in Table 1.2 when biased at an infinitely large field.

Table 1.2 Common direct-conversion detectors (parentheses indicate dopants) used in nuclear medicine and their associated density (1), atomic number (2) and photoionization energy (3). Air is shown for comparison [9].

	Si(Li)	Ge(Li) or Ge	CdTe or CdZnTe	a-Se	Air
1 ρ (g/cm^3)	2.33	5.32	6.06	4.79	0.001297
2 Z	14	32	48 52, 48 30 52	34	~7.6
3 $W_{\pm}$ (eV)	3.6	2.9	4.43	5.9	33.7

Of all semiconductors listed above, their theoretical $W_{\pm}$ are similar, where one ionization is produced per 3 to 6 eV of radiation energy absorbed. Comparing to air, about 34 eV is required for ionization. Thus a semiconductor detector is not only a better absorber of radiation, but also produces about 10x larger electrical signal. The signal is large enough to permit detection and counting of individual radiation events. Furthermore, the size of the electrical signal is proportional to the amount of radiation energy absorbed. Therefore, direct-conversion materials can be readily used for energy-selection and photon counting techniques.

Unlike NaI, these semiconductors do not require an aluminum seal as they are non-hygroscopic. In addition, they can be fabricated onto thin electronic hardware and are compatible with highly sensitive charge-coupled devices (CCD) and complementary metal-oxide-semiconductor (CMOS) sensors commonly used in photon counting digital cameras [12]. Unfortunately, use of Si or Ge for γ-ray detection is complicated by their high dark currents at room temperature operation. Dark current introduces electronic noise and thus lowers the overall SNR of a photoconductor detector. As a result, Si and Ge detectors must be operated at low temperatures using liquid nitrogen which is technically unfeasible.

In contrast, CdZnTe has all the desirable properties: high stopping power, low thermal noise, room temperature operation, excellent energy resolution and excellent spatial resolution [13]. With these features, CdZnTe is increasingly being considered as an alternative to NaI/PMT systems in a variety of applications in nuclear medicine, including intra-operative portable imaging devices [14,15]. In comparison, CdTe has a much greater hole collection efficiency than CdZnTe, however, space charge effect limits its performance. This occurs due to the accumulation of trap carriers which generates a localized internal electric field. This essentially reduces the bias field [16,17] and destroys the homogeneity of the electric field inside the photoconductor. This effect is circumvented by introducing Zn into the structure. CdZnTe is currently the only single crystalline semiconductor used in direct-conversion gamma cameras since CdZnTe can operate at room temperature, unlike Si and Ge. Other advantages of CdZnTe detectors include high sensitivity for x-rays and γ-rays, due to the high atomic numbers of Cd and Te, and better energy resolution than scintillator detectors. CdZnTe can be formed into different shapes for different radiation-detecting applications, and a variety of electrode geometries, such as coplanar grids, have been developed to provide unipolar (electron-only) operation, thereby

further improving energy resolution. At this time, however, there is no CdZnTe device capable of imaging at ~20 keV due to the lack of a high performance read-out system. Current electronic systems developed for CdZnTe have a noise threshold of about 30 keV, which is greater than the 21 keV in PBSI [18]. Thus, there is a need to develop a read-out method such as Application Specific Integration Circuit (ASIC) with CdZnTe dedicated to fast imaging at low gamma photon energies before the advantage of PBSI image guidance can be achieved [18]. As an alternative to CdZnTe, other direct-conversion materials used in xerography (x-ray application) can be well suited to image low energy radionuclides.

Both a-Si and a-Se direct-conversion technology has been developed successfully to create large area, flat-panel x-ray imagers (FPXIs) for digital chest radiography and mammography [19-26]. Currently, these types of detectors for diagnostic medical imaging use a-Si:H 2D arrays of passive pixel sensor structures for x-ray image acquisition [27,28]. The a-Se photoconductive layer is deposited directly onto this structure and serves as the x-ray-to-charge trasucer. Currently a-Se is the only photoconductor whose technology is mature enough for application to x-ray imaging. The main drawbacks of a-Se are its relatively low x-ray-to-charge conversion efficiency and low x-ray attenuation coefficient, which limits its clinical applications [29]. However, a-Se properties fit the low energy range required for PBSI imaging.

Direct-conversion digital radiography systems described above use photon integration technique. An alternative approach that can achieve higher sensitivity is by photon counting, where the intensity of each image pixel is equal to the number of photons that interact with the detector. In the photon counting method, the photon-generated charge in the pixel is compared to a predetermined threshold value where the threshold value is chosen to be, at the very least, greater than the background noise. If the x-ray photon signal exceeds this threshold, the value of a counter is incremented. Any photon detected with energy above the threshold value is assigned a weight of one (i.e. single photon counter). The main advantages of photon counting over photon integrating pixels are:

a) Better weighting of information leading to selectivity between photons of different energies that is a major requirement of energy-selective imaging. Higher energy photons deposit more charge in the detector than low energy ones so that in an energy integrating detector, the higher energy photons are weighted higher. In a photon counter, events are defined by predetermined

threshold values. Implementing a single threshold will weight all information equally. Implementing multiple thresholds enables a means to distinguish between energy levels and thus perform energy-selection.

b) Due to predetermined thresholds, photon counting systems are inherently linear with very large dynamic ranges where at the low count rate, there is no limit and at high count rate by the separation of pulses and capacity of counters.

c) The effect of amplifier noise is independent of frame readout rate as the readout is in the digital domain after the photon has been detected [30]. This noise suppression compared to integrating detectors gives superior SNRs, which are essential for low energy gamma photon counting.

Although photon counting technology has been applied using gas microstrip and silicon microstrip detectors [31,32], solid state x-ray detectors integrated with semiconductor pixel arrays for photon counting have also been under investigation [33,34,35]. The advantage provided by the semiconductor pixel arrays is that they are fabricated in crystalline silicon (c-Si) CMOS technology that has a well-entrenched fabrication infrastructure so that pulse shaping and counting circuitry can be integrated directly at the pixel level which improves SNR [36,37]. This is benficial over counting systems where the detector and readout apparatus is discrete. A high degree of integration and small device sizes, as provided by c-Si technology, is essential for photon counting imagers due to the pixel resolution and count rates needed to capture the typical fluence rates of photons in radiation imaging applications [38,39,40,41]. Thus, a portable γ-ray photon counting camera dedicated to imaging of low energy isotopes like ^{103}Pd is ideal for seed implantation guidance, since it potentially can offer both, high spatial resolution and sensitivity. In turn, this will satisfy both criteria for the PBSI imager. With this in mind, we examine the potential of a-Se with photon counting readout for brachytherapy applications. With very good sensitivity and spatial resolution at mammography energies, a-Se technology can be a very practical and cost-effective implementation in a portable 2D gamma camera for image-guided breast brachytherapy. This thesis aims to initiate the development of a PBSI imager based on a-Se through proof-of-principle, by computer simulation and pulse-height spectroscopy experiments.

1.5. Thesis outline

The research objective of this thesis is to implement a gamma camera for PBSI, based on a-Se photoconductor. Since its current application in FPXIs are sensitive to x-ray mammography energies, very similar to those in PBSI, it will provide a cost-effective and technological advantage over CdZnTe. The proposed PBSI gamma camera design, shown in Fig. 1.12, should consist of two SPECTheads for image reconstruction, an appropriately tuned collimator, a photoconductor layer (CdZnTe or a-Se), "sandwiched" between a top and bottom electrode, and the required photon counting readout electronics associated with it. The structure of the a-Se detector can be implemented from the same FPXI designs as mammography detectors with pixels of 200 x 200 μm, which is suitable for PBSI since each seed will only be localized, not imaged in detail. With specified dimensions of 10 x 10 cm, there will be a 500 x 500 pixel architecture for this pixel size. For this particular application this pixel size is much smaller than required, although, the use of smaller pixels result in lower noise levels in the pixel amplifiers [30] which is desirable. With this design in place, our research goals are to: a) develop a test platform for the evaluation of the gamma camera and to assess its imaging performance; and b) show that a-Se is sensitive enough for photon counting at low energy. Using CdZnTe as a baseline, we will demonstrate proof-of-principle of this gamma camera by computer simulation and perform PHS experiments to directly measure the $W_{\pm}$.

An a-Se detector should be able to resolve ^{103}Pd photopeak energy to quickly localize each seed for a 60-80 seed distribution in a breast phantom, consistent with a typical PBSI procedure. Localization of the seeds in a short duration should be observed in the simulation, which will be the basis of the next chapter of this thesis.

Chapter 2

Monte Carlo simulation for permanent breast seed implantation

2.1. Monte Carlo in particle transport

Monte Carlo (*MC*) is a stochastic method for calculation by building models of possible results from substituting a probability distribution for any factor with uncertainty [42]. For each photon emission, MC samples an interaction probability distribution with random numbers. A random number generator is used to determine the occurrence of stochastic events. For example, using the random number, R, generated uniformly on an interval $\{0,1\}$, it is possible to simulate several random outcomes from cumulatively integrating with R, over some probability distribution [43]. In the case of particle transport, each photon interaction is derived from the cross-section (CS) of the target material, and by the energy of the incident photon. In nuclear physics, the concept of a CS is used to express the likelihood of interaction between particles.

The history of using similar random processes like MC dates all the way back to the late 1700s, where a simple needle tossing experiment was performed to calculate π. The mathematician, Laplace did something similar by taking random points in a rectangle in 1886 and Fermi in 1930 to calculate properties of the newly discovered neutron. During the 1940s, with the development of the Manhattan project, two scientists working on the project coined the term "Monte Carlo" (from the casino in Monaco) while simulating the initial development of thermonuclear weapons. Like most other things, the age of digital computing lead to exponential growth in MC simulation potential and the associated software applications. The first complete coupled electron-photon transport code named ETRAN became available by 1963. Then, from the 1980s, numerous MC simulation packages for medical physics were being implemented for research and clinical applications [44].

MC simulation is an essential component in emission tomography to aid in the design of new medical imaging devices, assess new implementations of image reconstruction algorithms and/or scatter correction techniques, and optimize scanning protocols. Although dedicated MC codes

have been developed for Positron Emission Tomography (PET) and for SPECT, these tools suffer from a variety of drawbacks and limitations in terms of validation, accuracy, and/or support [45]. On the other hand, accurate and versatile simulation libraries such as GEANT3, EGS4, MCNP, and GEANT4 have been written for high energy physics [46]. They all include well-validated physics models, geometry modelling tools, and efficient visualization utilities [47,48,49]. Depending upon the number samples, a MC simulation could involve thousands or tens of thousands of recalculations before the desired statistical uncertainty is achieved. Furthermore, with the very large number of events simulated (~7.4 x 10^7) for each ^{103}Pd source, there is a need for cluster computing in order to complete simulations in a reasonable time frame.

2.1.1. Compute resources

Due to the magnitude of calculations required for MC simulation, high-performance computing is normally required to run complex particle transport simulations in a reasonable time frame. For this we need to select the appropriate resources to use. The Lakehead University High-Performance Computing Centre (LUHPCC) was used to run simulations on their 240 compute core Linux cluster that was installed in the summer of 2011. The cluster is composed of 20 compute nodes housed within five Dell PowerEdge C6100 series chassis (4 nodes/chassis), a PowerEdge R710 login/head node, and a PowerEdge R710 storage node with 12 TB of direct attached storage in a PowerVault MD 1200. A PowerConnect 6248 Gigabit Ethernet switch serves as an interconnection fabric between all of these components making it suitable for serial farming and low-bandwidth MPI cross-node calculations. A PowerEdge C410x PCIe Expansion Chassis also provides general purpose graphics processing unit capabilities.

2.1.2. Introduction to GATE

GATE (*Geant4 Application for Emission Tomography*) is a widely used Monte Carlo Simulation platform, which is being developed by the OpenGATE collaboration since 2001 [50]. Computer simulation is often used in designing modern emission tomography instruments. Before a device

is built, there is a need to test its capability with a validated platform. GATE provides that in a "toolkit" which can simulate interactions of photons and subatomic particles with matter, specific for tomography applications. It features a broad range of physics processes validated by particle physics experiments, sophisticated geometry description, powerful visualization, 3D rendering and other original features desirable for emission tomography [50]. The package also contains tools useful for analyzing results for both energy and spatial representation.

Dedicated to the modeling of planar tomography, SPECT and PET acquisitions, this platform is widely used to assist in the research and development of new imaging devices and techniques. Validation of the platform has been quite successful in recent scintillation camera simulations. Results obtained with GATE are generally within 6% of published results from similar tomography experiments [51,52]. Following the first public release of GATE in 2004 a major enhancement, referred to as GATE V6, was published in 2010 [50]. Besides the introduction of CT and radiotherapy simulations, the recent version allows the selection of various physical models for a specific process, but also the simulation of optical and hadronic processes. It also includes options for speeding up GATE simulations. GATE has proven to be a powerful and worldwide well received tool to design and study medical imaging devices owing to the flexibility to build a device based on usage of *macros*. Macros are script files, which systematically provide details to GATE of how the simulation is to be performed. These macros are the building blocks, specifying materials and parameters for building the detector, defining the sources and activating particle interactions. In the following section, the essential macro commands have been included in textboxes for reference.

2.2. GATE simulation method

GATE is composed of several modules, broken down into components shown in Fig. 2.1, defining the geometry and mechanisms associated with each particle interaction. As an MC tool, GATE also needs a random number generator. The class libraries for high energy physics (CLHEP) provide various ones such as Ranlux64, the James Random and the Mersenne Twister [53]. Each simulation can be broken down into 6 steps: a) define the radiation detector and phantom geometry; b) set up the detector model (ie. SPECT, PET, etc.); c) define the source(s);

d) set up the physics processes; e) specify the data output format; and f) initialize the simulation [53]. Since the detector geometry remains the same in each run, it is included into the main macro called *gamma.mac*, along with the configuration for defining orientation and materials used for each component. The digitizer, physics and output scripts have also been included into this file. Sources have been separated into different macros since the configuration file can call upon which source is to be simulated.

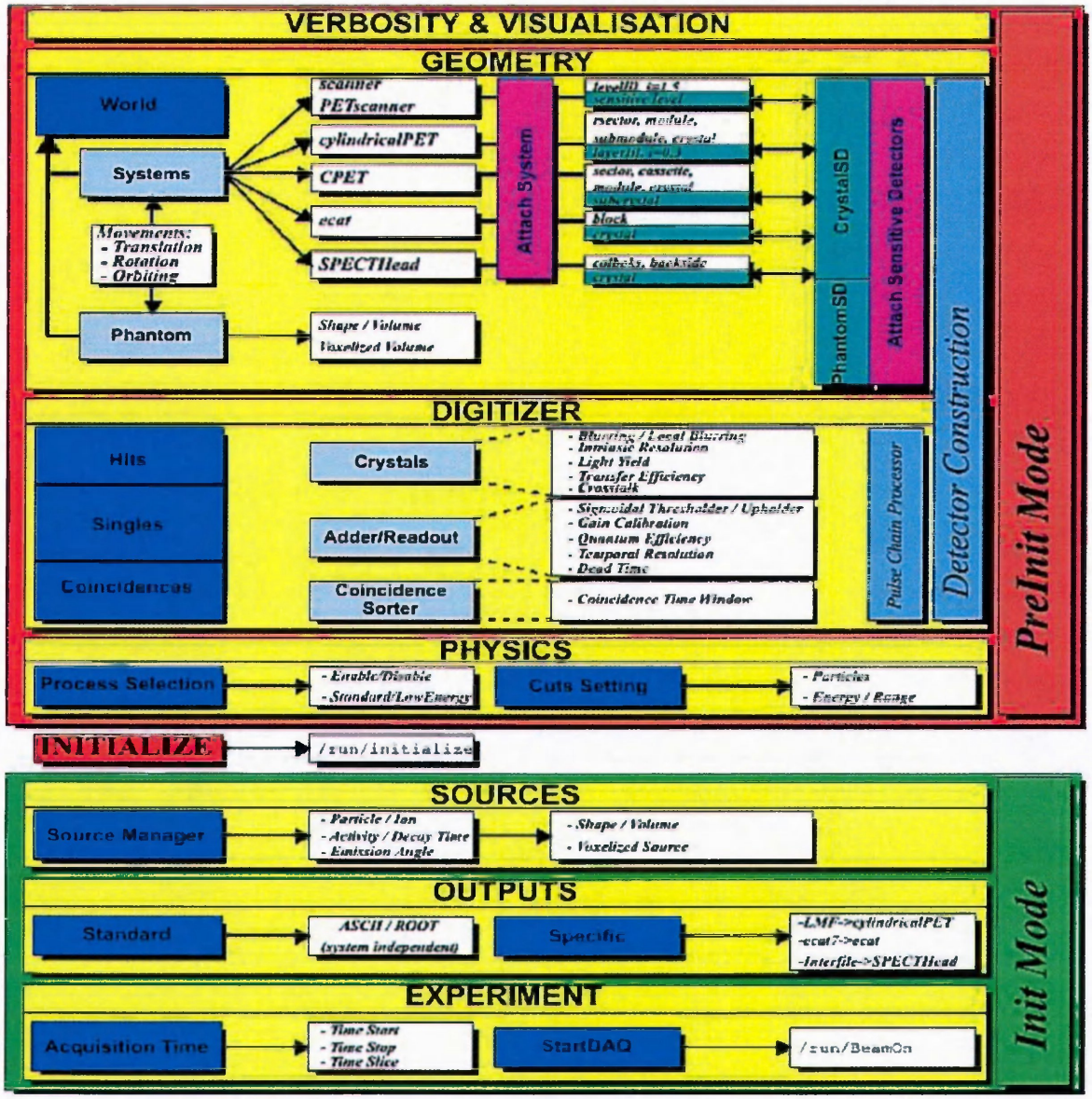

Figure 2.1 A diagram from the GATE user's guide, showing the simulation architecture categorized by modules. Each module is divided further into several components defining the simulation parameters [53].

2.2.1. Geometry setup

The first volume which is created is the world. Each new volume created is contained within the world and thus the dimensions must be large enough to include all of the simulated geometries like the detector and the breast phantom. The macro shown below generates the world with an air medium of dimensions 120x120x120 cm in X-Y-Z coordinates:

```
/gate/world/geometry/setXLength      120 cm
/gate/world/geometry/setYLength      120 cm
/gate/world/geometry/setZLength      120 cm
/gate/world/setMaterial              Air
```

All new volumes contained within the world are termed "daughters" and those daughters may also be "parent" volumes to smaller daughter volumes. This nested chain of geometry building is especially important when discussing readout of *hits*. A hit refers to any interaction event, where an incident photon deposits some energy. A sensitive volume, termed, *crystalSD* or *phantomSD*, must be attached to whatever volume where a photon hit is recorded [53]. For instance, if we wish to separate hits in the detector from hits in the phantom, we assign different sensitive detectors to them. *CrystalSD* is assigned to record hits in the a-Se and *phantomSD* for the breast phantom. The first will output hits recorded only in the photoconductor layer while the latter can output hits in the other components. The main reason for separating the two is that *crystalSD* generates both positional and energy data, while the *phantomSD* provides information on the scattering processes, such as which scattering process occurs and where in the volume. Essentially, a breast phantom and one or two SPECTheads composed of a collimator, radiation detector and readout electronics is simulated. The electronics component can be simulated with the digitizer module, as will be discussed in that section. The SPECThead is a parent volume to the other components, so in the following macro we define a thickness of 7.8 cm to contain the 3.8 cm collimator, the a-Se photoconductor and a lead back-compartment to attenuate any photons which pass through the a-Se layer:

```
/gate/world/daughters/name                  SPECThead
/gate/world/daughters/insert                box
/gate/SPECThead/geometry/setXLength         7.8 cm
/gate/SPECThead/geometry/setYLength         10. cm
/gate/SPECThead/geometry/setZLength         10. cm
/gate/SPECThead/placement/setTranslation    8.9 0. 0. cm
/gate/SPECThead/setMaterial                 Air
/gate/crystal/attachCrystalSD
```

The phantom is simplified to a spherical volume of 5 cm radius with the material set to breast. GATE contains a materials database file called, *materials.db*, specifying the composition and physical properties of each material, which the user can freely edit. The breast composition is already included in the database which lists the breast density (d), number of elements composing the tissue (n) and the relative composition percentage of those elements (f) [53]:

```
 Breast: d=1.020 g/cm3; n = 8
+el: name=Oxygen;      f=0.5270
+el: name=Carbon;      f=0.3320
+el: name=Hydrogen;    f=0.1060
+el: name=Nitrogen;    f=0.0300
+el: name=Sulfur;      f=0.0020
+el: name=Sodium;      f=0.0010
+el: name=Phosphor;    f=0.0010
+el: name=Chlorine;    f=0.0010
```

For optimal sensitivity and resolution, the breast phantom surface is touching the collimator, such that the origin is 5 cm from the collimator face defined by R_{max} in the following macro:

```
/gate/world/daughters/name                  Phantom
/gate/world/daughters/insert                sphere
/gate/Phantom/geometry/setRmax              5.0 cm
/gate/Phantom/geometry/setRmin              0.0 cm
/gate/Phantom/placement/setTranslation      0. 0. 0. cm
/gate/Phantom/setMaterial                   Breast
/gate/Phantom/attachPhantomSD
```

For consistency throughout the next section of this chapter, we define the crystal layer to have identical dimensions to the one we will use in our PHS experiment. Not to be confused with the crystalline structure, the crystal term in GATE refers to the photoconductor layer which records both energy and spatial data in addition to scattering. The a-Se composition has been defined in *materials.db*, with density of 4.28 g/cm^3, as per NIST database [54], with no lattice arrangement (amorphous). To follow the same a-Se structure used in later PHS, a 110 μm thick a-Se layer deposited upon a glass substrate will be the choice for simulation, shown in the crystal macro below:

```
/gate/SPECThead/daughters/name              Crystal
/gate/SPECThead/daughters/insert            box
/gate/crystal/geometry/setXLength           0.011 cm
/gate/crystal/geometry/setYLength           10. cm
/gate/crystal/geometry/setZLength           10. cm
/gate/crystal/placement/setTranslation      -0.095 0. 0. cm
/gate/crystal/setMaterial                   Selenium
```

With all the parameters defined for the geometry, the visualization window in Fig. 2.2 a) shows the constructed SPECTheads and spherical breast phantom. The GATE visualization tool is essential for reviewing the constructed geometries and useful in viewing the simulation in real-time. Figures 2.2 b) to 2.2 d) visualize the simulation from several angles. Trajectories of γ-rays are displayed in green and their absorption and scattering interactions in red.

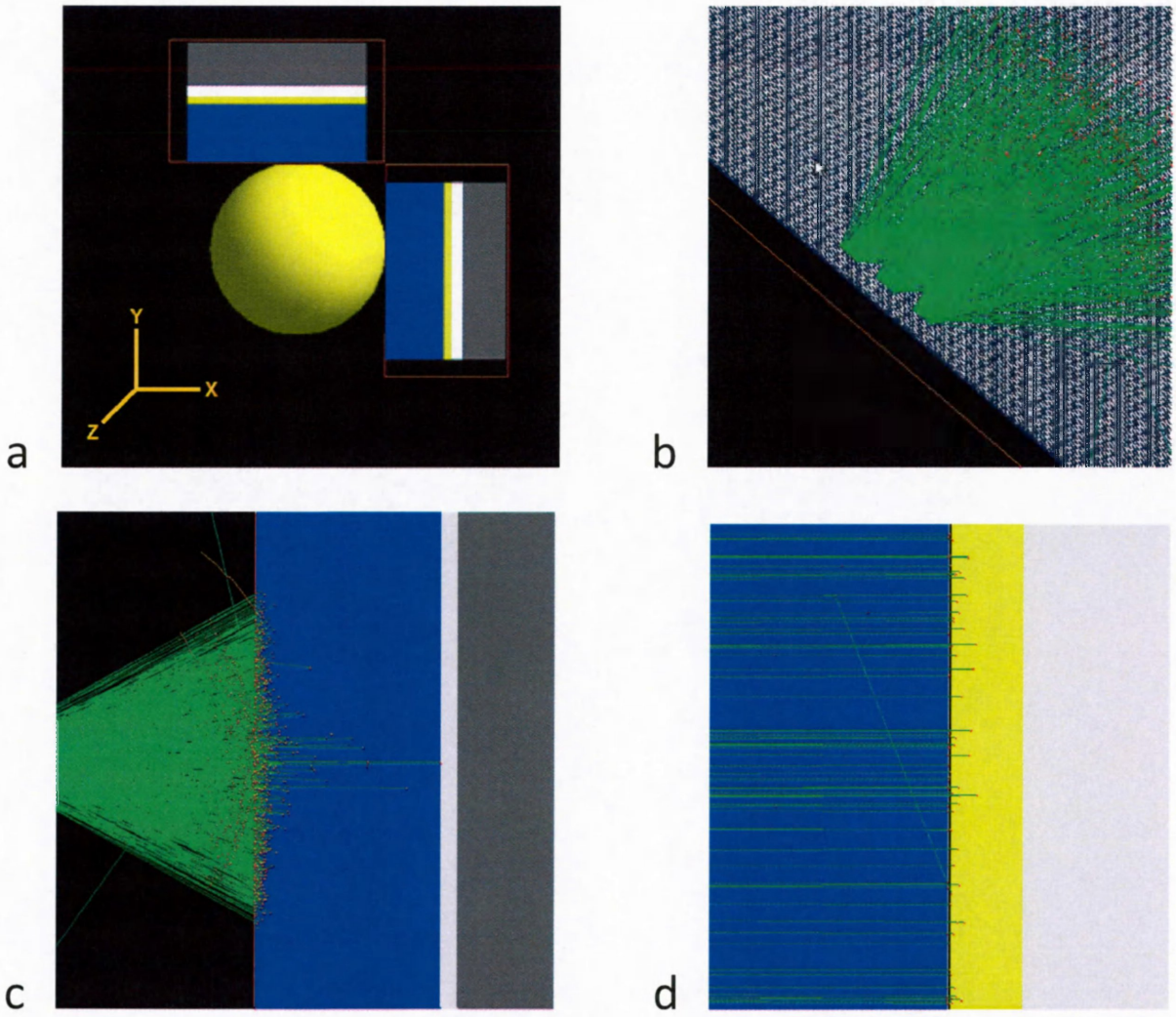

Figure 2.2 GATE visualization windows which show: a) The constructed detector geometry and spherical breast phantom in yellow. Each SPECThead is composed of the collimator (blue), a-Se layer (yellow), glass substrate (white), lead back-compartment (grey) and shielding (red) which encloses all but the collimator face. The a-Se layer has been scaled up to show in this diagram. b) 3 emission sources (21 keV) viewed from 60° oblique to collimator face. c) Same 3 sources viewed from 90° to collimator face. d) Close-up view of 21 keV γ-ray interactions with photoconductor layer and glass substrate.

2.2.2. Collimator optimization

As in most electronic devices, the overall performance of the system is dependent on each individual component. As the collimator is the "bottleneck" of this gamma camera, optimizing its efficiency is critical to meet the PBSI requirements for resolution and sensitivity.

For an isotropic emission, the purpose of the collimator is to block obliquely incident γ-rays from striking the detector. If these were to reach the detector and register an image, the entire image would be "flooded" and appear as a cloud of decreasing brightness away from the center. The required γ-rays to register an image are ones which are almost entirely perpendicular to the detector surface. The collimator efficiency is defined as the fraction of incident γ-rays on the collimator compared to the fraction that passes through to the detector. In this manner, collimator resolution, which is the sharpness of the γ-ray image projected onto the detector, can be improved. Some types of collimators used in nuclear medicine are: parallel hole, slant hole, converging and diverging, fan-beam, and pinhole [9].

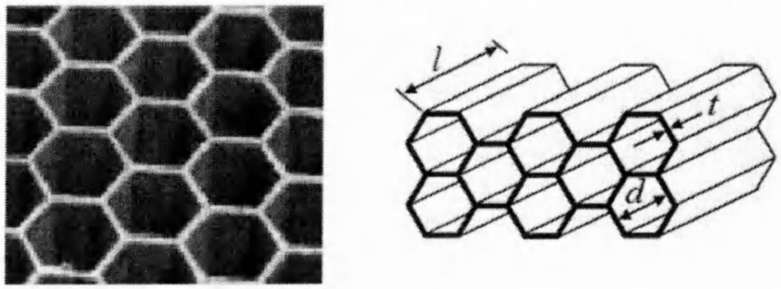

Figure 2.3 A parallel-hole collimator used in nuclear medicine is typically made of lead as an array of hexagonal holes where *d* is the diameter of holes, *l* is their length and *t* is the thickness between adjacent holes [55].

The parallel-hole collimator used in the simulations is illustrated in Fig. 2.3. It consists of a hexagonal septa array made of a high Z material capable of attenuating γ-rays with small thicknesses. All holes are parallel to each other. Common low energy collimator designs are: Low Energy All-Purpose (LEAP) and Low Energy High-Resolution (LEHR) [55].

LEAP collimators have holes with a large diameter. The sensitivity is relatively high as where the resolution is moderate (larger diameter holes allow more scattered photons). The average

sensitivity of a LEAP is approx. 500,000 cpm (counts per minute) for a 1 μCi source, and the resolution is 1.0 cm at 10 cm from the collimator face. LEHR collimators have higher resolution images than the LEAP. They have more holes that are both smaller and deeper. The sensitivity is approx. 185,000 cpm for 1 μCi source, and the resolution is higher with 0.65 cm at 10 cm from the collimator face. To achieve the desired resolution of < 5mm, PBSI requires a LEHR parallel-hole collimator [6]. *Lead*, which has a high linear attenuation coefficient μ = 797.68 cm^{-1} (NIST database) [54], is very likely the most attenuating collimator material, but if manufacturing constraints for the required dimensions arise, other metals with large attenuation coefficients such as *copper* or *tungsten* may also be used.

Relevant collimator parameters were calculated following Ch. 14, section C of *Physics in Nuclear Medicine* by S.R. Cherry, J.A. Sorenson and M.E. Phelps. Equations 2.1 to 2.5 account for the sensitivity and resolution of the collimator from the trajectories of the γ-rays from a point source and by geometric analysis (Fig. 2.4). The first parameter considered is the thickness of material between collimator holes, called septa. The required septal thickness, for less than 5% penetration between adjacent holes is:

$$t \approx \frac{2dw}{l - w} \tag{2.1}$$

where d is the diameter of holes, l is their length and w is the shortest path length for γ rays to travel from one hole to the adjacent one [9], as labeled in Fig. 2.4. Collimator resolution, R_{coll}, is determined from the *full-width at half-maximum* (*FWHM*) of the radiation profile from a point source projected from the collimator onto the detector:

$$R_{coll} \approx d(l_{eff} + b)/l_{eff} \tag{2.2}$$

$$l_{eff} = 1 - 2/\mu \tag{2.3}$$

where b is distance from the radiation source to the collimator surface, l_{eff} is and the effective length of collimator holes and μ is the linear attenuation coefficient of the collimator material [9]. If we know the intrinsic resolution of the detector material, R_{int}, then the resolution for the system can be attained by:

$$R_{sys} = \sqrt{{R_{int}}^2 + {R_{coll}}^2} \tag{2.4}$$

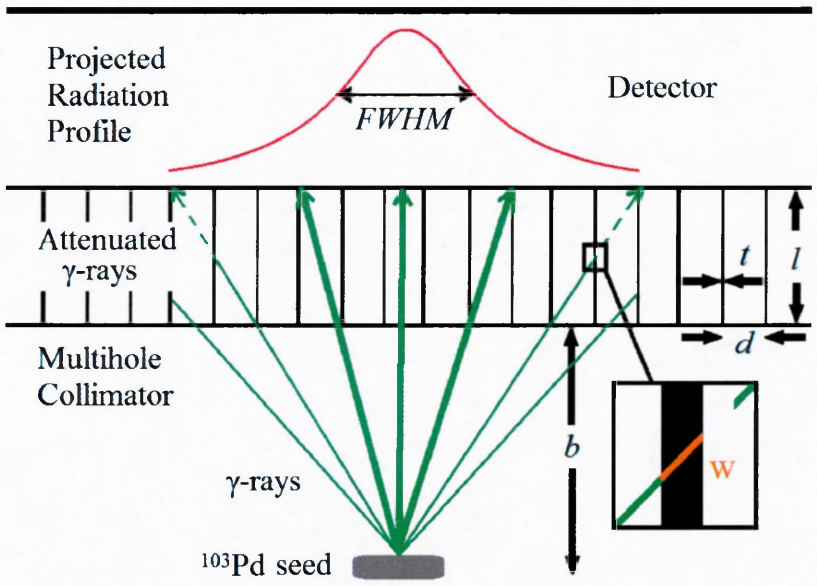

Figure 2.4 The 2D projected radiation profile of a ^{103}Pd seed is a Gaussian with peak intensity defined by γ-rays perpendicular to the point source at distance *b*. The collimator resolution is defined as the FWHM of the 2D radiation profile. For reference, the collimator parameters: *t*, *d*, *l* and *w* are shown as well.

Collimator sensitivity, which is the fraction of γ-rays passing through the collimator per γ-ray emitted by the source toward the collimator is calculated by:

$$g \approx K^2 \left(\frac{d}{l_{eff}}\right)^2 \left[\frac{d^2}{(d+t)^2}\right] \tag{2.5}$$

where K is a constant which depends on hole shape. For hexagonal holes, $K \approx 0.26$ [9]. It is evident that the gain in sensitivity results in a poorer resolution, and visa-versa when manipulating the collimator hole length and diameter.

The following calculations are based on the assumption that the deepest seed will be placed 8 cm into the breast tissue which will be used in our calculation as *b*, the longest distance from the imaging source to the gamma camera. By carefully examining the sensitivity and resolution

equations, a list of parameters for d and l were generated along with a septal thickness (t) which attenuate > 95% of oblique photons, ideally.

The company, *Nuclear Fields*, in the Netherlands is well known for superior quality Micro-cast® collimators, which are still considered the gold standard in Nuclear Medicine [55]. Their website contains a useful tool for calculating collimator parameters by inputting energy along with the previous parameters to see what efficiency and resolution can be achieved. The production limitations listed indicate the minimum hole diameter and septal thickness are 1.2 mm and 0.15 mm respectively. The acceptable resolution must be less than 5 mm for PBSI requirements. As both the resolution and sensitivity depend on d and l, the ranges to satisfy the requirements are listed in Table 2.1.

Table 2.1 Parameter ranges for the design of this collimator.

Hole diameter (d)	1.2 – 2.5 mm
Septal thickness (t)	0.15 – 0.5 mm
Hole length (l)	30 – 40 mm
Average resolution	3.6 mm

To maintain high count rate to minimize imaging time, the optimal collimator parameters are as follows:

$$d = 1.2 \text{ mm} \qquad l = 38 \text{ mm} \qquad t = 0.2 \text{ mm}$$

Then, at the source distance of b = 8 cm, R_{coll} is expected to be 3.73 mm with a sensitivity of 1.83 counts/sec/μC. The activity of a typical ^{103}Pd seed is about *2 mCi*. By factoring this activity, the overall sensitivity will be 3665 counts per second (cps) but we also have to take into account attenuation of γ-rays in the breast. The linear attenuation coefficient, μ:

$$\mu = \lambda_m * \rho \tag{2.6}$$

where λ_m is the mass attenuation coefficient [cm^2/g] and ρ = 1.02 g/cm^3 is the average breast density. For 21 keV energies and assuming a breast composition as in ICRU 44, we consider two

major attenuation processes: photoelectric attenuation, with $\lambda_{photoelectric} = 0.5$ cm^2/g and Compton scattering, where $\lambda_{scattering} = 0.18$ cm^2/g [56].

The number of γ-rays (N_{out}) that will successfully escape the breast can be calculated from the modified exponential attenuation law:

$$N_{out} = N_{in}[e^{-((\lambda_{photoelectric})*\rho)x} + e^{-((\lambda_{scattering})*\rho)x}] \tag{2.7}$$

where x is distance traveled in the breast. For an 8 cm travel distance, the attenuation coefficient will be:

$$e^{-\left(\left(0.5\frac{cm^2}{g}\right)*1.02\frac{g}{cm^3}\right)*8\text{ cm}} + e^{-\left(\left(0.18\frac{cm^2}{g}\right)*1.02\frac{g}{cm^3}\right)*8\text{ cm}} = 0.2471 \tag{2.8}$$

Sensitivity including attenuation coefficient will be: 3665 cps * 0.2471 = 905 cps. Thus, this collimator can provide a sensitivity of 905 cps and a spatial resolution of 3.73 mm for a source distance of 8 cm. Now that we have a count rate for the collimator, the detector performance should be considered, to address its compatibility with this collimator.

The conventional a-Se x-ray detectors operate with electric field 10 V/μm with the $W_{\pm} \approx 45$ eV at this field [22]. Taking this into account we can calculate how many counts each pixel will receive if the pixel size in a typical FPXI is 200 x 200 μm [22]. By geometry, each pixel will receive 2.61 cps or 1,216 EHP/s. For our assumptions this is the worst case scenario. But it's important to notice that the majority of seeds will be placed in the breast closer to the detector. For example when the seed is placed only 5 cm from the detector, it will improve resolution and sensitivity dramatically. In this case, the resolution will be 2.78 mm and the sensitivity is 1,626 cps. Each pixel will receive 4.69 cps or 2,187 EHP/s. In general, a shorter source distance to the detector will improve both resolution and sensitivity of the gamma camera.

In GATE, we build the collimator by inserting a lead box (parent) and filling it with a cubic array of hollow holes containing air. By defining a simple linear iteration with a repeat number (magnitude) and vector (direction), an array of hexagonal shaped holes are built into the lead box. The following macro demonstrates the construction process for the collimator:

```
/gate/SPECThead/daughters/name                    collimator
/gate/SPECThead/daughters/insert                  box
/gate/collimator/geometry/setXLength              3.8 cm
/gate/collimator/geometry/setYLength              10. cm
/gate/collimator/geometry/setZLength              10. cm
/gate/collimator/placement/setTranslation         -2. 0. 0. cm
/gate/collimator/setMaterial                      Lead

# Insert the first hole of air in the collimator
/gate/collimator/daughters/name                   hole
/gate/collimator/daughters/insert                 hexagone
/gate/hole/geometry/setHeight                     3.8 cm
/gate/hole/geometry/setRadius                     0.058 cm
/gate/hole/placement/setRotationAxis              0 1 0
/gate/hole/placement/setRotationAngle             90 deg
/gate/hole/setMaterial                            Air

# Repeat the hole in an array
/gate/hole/repeaters/insert                       cubicArray
/gate/hole/cubicArray/setRepeatNumberX            1
/gate/hole/cubicArray/setRepeatNumberY            134
/gate/hole/cubicArray/setRepeatNumberZ            113
/gate/hole/cubicArray/setRepeatVector             0. 0.14  0.242 cm

# Repeat these holes in a linear iteration
/gate/hole/repeaters/insert                       linear
/gate/hole/linear/setRepeatNumber                 2
/gate/hole/linear/setRepeatVector                 0. 0.069  0.121 cm
```

Once the detector has been fully constructed, it is useful to open *visualization* in GATE, to verify that the geometries and placements are correct. Parameters can also be modified for viewing the geometry at different angles and scale. This is important to see the collimator holes, which can only be shown in detail at a closer field-of-view (FOV). In the visualization window, the fully constructed collimator is displayed below in Fig. 2.5.

Figure 2.5 The collimator geometry is shown here, constructed with the parameters: d = 1.2 mm, l = 38 mm and t = 0.2 mm. a) and b) windows show oblique views of the collimator face and c) window shows the detailed hexagonal hole structure, as viewed on the collimator face.

We can also experiment with possible collimator materials as in Fig. 2.6. Firstly, by setting the collimator to air, it is shown that there is no attenuation and almost no scattering from the source to the detector face. In the case of plexiglass and plastic, there is very little attenuation with a great deal of scattering. The runs with high Z materials like lead, copper and tungsten show the most attenuation with very minimal to no backscatter from the collimator.

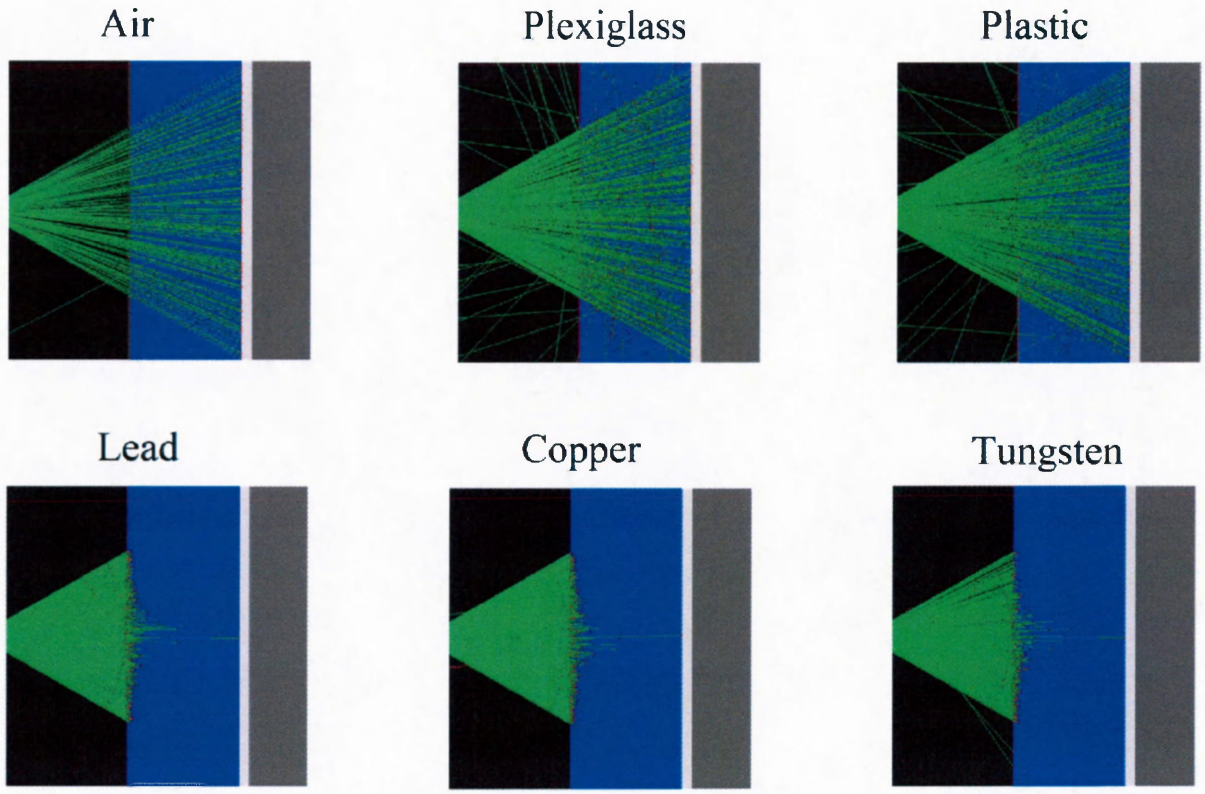

Figure 2.6 Different collimator materials are simulated here to shown the effects of scattering and attenuation. Low Z materials like plexiglass and plastic have very minimal attenuation and cause significant scattering while high Z materials like lead, copper and tungsten all demonstrate very high attenuation of incident photons.

Essentially, lead, copper or tungsten would be appropriate collimator materials to use, depending on the manufacturing constraints to build a collimator of such materials. To maximize attenuation so that optimum collimator resolution can be achieved, and to agree with the theoretical calculations previously shown, the collimator material of choice will be lead.

2.2.3. Defining the sources

Although ^{103}Pd has a mean energy emission of *21 keV*, for greater accuracy, the emission is of several low energy γ-rays and a few higher-energy ones. All the photon energies and fraction of those emissions are outlined in Table 2.2 from ICRP Publication 38, *Radionuclide Transformations Energy and Intensity of Emissions*, (Pergamon Press, 1983) [57].

Table 2.2 The Emission energies of ^{103}Pd seeds, sorted by their relative yields. The mass energy absorption coefficients for those energies are also shown.

Energy (MeV)	Yield (γ-rays/disintegration)	Mass Energy Absorption Coefficient in Air (cm^2/g)
0.02022	0.375	0.524
0.02007	0.198	0.539
0.02272	0.0660	0.365
0.02317	0.0174	0.343
0.0227	0.0348	0.366
0.3574	0.00022	0.0292
0.4971	0.000040	0.0296

The most accurate way to input source data into GATE is by specifying all energies and their respective yields. Another method to take all energies into account is by calculating the effective energy. The effective energy is calculated by the exposure weighting formula:

$$E_{eff} = \frac{\sum_i E_i y_i \left(\frac{\mu_\gamma}{\rho}\right)}{\sum_i y_i \left(\frac{\mu_\gamma}{\rho}\right)} \tag{2.9}$$

where E_i is the energy of the i^{th} photon, y_i is its yield, and $^{\mu_\gamma}/_{\rho}$ is the mass energy absorption coefficient [7]. For ^{103}Pd, the effective energy, $E_{eff} = 20.5\ keV$. Energies and yields are specified as a histogram source input, less the energies with negligible yields, along with a defined minimum energy of 20.07 keV and maximum of 23.17 keV. The shape is defined as a cylinder with dimensions in agreement with the previous diagram shown for a ^{103}Pd seed. A volume emission is specified which means the emission occurs along all points on the seed, not just as a

small point source. Finally, the activity of 2 mCi and half-life of 17 days is specified. For more than one seed, the macro below is simply iterated:

```
/gate/source/addSource                      seed1
/gate/source/seed1/gps/centre               0   0   0   cm
/gate/source/seed1/gps/type                 Volume
/gate/source/seed1/gps/shape                Cylinder
/gate/source/seed1/gps/radius               0.4 mm
/gate/source/seed1/gps/halfz                2.5 mm
/gate/source/seed1/gps/particle             gamma
/gate/source/seed1/gps/energytype           User
/gate/source/seed1/gps/hist/type            energy
/gate/source/seed1/gps/emin                 20.07 keV
/gate/source/seed1/gps/emax                 23.17 keV
/gate/source/seed1/gps/histpoint            0.02007   0.198
/gate/source/seed1/gps/histpoint            0.02022   0.375
/gate/source/seed1/gps/histpoint            0.02270   0.0348
/gate/source/seed1/gps/histpoint            0.02272   0.0660
/gate/source/seed1/gps/histpoint            0.02317   0.0174
/gate/source/seed1/setForcedUnstableFlag    true
/gate/source/seed1/setForcedHalfLife        1468800 s
/gate/source/seed1/gps/angtype              iso
/gate/source/seed1/setActivity              0.002 Ci
```

2.2.4. Digitizer setup

The digitizer module mimics the electronics of the gamma camera, serving functions such as energy blurring and energy window (for scatter rejection). The adder is the most important digitizer component as its function is to take each individual hit and cumulatively count each to generate a histogram. This is the pulse-height spectrum which shows # counts vs. energy. In this regard, the adder analogous to a photon counter, progressively adding counts for energies deposited from the start of the run to the end. With the intent of simplifying the readout electronics for this a-Se gamma camera, it is desirable to exclude an energy window completely, such that discriminator circuitry in the detector electronics will not be required. This will make the gamma camera electronics much cheaper than those of a CdZnTe gamma camera. Energy blurring is used to mimic noise and smear the photopeak based on predefined energy resolution. For example, by defining an energy resolution of $\pm$ *10%* with *21 keV* energy of reference, some of the deposited energies will take some value in the range $\pm$ *2.1 keV* when they are read out. This essentially creates a Gaussian energy distribution with the mean energy *~21 keV* and width, *~2.1*

keV. An energy window, as mentioned in the previous chapter, is a way for the electronics to reject photons above and below the specified thresholds. This is especially important at higher energies, where Compton scattering is more prominent. At this point, we simulate with no energy blurring or window, to see the full energy deposition process and visualize any Compton scattering which would otherwise become blurred by the photopeak itself. Blurring will be incorporated following PHS experiments in Chapter 3 when a-Se energy resolution will be determined. The following macro includes the adder, energy blurring and window:

```
/gate/digitizer/Singles/insert adder

# ENERGY BLURRING
/gate/digitizer/Singles/insert blurring
/gate/digitizer/Singles/blurring/setResolution              0.10
/gate/digitizer/Singles/blurring/setEnergyOfReference       20.5 keV

# ENERGY WINDOW
/gate/digitizer/Singles/insert thresholder
/gate/digitizer/Singles/thresholder/setThreshold            0 keV
/gate/digitizer/Singles/insert upholder
/gate/digitizer/Singles/upholder/setUphold                  80 keV
```

2.2.5. Physical processes

In the GATE simulation presented, the following physics processes are activated: photoelectic, Compton, Rayleigh, e^- ionization and multiple scattering.

The photoelectric CS calculation is complex due to the combination of the electron wave functions. It is simulated by using a parameterized photon absorption CS to determine the mean free path, atomic shell data to determine the energy of the ejected electron, and the K-shell angular distribution to sample the direction of the electron. The CS depends on the Z of the material and as shown in Chapter 1, photoelectric effect is favored by high Z materials. In the current implementation the relaxation of the atom is not simulated, but instead is counted as a local energy deposit. For low energy process, the de-excitation of the atom is simulated [53].

For Compton scattering, an empirical CS formula is used, which reproduces the CS data down to 10 keV. The final state of scattered photons is generated following the Klein-Nishina formula

[58]. For low energy incident photons, the simulation of the Compton scattering process is performed according to the same procedure used for the standard Compton scattering simulations, with the addition that Hubbel's atomic form factor [59] is taken into account. The angular and energy distribution of the inelastic scattered photon is then given by the product of the Klein-Nishina formula and the Hubbel form factor.

In Rayleigh scattering processes, the direction of the photon is the only modified parameter and no energy is transferred to the target. Thus, no atoms are excited, or ionized. At high energies, the CSs of Rayleigh scattering are very small and are neglected. For these reasons, the Rayleigh process is defined only for low energy and Penelope models [53] as in the macro below:

```
/gate/physics/addProcess PhotoElectric
/gate/physics/processes/PhotoElectric/setModel PenelopeModel

/gate/physics/addProcess Compton
/gate/physics/processes/Compton/setModel PenelopeModel

/gate/physics/addProcess RayleighScattering
/gate/physics/processes/RayleighScattering/setModel PenelopeModel

/gate/physics/addProcess ElectronIonisation
/gate/physics/processes/ElectronIonisation/setModel StandardModel e-
/gate/physics/addProcess MultipleScattering e-
/gate/physics/processes/MultipleScattering/setModel StandardModel e-
```

The physics models in GATE can also calculate the ionization potentials for materials, that is, the energy required to release (or ionize) a single electron from the valence band. A charged particle passing through matter loses energy due to inelastic collision with atomic electrons of the material. Lost energy is transferred to the atom causing ionization or excitation. The ionization energy loss is calculated using the Bethe-Bloch formula [60]. The particle energy loss E is divided into continuous energy loss and production of secondary electrons. The production threshold is defined as the minimum energy above which secondary particles will be produced and tracked. In materials such as a-Se and CdZnTe, secondary electrons average range is less than 10 μm, which is only 10% of the thickness used. Therefore, secondary electrons are modeled as depositing their energy in the same location as they originated [6]. For accuracy, the ionization values of 5.9 eV for a-Se and 4.43 eV for CdZnTe are specified [54].

As GATE utilizes data libraries from several high energy and low energy particle physics experiments, these are taken into account when simulating interactions via models, or more specifically, scattering and absorption CSs.

2.2.6. Scattering cross-sections

Electromagnetic processes are used to simulate the electromagnetic interaction of particles with matter. Essentially, scattering CSs are hypothetical areas used to describe a probability of some scattering or absorption event. The MC method in GATE essentially samples each photon interaction with the CSs for each material it encounters. The mean free path of a photon, $\lambda(E)$, for a given energy, E, also called the interaction length, can be given in terms of the total CS:

$$\lambda(E) = \left(\sum_i |n_i \, \sigma(Z_i, E)| \right)^{-1} \tag{2.10}$$

where n_i is the number of atoms per volume of the material and $\sigma(Zi,E)$ is the CS of the process for atom i composing the material [53]. For selenium, the CS data from NIST [54], presented in Fig. 2.7, photoelectric absorption is orders of magnitude large compared to Rayleigh and Compton scattering. At our energy of interest, the CS is $\sim 10^2$ larger for photoelectric than Compton and $\sim 10^3$ larger than Rayleigh. Thus, we can expect almost all interactions with a-Se to be photoelectric with very minimal Compton scattering and even less Rayleigh. Scattering in the phantom is expected to be the primary source of energy loss since lower Z elements, such as those of breast tissue, will have higher scattering CSs than higher Z elements like selenium and lead.

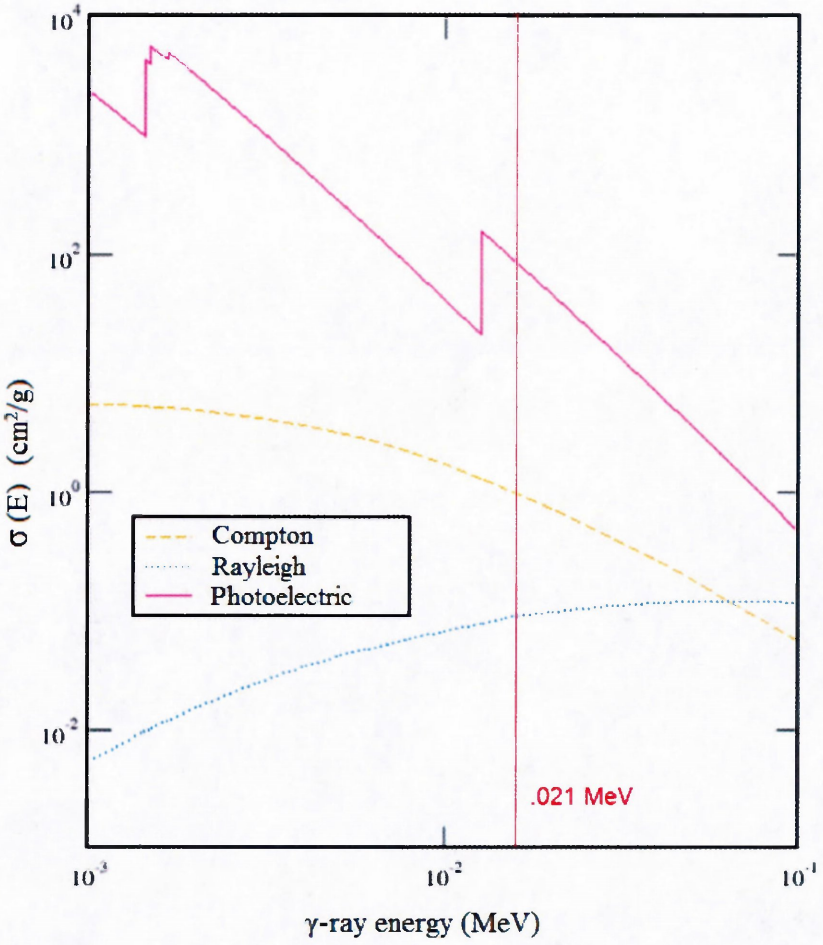

Figure 2.7 The scattering CS data plotted against photon energy for selenium [54]. At low energies, photoelectric absorption dominates over the other scattering process.

CS per atom and mean free path values are tabulated during initialization. In Geant4, three CS models are available for electromagnetic processes. These are the Geant4 implementation of the physics models developed for GATE: Standard processes, effective between 1 keV and 100 TeV; low energy processes, effective between 250 eV and 100 GeV; and *PENELOPE* (PENetration and Energy LOss of Positrons and Electrons) processes, effective between 250 eV and 1 GeV [53]. The PENELOPE models have been specifically developed for Monte Carlo simulation and great care was given to the low energy description (i.e. atomic effects, etc.). This is the physics model of choice in these simulations.

Models and CSs are based on the theoretical calculations and on extrapolation of evaluated data. For the standard processes based on data, models and CSs rely on parameterizations of these data. Because atomic shell structure is more important in most cases at low energies, the low energy processes make direct use shell CS data. The data used for the determination of CSs and for sampling of the final state are extracted from a set of freely distributed evaluated data libraries: EPDL97 (Evaluated Photons Data Library), EEDL (Evaluated Electrons Data Library), EADL (Evaluated Atomic Data Library), stopping power data and binding energy data from Scofield, "*Theoretical photoionization cross-sections for 1 to 1500 keV*" [53,61].

2.2.7. Energy and spatial output

In agreement with the important output information which the gamma camera provides, we focus on both the energy and position data. The energy data gives insight into the mechanisms of energy deposition in the detector, with the majority of counts at the photopeak and scattering events at lower energies. For each photon hit on the detector, the output file records the: a) *eventID*, with respect to all emissions; b) *sourceID*, with respect to all sources; c) origin of emission coordinates *X,Y,Z*; d) detected coordinates *X,Y,Z*; e) time of hit; f) energy deposited; and finally g) number of scattering interactions with the detector and/or other components. An ID is also assigned corresponding to where the scatter occurred. For example, if a hit was scattered once in the phantom before reaching the detector, it is assigned a count of one in the *ComptonID* data and labeled *phantom_phys*, indicating it occurred in the phantom physical volume.

2.3. Results and discussion

The results presented below are simulated without energy discrimination or blurring which makes it simpler to examine the full energy deposition and Compton scattering regimes in the energy spectrum. Position data is unaffected by energy blurring, only by scattering. From Equation 1.8, the primary scattering range up to complete backscatter (180°) at the Compton edge, E_{CE}, for ^{103}Pd energies of $E_\gamma = 20.5\ keV$, $E_\gamma = 22.7\ keV$ and rest mass energy, $m_e c^2 = 511\ keV$ is:

$$E_{scatter} = \frac{511\ keV}{\left(\frac{511}{20.5} + 1\right) - cos\theta} \tag{2.11}$$

$$For\ up\ to\ 180°\ (Compton\ edge\ or\ backscatter) \rightarrow\ E_{CE} = 18.9\ keV\ to\ 20.8\ keV$$

Therefore, Compton scattering can occur quite close to the photopeak energy of 21 keV. If we introduce energy blurring, the scattering regime may be obscured by the broadening of the photopeak. The first results presented are for one ^{103}Pd seed with a-Se detector, simulated for one minute and assuming a $W_{\pm}$ of 5.9 eV. The seed is placed in the center of the breast phantom, 50 mm from the collimator face. The numerical data with related energy, scattering, and position data are presented below.

Table 2.3 Simulation data for 1 seed imaged for 1 min. with a-Se gamma camera. Percentages are in relation to the total number of interaction processes including those from the detector, phantom and surroundings.

Number of emitted γ-rays	4.43996 x 10^9	Scatter order 1	76.7183 %
Number of detected γ-rays	9.9044 x 10^4	Scatter order 2	17.7302 %
Photoelectric absorption	91.4241 %	Scatter order 3	4.32999 %
Scatter in the phantom	7.6528 %	Scatter order 4	0.911577 %
Scatter in the collimator	0.0020193 %	Scatter order >4	0.309933 %
Scatter in the a-Se layer	0.698901 %		
Scatter in other components	0.22218 %		

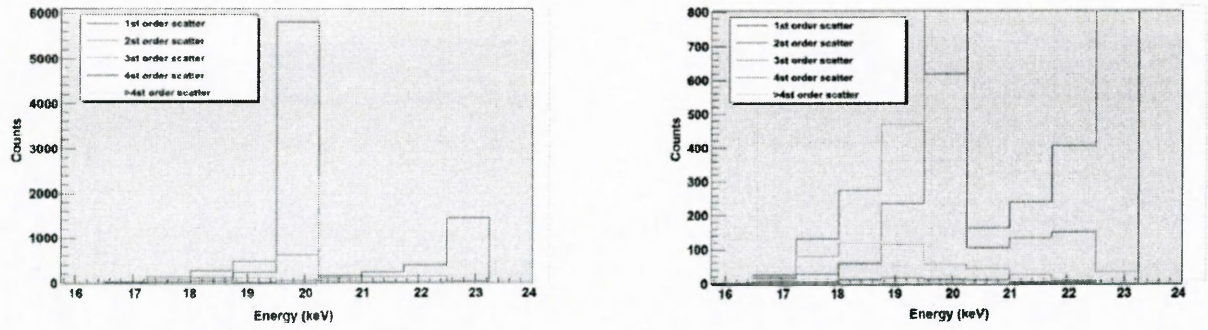

Figure 2.8 Scatter order of all events for a-Se, in full scale (left) and detailed view (right), showing number of counts which are scattered for each order and at which energies.

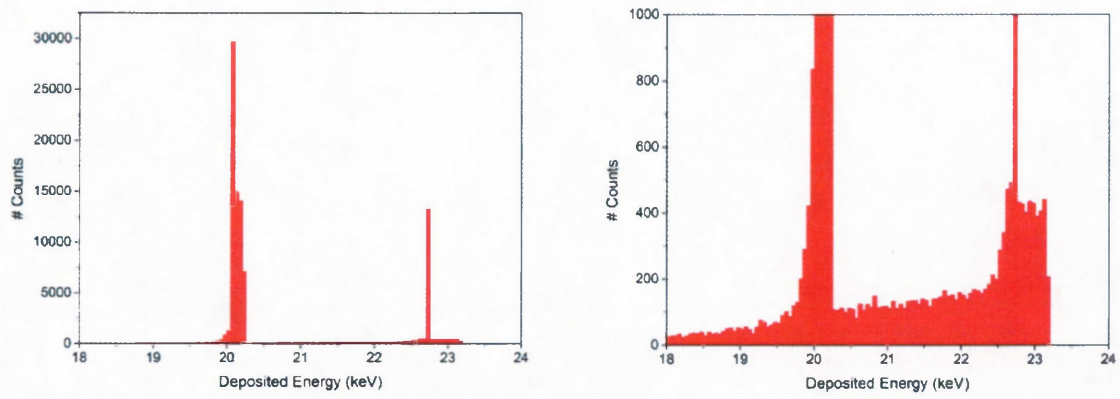

Figure 2.9 Full scale (left) and detailed (right) views of pulse-height energy data for 1 seed imaged with a-Se gamma camera with $W_{\pm}$= 5.9 eV.

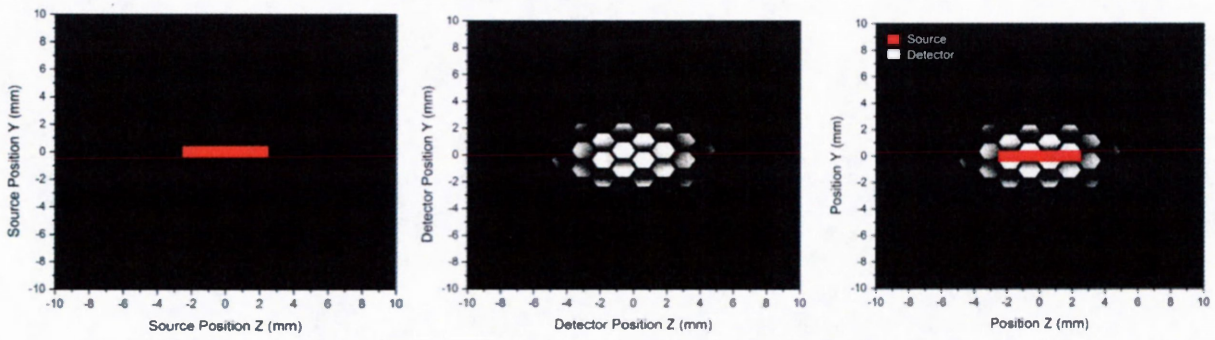

Figure 2.10 Position data for 1 seed imaged with a-Se, showing the spatial distribution of emissions from the source (left), the corresponding distribution seen at the detector (middle), and both those data sets superimposed (right). The detector images are set at 20% brightness, to improve contrast and edge definition.

Almost 100,000 photons reach the detector in 60 s, which agrees within 1.5% of our previous collimator sensitivity calculation of 1626 cps or 97,560 cpm. From Table 2.3, photoelectric absorption dominates at 91% with only 7% scattered events due to the phantom and only 0.7% scattering in the a-Se layer. Scattering in other components such as the back-compartment of the SPECThead and shielding is minimal and scattering in the collimator is negligibly small. The majority of photons scatter only once (76%). Much less will scatter a second (17%) and third (4%) time and the majority of these occur at energies lower than 20 keV, indicated in Fig. 2.8.

In the full scale view (Fig. 2.9), the two sharp photopeaks represent the bulk of photon yields corresponding to Table 2.2. The first major peak on the left lies around 20.2 keV, while the minor peak to the right is around 22.7 keV. The maximum peak corresponds to 23.17 keV, with no energies greater than this level. This should be expected since scattered photons which reach the detector will all have lower energies than the ones which undergo photoelectric absorption. The Compton scattered events are shown as the "tails" from each photopeak, decreasing toward the lower energies. This is also related to the scattering order as higher orders of scattering will lose more energy before deposited. Relative to the maginitude of the photopeaks, Compton scattering is shown to be negligibly small in comparison, with less than 200 counts for most scattered energies. Since the expected Compton edges at 18.9 and 20.8 keV are difficult to distinguish, it is likely that insignificant backscatter occurs in the phantom, collimator and detector. This scattering range is seen in the data, as the majority of counts between in photopeak are related to the yields between 20.5 and 22.7 keV. The Compton scattered and multiple scattered ranges are almost non-existent at energies less than 18 keV. Rayleigh scattering is insignificant as no events of this nature were detected at all.

As the position data in Fig. 2.10 shows, the images take the shape of the hexagonal collimator holes which diminish in brightness away from the origin. This is expected since there should be very few photons passing through the collimator septa. With 100% brightness, the small amount of photons, oblique to the collimator, appear as "cloud", effectively smearing the image. This smear degrades spatial resolution and contrast of the imaged seeds. With image post-processing and reconstruction, algorithms could be implemented to reduce this effect. With simple image processing, the brightness in the spatial data has been set at 20%, to improve the contrast of the image against the background.

We also simulate one ^{103}Pd seed with CdZnTe detector for one minute. We can then compare the energy and position data to that of a-Se. As CdZnTe is the baseline for a-Se, it is important to show how CdZnTe performs in an identical simulation. With only the photoconductor material changed to CdZnTe and the $W_{\pm}$= 4.43 eV, the following results include the same parameters as the previous simulation with a-Se.

Table 2.4 Simulation data for 1 seed imaged for 1 min. with CdZnTe detector. Percentages are in relation to the total number of interaction processes including those from the detector, phantom and surroundings.

Number of emitted γ-rays	4.42384×10^{9}	Scatter order 1	66.8992 %
Number of detected γ-rays	8.0964×10^{4}	Scatter order 2	25.814 %
Photoelectric absorption	91.0335 %	Scatter order 3	5.81395 %
Scatter in the phantom	7.95865 %	Scatter order 4	1.25581 %
Scatter in the collimator	0.00123512 %	Scatter order >4	0.22338 %
Scatter in the CdZnTe layer	0.47799 %		
Scatter in other components	0.306445 %		

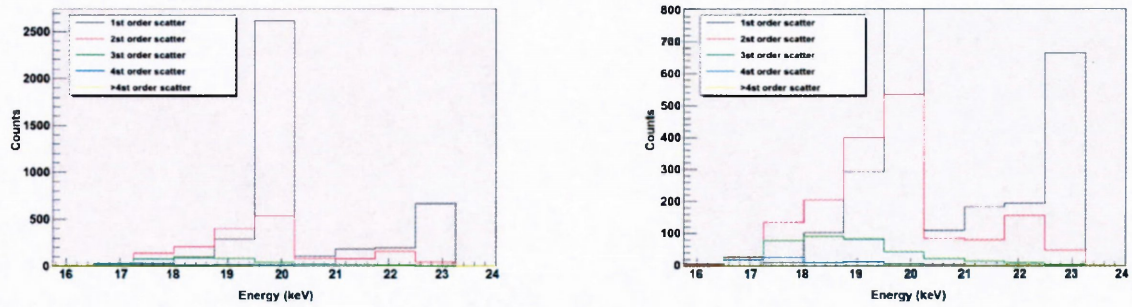

Figure 2.11 Scatter order of all events for CdZnTe, in full scale (left) and detailed view (right), showing number of counts which are scattered for each order and at which energies.

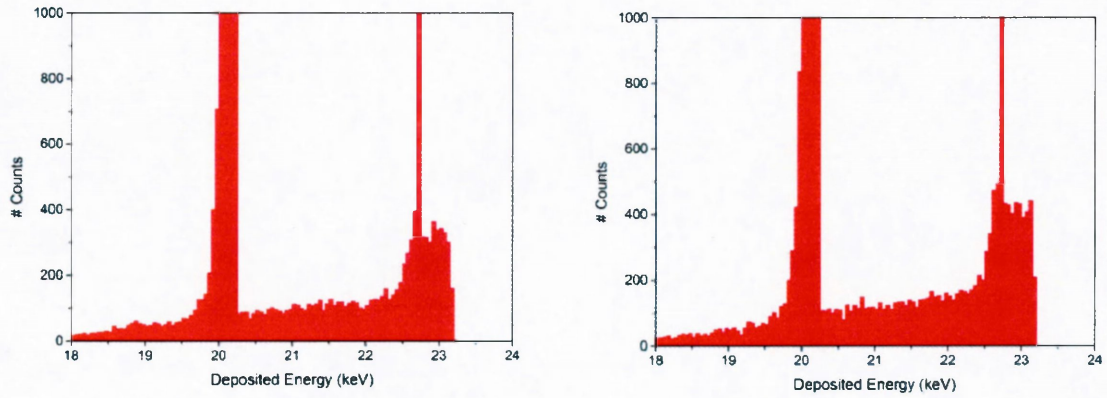

Figure 2.12 Comparison in detailed energy data for 1 seed imaged with CdZnTe camera (left) and a-Se camera (right) simulated for 1 min and $W_{\pm}$ of 4.43 eV and 5.9 eV respectively.

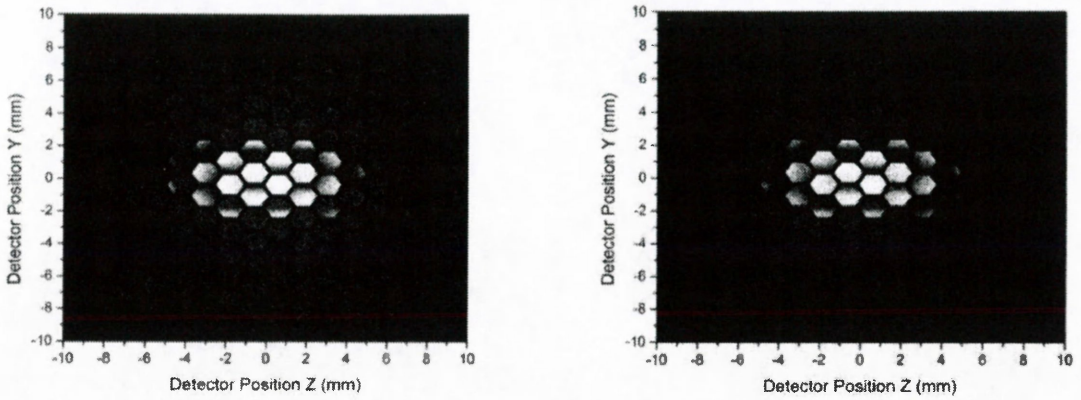

Figure 2.13 Comparison of position data for 1 seed imaged with CdZnTe camera (left) and a-Se camera (right), showing almost identical spatial distributions. Both images are set at 20% brightness, to improve contrast and edge definition and conditions are identical in each case.

The results presented from 1 seed imaged for 1 minute with both a-Se and CdZnTe detectors, demonstrate that each material is capable of stopping 21 keV γ-rays with photoelectric absorption accounting for >90% of the energy spectrum. In comparison, CdZnTe shows slightly less scattering in the crystal layer (~0.5%) with scatter orders similar to that a-Se. Energy data in Fig. 2.12 are very similar in both a-Se and CdZnTe, and as in Fig. 2.13, images produced by each detector are almost identical. Since the detector material is the only parameter which is changed in each case, the spatial resolution relies more on the collimator design than the material itself. Furthermore, it is evident that a-Se can provide the stopping power and detection efficiency comparable to CdZnTe.

The next results are with 5 seeds, imaged with the same a-Se camera as in the 1 seed case. The intent of this arrangement is to examine how closely two adjacent seeds can be placed, without smearing each image into one. For simplicity, the origins of each seed are spaced 10 mm apart, with edge spacing in Z = 5 mm and Y = 9.2 mm calculated from the dimension of a seed (5 mm, 0.8 mm). Figure 2.14 shows the 5 seed position data and Fig. 2.15 gives a general view on how close two seeds can be placed together and still be distinguishable by the detector.

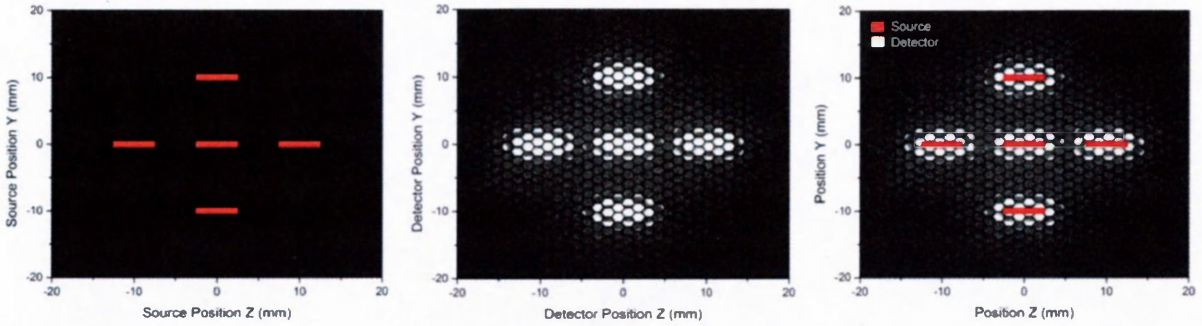

Figure 2.14 Position data for 5 seeds imaged with a-Se camera, showing the spatial distribution of emissions from the source (left), the corresponding distribution seen at the detector (middle), and both those data sets superimposed (right). The detector images are set at 20% brightness, to improve contrast and edge definition.

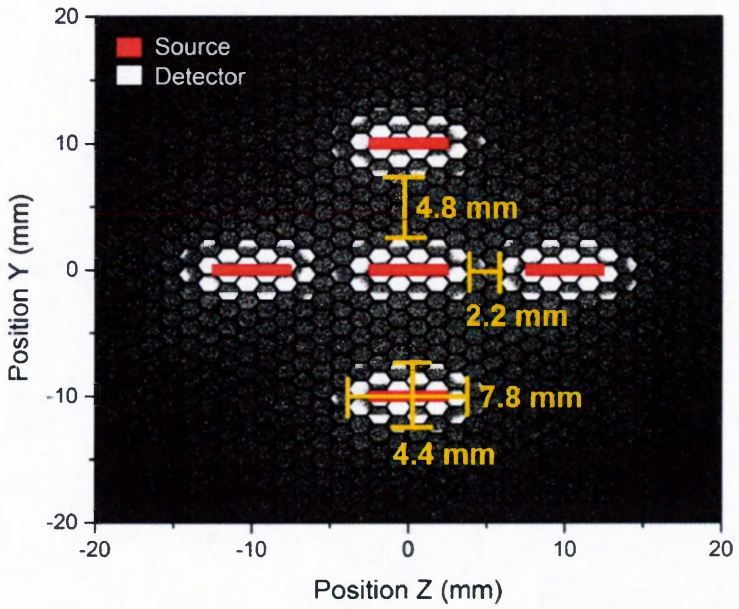

Figure 2.15 The edge-to-edge image dimensions for a single seed and between adjacent seeds in a 5 seed distribution. The seeds are spaced 5 mm apart in Z-coordinate and 9.2 mm in the Y-coordinate. This corresponds to placing their origins exactly 10 mm apart in each coordinate.

Finally, we simulate a hypothetical PBSI treatment plan, using 60 seeds, imaged for 60 s. The total seed distribution is divided into 3 planar layers, each placed 10 mm deeper into the breast. There is the superficial layer, with 27 seeds; intermediate layer, with 17 seeds; and the deepest

layer, with 16 seeds. Therefore, the superficial layer is 40 mm from the collimator face, the intermediate is at 50 mm and the deepest at 60 mm.

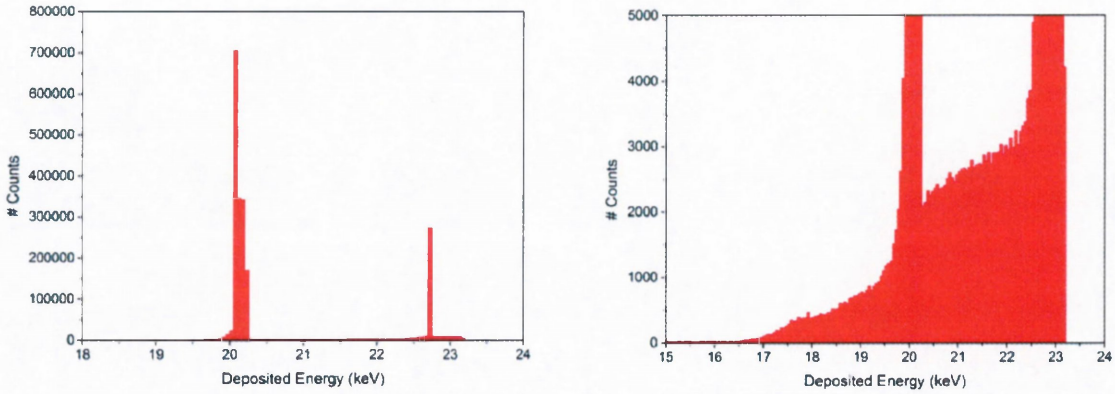

Figure 2.16 Full scale (left) and detailed (right) views of pulse-height energy data for 60 seeds imaged with a-Se gamma camera with $W_{\pm}$= 5.9 eV.

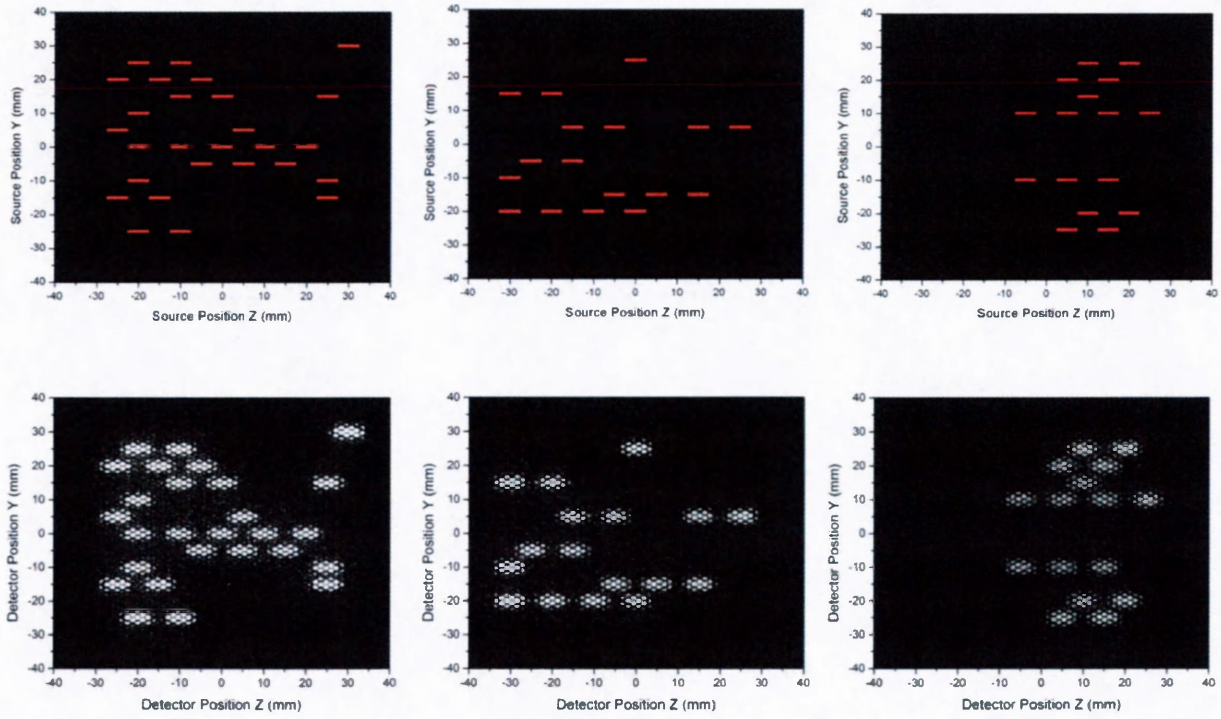

Figure 2.17 The hypothetical seed distribution consisting of 3 layers: superificial layer (left) with 27 seeds, intermediate layer (middle) with 17 seeds, and the deepest layer (right) with 16 seeds. The resulting images for those distributions are shown below each. The minimum spacing between adjacent seeds in both Y and Z directions is 5 mm. Each seed is 5 mm in length by 0.8 mm in width.

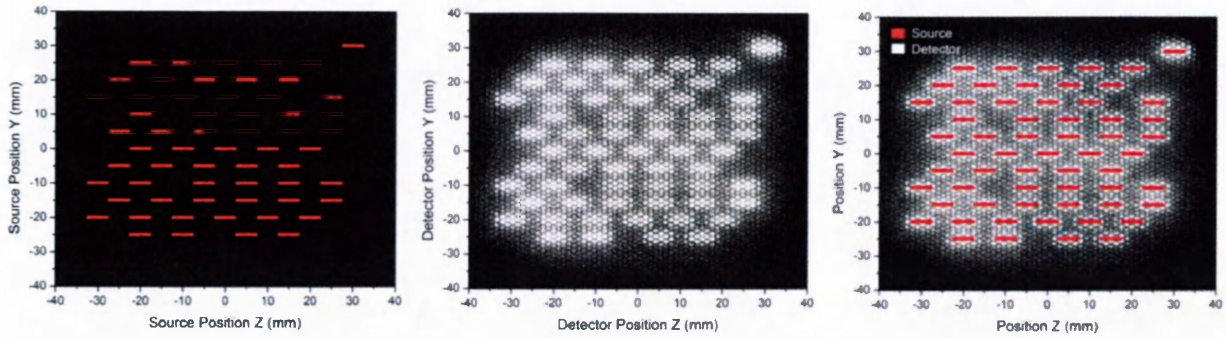

Figure 2.18 Position data at full brightness for 60 seeds imaged with a-Se camera, showing the spatial distribution of emissions from the source (left), the corresponding distribution seen at the detector (middle), and both those data sets superimposed (right).

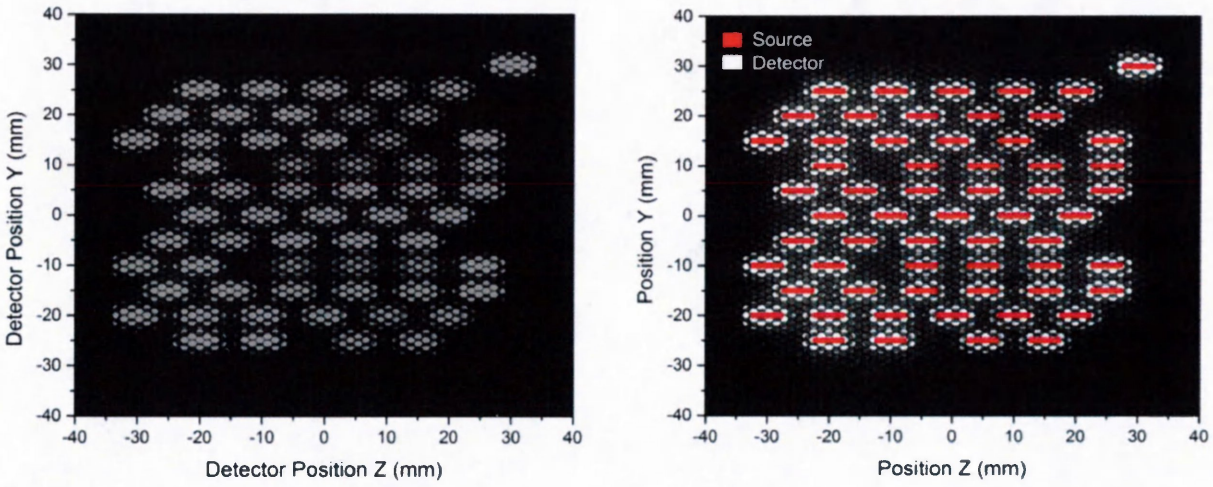

Figure 2.19 By lowering the brightness in the image processor, each seed is even more distinguishable from the next, as shown on the left. In the right image, the actual positions of seeds correspond much better to the edges of the imaged seeds at the detector.

As in the 1 seed simulation, Fig. 2.16 demonstrates much lower scattering counts than the photopeaks, which are non-existent less than 17 keV. Thus, when comparing relative scattering to the photopeaks in the energy data for 1 seed, 5 seeds and 60 seeds, all cases show negligible counts. Improving on the 5 seed distribution, we more carefully analyze the position data for the full distribution, specifically, in relation to pixels.

The next set of figures will examine the 60-seed distribution after only 10 s of imaging. If the intended pixel size of the a-Se detector is 200 x 200 μm, for an area of 10 x 10 cm, then the detector FOV will be 500 x 500 pixels. The FOV has been divided into pixels and the root-mean-square error (RMSE) values correspond to the localization error from source distribution to detector distribution for a specific emission. Each pixel can image a distribution shown in Fig. 2.20. From the data, the pixels represented with larger boxes receive about 42 photon counts, on average. This translates to 4.2 cps, only 11% difference from the theoretical count rate of 4.69 cps found with the collimator. The distribution as a whole, as in Fig. 2.21, is plotted to show the localization error (boxes) around the centroids of the seeds. For greater accuracy in position, each reconstructed seed image on the detector can be plotted as error bars with the centroids of each seed to exactly calculate the RMSE, or localization error in both Y and Z-coordinates (Fig. 2.22).

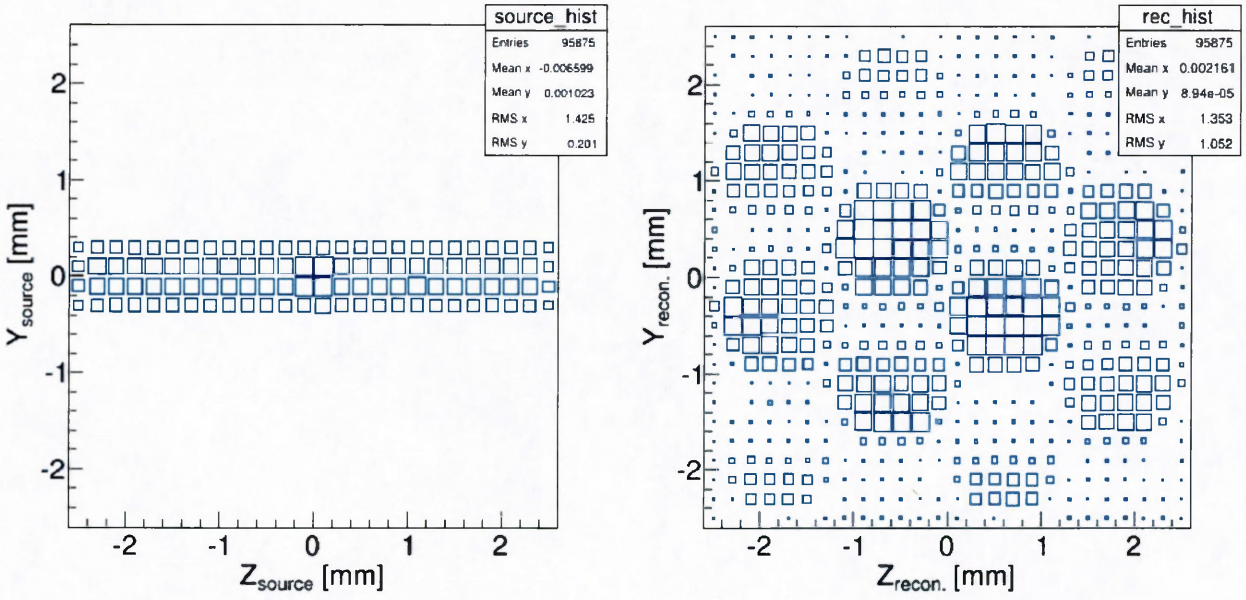

Figure 2.20 The pixelated distribution of ^{103}Pd emission shown on the left and the detector on the right, where each blue box is one 200x200μm pixel. The sizes of the boxes correspond to the relative number of emissions detected by each pixel. As the majority of detected events are from the center of the seeds, as shown in the source data, these boxes are largest.

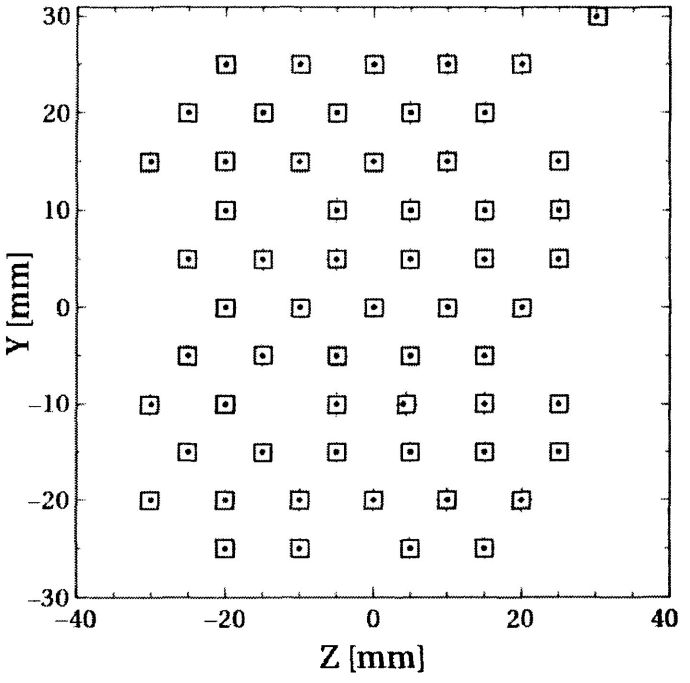

Figure 2.21 The spatial distribution of 60 ^{103}Pd seeds, shown as points, with their maximum localization error in Y and Z position indicated by the surrounding boxes.

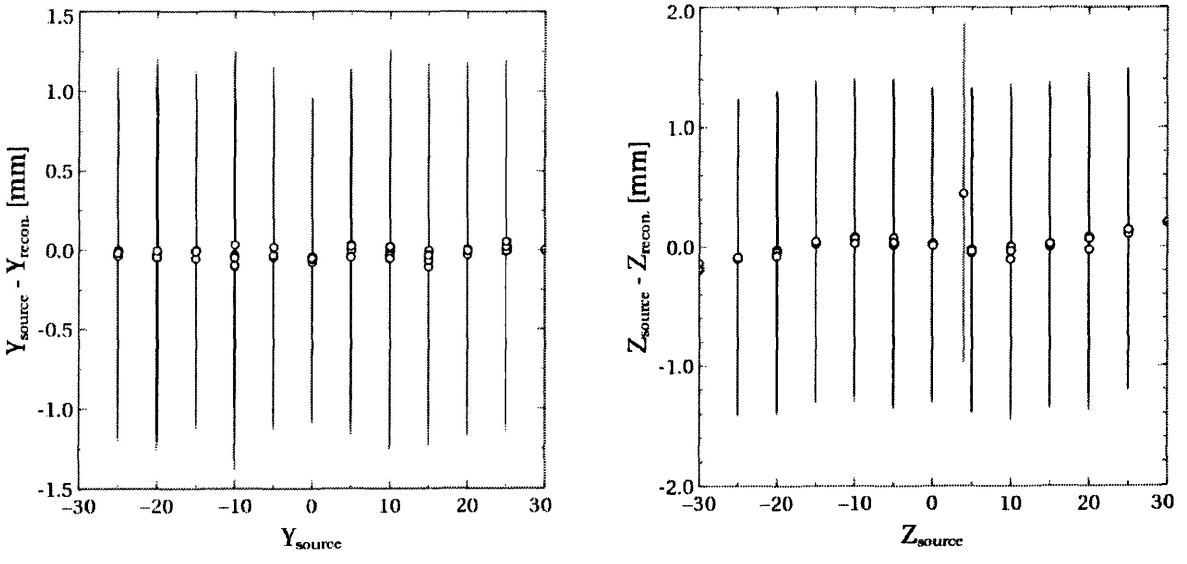

Figure 2.22 The maximum localization errors in reconstructing seed distribution for Y position (left) and Z position (right). The points represent actual seed positions while the error bars indicate the RMSE of their image reconstruction.

By interpolating Fig. 2.20, individual seeds can be localized to a maximum ~1.35 mm in the Z-coordinate and ~1 mm in the Y-coordinate. As expected, there is a greater error in the Z direction since this is along the length of the seed which contains more source emissions than the smaller width in the Y direction. Thus, for an imaging duration of just 10 s, this a-Se gamma camera could localize seeds within 1.3 mm. These results are quite comparable to those of Ravi et al., where seeds could be resolved within 1 mm, using two views after 24 s of imaging with a CdZnTe simulated camera [6]. By recalling Equation 2.4, the intrinsic spatial resolution of the a-Se detector, is determined:

$$R_{sys} = \sqrt{{R_{int}}^2 + {R_{coll}}^2}$$

And by using the calculated collimator and system resolutions of: 2.78 mm and 1.35 mm:

$$R_{int} = \sqrt{(2.78\,mm)^2 - (1.35\,mm)^2} = 2.43\,mm \tag{2.12}$$

2.4. Conclusions

In this chapter, we have demonstrated that a-Se could localize individual seeds to 1.35 mm in a 60-seed distribution, comparable to other CdZnTe camera systems [6]. With this design, the a-Se detector has an intrinsic resolution of 2.43 mm. From the energy data, Compton scattering is shown to be negligible, with much less than 1% of the photopeak counts. In principle, the GATE simulated energy and position data shows energy discrimination is not required for localizing seeds with this a-Se gamma camera.

Now that the capability of localizing seeds has been demonstrated, there is a requirement to test the photon counting abilities of a-Se for low energy γ-rays. This will be accomplished by pulse-height spectroscopy in the next chapter.

Chapter 3

Pulse-height spectroscopy with a-Se photoconductor

3.1. Pulse-height spectroscopy

PHS is a technique used to examine the amplitudes of signals from a radiation detector to determine the energies of radiations striking the detector, or to select for counting only those energies within a desired range. This is accomplished with detectors providing output signals proportional to radiation energy detected (photon counters), such as semiconductors. A pulse-height spectrometer consists of a radiation detector and its high-voltage power supply, preamplifier, amplifier, analog-to-digital converter (ADC) and multichannel analyzer (MCA). A pulse-height spectrum is a display showing the number of events detected (counts) versus the amplitude of those events. This is processed by the MCA. Figure 3.1 illustrates how a γ-ray source interacts with the a-Se radiation detector. Energy is transferred to the detector and shielding box through photoelectric and/or Compton scattering processes. A portion of the incident photon energy is transferred as kinetic energy to photoelectrons, Compton electrons, or positive-negative electron pairs, respectively, which in turn transfer their kinetic energy to the detector in secondary ionization events. Following the schematic in Fig. 3.1, an incident γ-ray can deposit its full energy to the detector in one of two ways: (A) a photoelectric interaction; or (B) one or more Compton scatters followed by a photoelectric interaction [11].

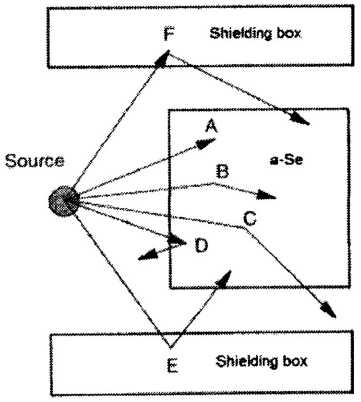

Figure 3.1 The illustrated trajectories and interactions of the γ-rays with the a-Se and surrounding shielding box.

If no γ-rays escape the detector, the charge generated, or number of EHP, is directly proportional to the number of photons which are incident. Ideally, the detector can then collect all charge generated from the exact same energy and display one sharp peak (a δ-function) on the energy scale. In this manner, each full energy interaction is accounted for and we now have a photon counting system. However, to account for all interactions and scattering, the photopeak is broadened from energy losses and stochastic particle interactions with the detector and components. In the partial interaction case, a photon can deposit only a fraction of its energy if it interacts by Compton scattering and the scattered photon escapes the detector (C). Although the scattered photon can ionize an electron, the remainder of energy is lost so this is not a full energy deposition process. Even if the incident photon interacts by the photoelectric effect, less than its total energy will be deposited if the inner-shell electron vacancy created by the interaction results in emission of a characteristic x-ray that escapes the detector (D). Our detector is enclosed in a shielded box to reduce effects of natural background radiation and nearby radiation sources, especially ambient light. We should then also consider photon interactions with this box which can give additional information in the pulse-height spectrum. An x-ray or γ -ray may interact in the shielding and deposit energy in the detector. There may be Compton scattering within the shield, with the scattered photon striking the detector (E), and/or a generated characteristic x-ray from the shield may interact with the detector (F). In each case, these energies will differ from the incident energies and we will see other peaks which differ from the photopeak. Fig. 3.2 shows how pulse amplitude relates to energy deposition and the most likely processes associated within each amplitude range [9].

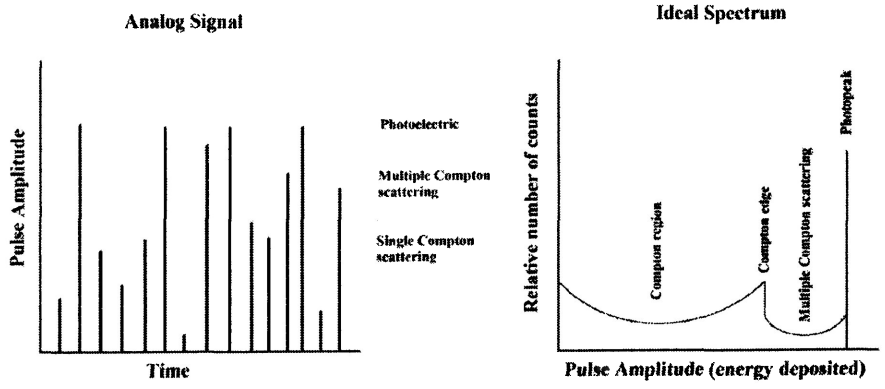

Figure 3.2 The relation of pulse amplitude to energy depostion and associated mechanisms at each interface.

For gamma cameras, energy selection is important for imaging because it provides a means to discriminate against γ-rays that have scattered in the body and therefore lost their positional information. By choosing a relatively narrow energy window in the PHA that is centered on the photopeak, only γ-rays that undergo no scattering or small-angle scattering will be accepted. Two different methods can be used to select the photopeak events. A modern gamma camera has an energy resolution around 10% for a standard radionuclide ^{99m}Tc which emits 140 keV γ-rays [9]. The energy resolution of a gamma camera depends on the energy of incident γ-rays and determines the size of the energy window which can be used for discrimination. For example, defining an energy window which is less than the resolution of the detector will cut out photopeak events which add to the intensity of the PHS signal. This can result in longer collection times to achieve the desired number of counts for higher signal. In the other case, an energy window greater than the energy resolution will count more background noise and scattering events. However, for 60 keV and lower energies, Compton scattering may be insignificant, as seen previously with GATE at 21 keV. Similarily, by using Equation 1.8, the Compton edge, E_{CE}, for ^{241}Am energy of $E_\gamma = 60\ keV$ and rest mass energy, $m_e c^2 = 511\ keV$ is calculated by:

$$E_{scatter} = \frac{511\ keV}{\left(\frac{511}{60} + 1\right) - cos\theta} \tag{3.1}$$

$$For\ up\ to\ 180°\ (Compton\ edge\ or\ backscatter) \rightarrow E_{CE} = 48.6\ keV$$

PHS records energy pulses based on the amount of energy deposition in the detector in order to reject scattering from pulse amplitudes. This is the principle on which PHA electronics function, as will be discussed in the materials and methods of the PHS experiments.

3.2. Materials and methods

The function of the PHA electronic system in pulse-height spectroscopy is the collection of the EHPs produced from the signal pulses, the processing of those pulses, and sorting them by their energy, or to more accurately measure sensitivity, number of EHPs. A simpified PHA system is shown below in Fig. 3.3, followed by the actual laboratory apparatus in Fig. 3.4. The process can be described by the following steps [11]:

1. Photon interacts with the photoconductor and produces EHPs.
2. Applied bias voltage sweeps EHP across thickness of sample.
3. Current produced by EHP forms signal pulse.
4. Pulse size is increased with a preamplifier.
5. Pulse is further intensified and shaped with amplifier.
6. Pulse intensity is converted into numerical value using ADC.
7. Numerical values are sent to MCA for photon counting.

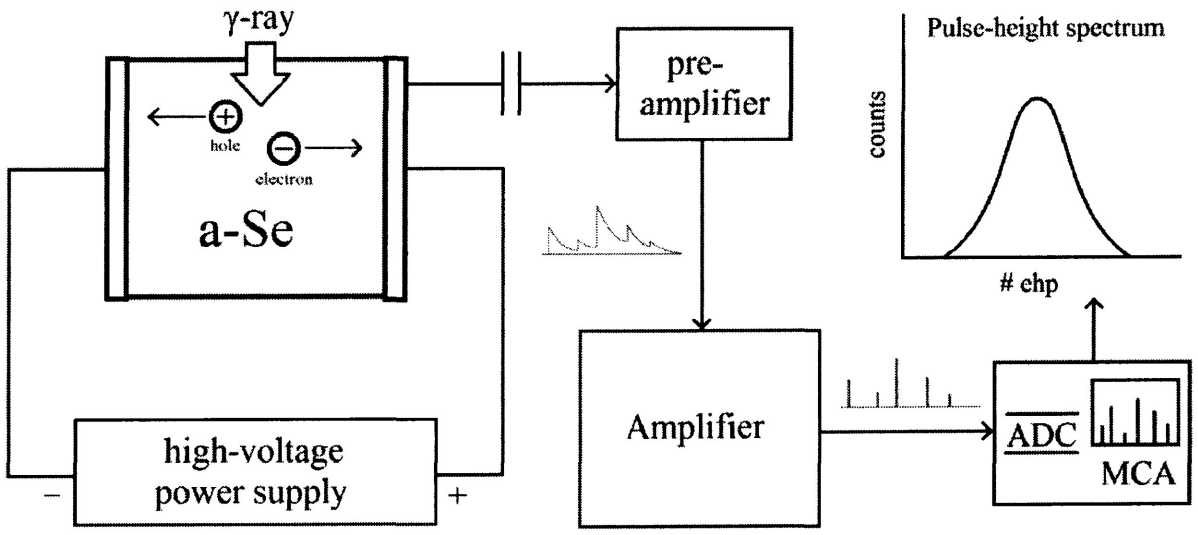

Figure 3.3 The PHA hardware is demonstrated, where a γ-ray strikes the a-Se layer, generating several EHPs. The HV power supply provides an electric potential across the a-Se, allowing the EHPs to drift to the electrodes on either side. These are then collected by a capacitor and sent to the preamplifier, generating a signal pulse. The pulse is sent to the amplifier which intensifies and shapes the pulse for the ADC which the MCA can then digitally readout as a pulse-height spectrum.

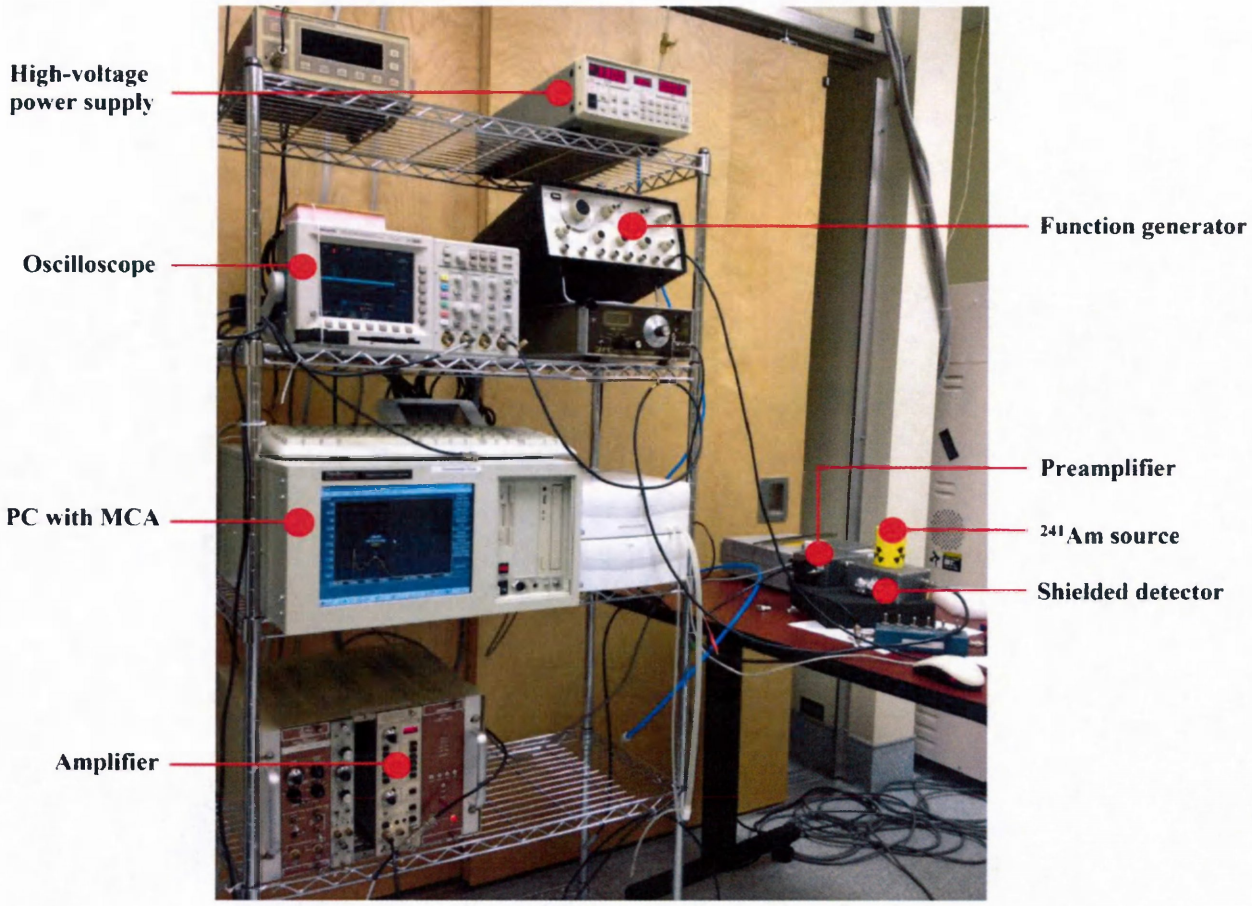

Figure 3.4 The labelled apparatus for PHS experiments in the lab is depicted here. The components include: the high-voltage power supply, oscilloscope, MCA, amplifier, preamplifier, function generator, ^{241}Am source, and the a-Se detector, enclosed in an aluminum shielding box to reduce background noise.

3.2.1. Multichannel analyzer

The multichannel analyzer (MCA) performs the essential functions of collecting the data, providing a visual monitor, and producing output, either in the form of final results or data for later analysis. It essentially consists of an analog-to-digital converter (ADC), control logic, memory and display. All this can be accomplished with a computer equipped with an MCA card and analysis software. We use the software *Aptec MCA* which can display our collected spectrum in real-time, as depicted in Fig. 3.5.

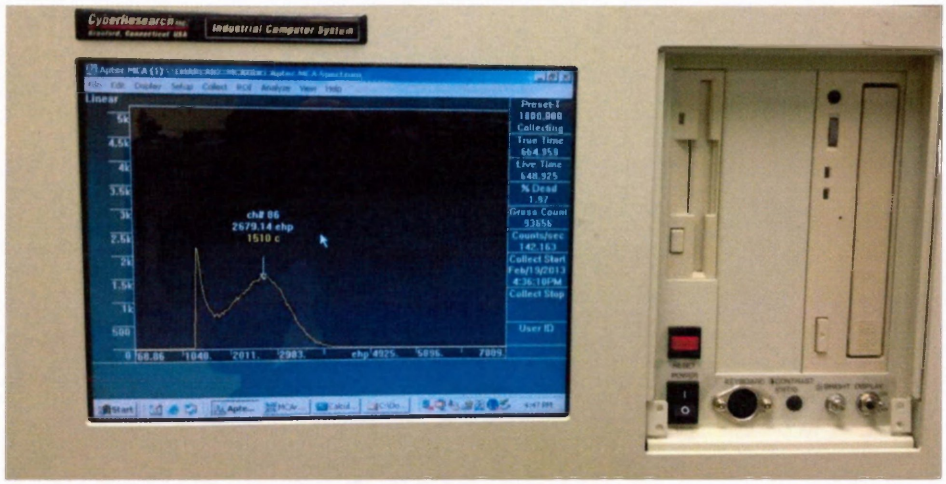

Figure 3.5 The computer is equipped with MCA card and software for analysis and data output. For each PHS experiment, the spectrum can be viewed in real-time which is shown here on the screen.

The multichannel analyzer collects pulses in all voltage ranges at once and displays this information in real-time. The number generated from the pulse in the ADC counter must somehow be stored for later use. The contents of the ADC counter (a number) is used as an address to identify a counter (or channel) of the MCA. When the ADC recieves an analog voltage pulse, the contents of this channel is increased by one. A MCA used for gamma spectroscopy can contain 1024 (1K), 2048 (2K), 4096 (4K), or more channels for storage. We only require 1024 channels for our small energy range. Each channel has the capacity to store at least 106 pulses. The contents of the different channels (i.e. number of counts) as function of the channel number (i.e. address), is referred to as the pulse height spectrum; both for analog and digital representation. A low-level energy discriminator (LLD) can be set to establish an energy threshold in the MCA. This is useful for rejecting electronic noise at the low energy range in PHS. The analog-to-digital conversion module (ADC) forms the heart of the gamma spectrometer. It converts the analog information from the pulse train into a digital format that can be stored and processed by a computer. As in Fig. 3.6, for each analog pulse received by the ADC, a number is generated that is proportional to the height of that pulse [9].

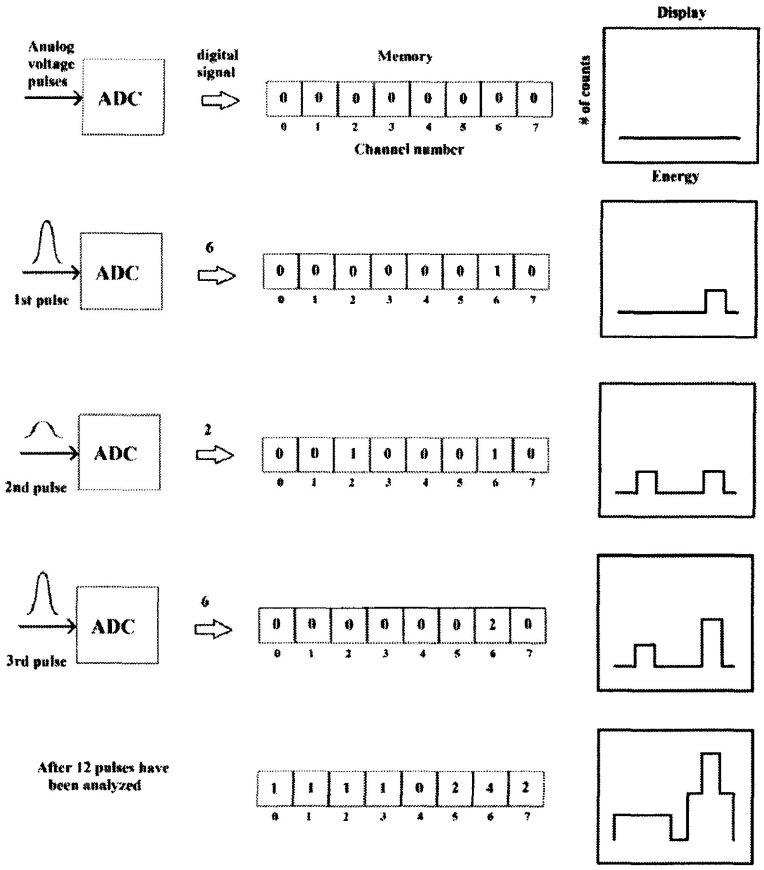

Figure 3.6 The ADC conversion process for signal pulse to memory storage. Each analog pulse received is assigned a channel in memory (one count) and over time, accumulated counts are diplayed as a histogram. This histogram is essentially the pulse-height energy spectrum in digital format.

3.2.2. Gamma-ray source

For experimental purposes, ^{103}Pd is non-conventional due to its relatively short half-life and availability. Alternatively, we use ^{241}Am, the gamma source of choice for many PHS experiments with a long half-life of 432 years. It decays by α-particle emission with by-product of monoenergetic γ-rays of energy ~60 keV. The ^{241}Am in these experiments have an activity of ~5 mCi. Figure 3.7 shows the placement of ^{241}Am on top of the shielding box, which delivers γ-rays from a distance of 5 cm to a-Se photoconductor.

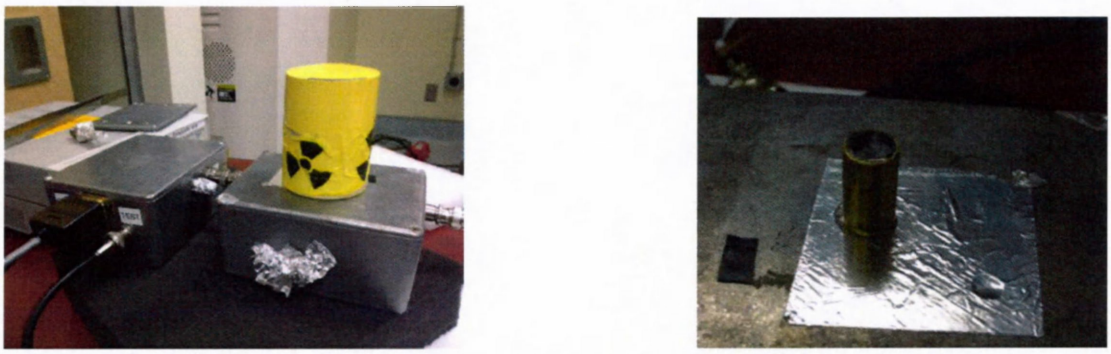

Figure 3.7 The ^{241}Am source, shielded by lead casing (left) and exposed (right), emits γ-rays of 60 keV to the sample for detection. The distance from the source to the detector inside is approximately 5 cm.

3.2.3. High-voltage power supply

Bias voltage from the high-voltage power supply in Fig. 3.8, is required to establish strong electric field in the a-Se sample that sweeps charge carriers across the thickness to be collected at adjacent electrodes. Without any field, all the charge generated will quickly recombine due to the Coulomb interaction of two unlike charges. As $W_{\pm}$ in a-Se depends strongly on electric field, high fields of 10 V/μm or greater are required to collect the photogenerated charge. Of course, with stronger applied fields there is a much higher charge collection efficiency as EHP recombination is suppressed. However, biasing the a-Se photoconductor with very high fields (>10 V/μm) can lead to dielectric breakdown. However, charge carrier injection from the bias electrodes introduces noise into the a-Se layer. At fields higher than 30 V/μm, there are unacceptable levels of noise in this particular a-Se structure and therefore, 30 V/μm is the experimental limit for this a-Se sample.

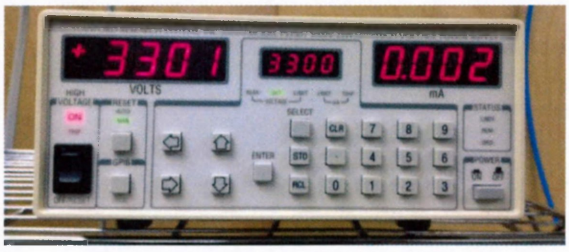

Figure 3.8 The power supply set at 3300 V to achieve a desired electric field of 30V/μm.

3.2.4. Preamplifier and amplifier

The charge created within the detector after the photon interaction with the detector crystal, is collected by the preamplifier. Additionally, the preamplifier also serves to provide a match between the high impedance of the detector and the low impedance of coaxial cables to the amplifier, which may be located at great distances from the preamplifier. Most PHAs in use today are equipped with resistor-capacitor (RC) feedback preamplifiers [7]. These can have various modes of operation: current-sensitive, voltage-sensitive and charge-sensitive [9]. Charge-sensitive preamplifiers are commonly used for most solid state detectors where an output voltage pulse is produced that is proportional to the input charge. To maximize performance, the preamplifier should be located at the detector, as illustrated in the left photo of Fig. 3.9 below.

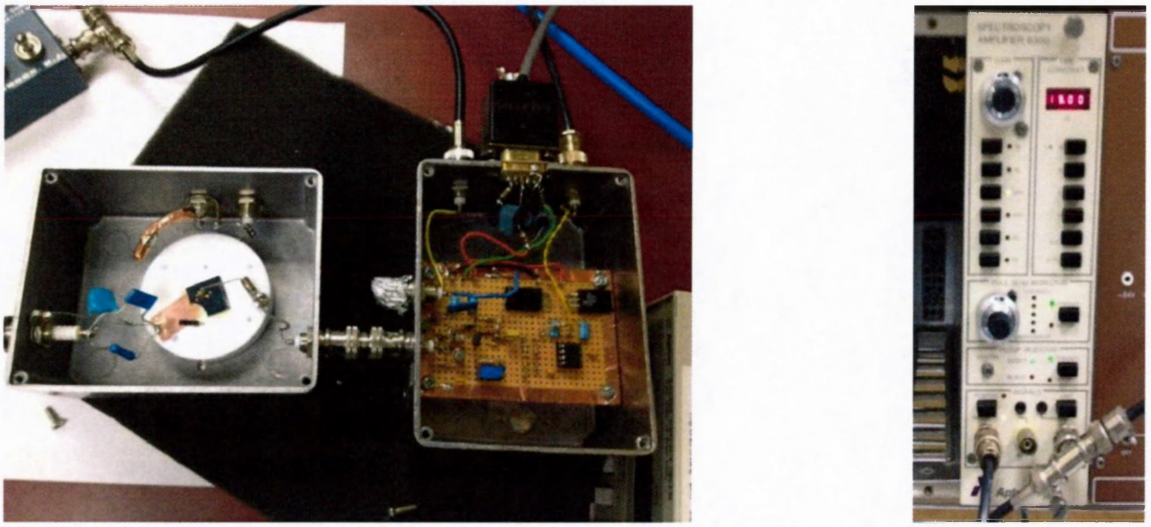

Figure 3.9 The preamplifier (left) is connected in proximity to the detector. The amplifier (right), with 19 μs shaping time and gain of 300, increases and shapes the small EHP signal to measureable amplitudes.

The charge collected is integrated over our collection time to output the overall signal. If this wasn't the case, we would receive no signal at all since the charge of each individual interaction would be well below the threshold of our electronics. The amplifier used in these PHS experiments is *Aptec Spectroscopy Amplifier 6300*, shown in the right photo of Fig. 3.9.

The amplifier provides two main functions: a) to increase the still relatively small pulses from the preamplifier (millivolts) to sufficient amplitude (volts) in order to provide measureable signal to the MCA; and b) to reshape the slow decaying pulse from the preamplifier into a narrow one to avoid the problem of pulse pile-up at high counting rates and to improve SNR. The gain has an adjustable range from x1 to x1000. By several trials, a gain of x300 was an appropriate medium to acquire a measureable signal pulse above the electronic noise. Pulse shaping is an essential function of the amplifier as well. For example, consider the output of the preamplifier as a sharply rising pulse that decays with a time constant, τ of about 50 μs, returning to the baseline after about 500 μs. Thus if a second pulse occurs within that 500 μs, it will "ride" on the tail of the previous pulse, as in Fig. 3.10, providing the MCA with incorrect amplitude information. Shaping time (or integration time) must be carefully adjusted to provide output of clearly separated pulses, even though the output from the preamplifier are overlapping pulses. The most common shaping methods are RC, Gaussian, and delay-line methods [9]. The chosen shaping time of *19 μs* was also done by trial. Longer shaping time is required for trapped charges to be released and later collected. However, increasing the shaping time creates more pulse pile-up.

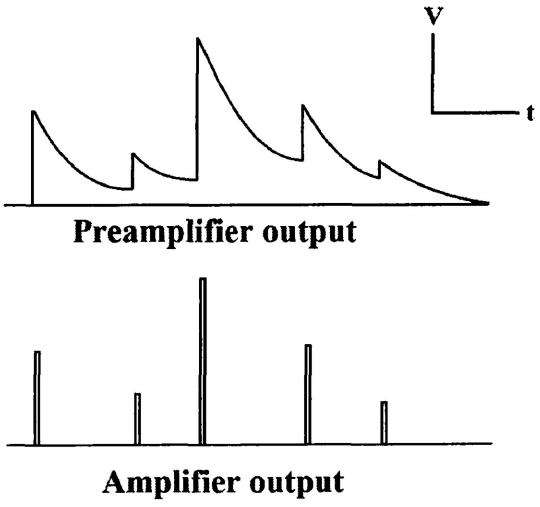

Figure 3.10 The overlap of pulses from preamplifier (above) causes "pile-up" shown as the tails of each pulse for which the amplifier (below) must eliminate with shaping. The vertical scale is in volts and the horizontal is time.

3.2.5. Calibration and pulser

Calibration involves converting the channel number into an energy scale, or number of EHPs. The reason for choosing a scale in EHP will be apparent in the discussion section when photoconversion processes are examined. Calibration can be performed using a test pulse (or pulser), shown in Fig. 3.11, driven into the PHA from a function generator. Another reason to use a pulser is to calibrate our final PHS signal to the electronic noise of the components. Since the function generator should trigger the oscilloscope with an exact voltage each time, the Gaussian spread of the pulser can be attributed to the noise in the PHA electronics. We choose a pulser signal larger than the signal from ^{241}Am so that the two can be clearly distinguished.

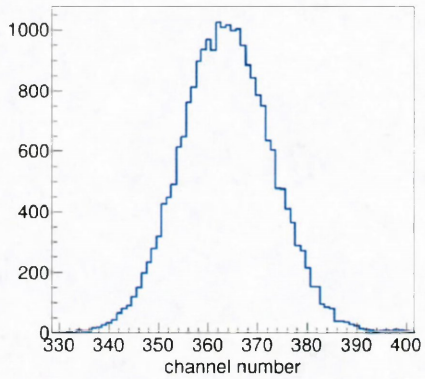

Figure 3.11 A pulser with peak of around 1000 counts, from a square-wave input used to calibrate channel number to number of EHPs and for testing noise level in the electronics.

From the oscilloscope, the pulser is input as a square wave with peak-to-peak voltage, $v_{pp} = 720\ \mu V$. Then we collect the counts from that pulse with the MCA and see the peak lies at around channel 202 (Fig. 3.12). By measuring the capacitance of the detector capacitor, $c = 1.38\ pF$, the total collected charge from the pulser, q, is calculated by:

$$q = c * v_{pp} \tag{3.2}$$

$$q = (1.38x10^{-12}\ F) * (720x10^{-6}\ V) = 9.936x10^{-16}\ C$$

$$\frac{9.936x10^{-16}\ C}{1.602x10^{-19}\ C/EHP} = 6202\ EHP$$

Therefore, Ch 202 = 6202 EHP for the channel to EHP calibration. If we change the pulser amplitude and repeat this process, we now have a linear scale of channel number relative to collected charge.

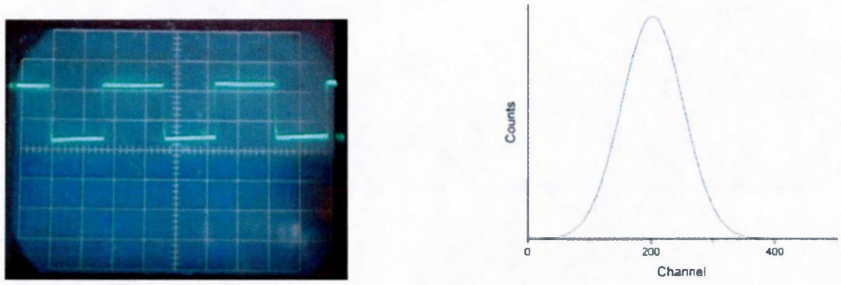

Figure 3.12 Square-wave pulser (left) and the pulse-height spectrum for that wave from the MCA (right).

3.2.6. The a-Se photoconductor layer

We place the 110 μm thick a-Se sample inside a shielding box to reduce exposure to external radiation sources, especially ambient light. The photoconductor is extremely sensitive such that any external sources of energy such as light or sound (vibrations) will vary the electrical signal enough to record inaccurate pulse amplitudes in the PHA which essentially distorts the γ-ray pulse into a noisy signal. The a-Se structure used in these PHS experiments is outlined in Fig. 3.13. The a-Se layer is deposited upon an indium tin oxide (ITO) glass substrate, serving as the bottom electrode. The HV power supply is connected to the copper contact underneath the ITO, electrically linked to the glass via conductive tape. The wiring pases through a simple RC filter circuit to reduce high frequency noise generated by the power supply, thus limiting external noise from this source. Gold contracts were sputtered on top of the a-Se layer which serve as the top electrode for biasing. There is also a resistive interface layer (RIL) between the a-Se and gold contacts to supress dielectric breakdown of the sample. This layer allows us to use strong electric fields needed to improve $W_{\pm}$ without increasing dark current or damaging the sample at the edges of metal contacts where electric field is further increased. A small contact pin touches the contact which is passed to the preamplifier, thus completing the circuit. The detector box setup with the a-Se sample enclosed is diplayed in Fig. 3.13. When measurements are performed, the lid seals this box shut and the lights turned off to minimize background radiation.

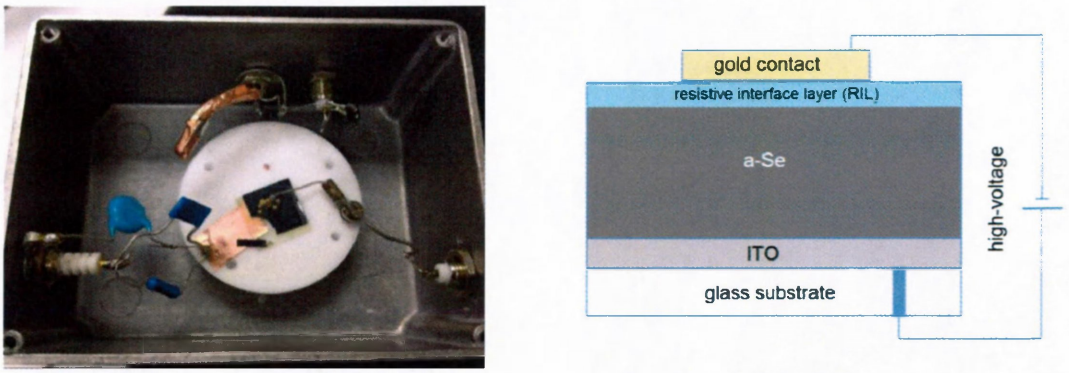

Figure 3.13 The left photo shows the a-Se sample with connected electronics, enclosed in aluminum shielding box to reduce the effects of background noise and ambient light. The input from the power supply passes through an RC filter to reduce high-frequency noise. The schematic on the right shows the a-Se structure with gold and ITO serving as the top and bottom electrods, and with a RIL to suppress dielectric breakdown at the electrode interface.

3.3. Experimental results

For this PHS experiment, we use an EHP scale instead of energy in order to measure total charge collected when calculating the photoconversion gain ($W_{\pm}$). This depends on both the electric field across the a-Se sample and on the temperature to which it is exposed. These two variables will be the dependence on which we will base our measurments on. In the MCA, we set the LLD to reject electronics noise less than 1000 EHP. EHPs less than this threshold obscure the signal pulse which convolutes with the electronic noise. PHS is performed with electric field dependence in Figs. 3.14 to 3.15 and temperature dependence in Figs. 3.15 to 3.16. To calculate $W_{\pm}$, the peaks of the pulse-height spectra are analyzed by Gaussian-fitting (Figs. 3.15 and 3.18). This is necessary to interpret the peaks of each PHS signal in order to acquire $\langle n_0 \rangle$, the mean EHPs for the Gaussian-fitted results. The importance of $\langle n_0 \rangle$ becomes aparent in Equation 3.3.

3.3.1. Electric field dependence

The first set of measurements were each performed for 30 min. collection time and the data presented in Fig. 3.14 is the pulse-height spectra from 10 to 30 V/μm in 5 V/μm increments, where N is the number of photon counts and n_0 is the number of collected EHPs of those counts.

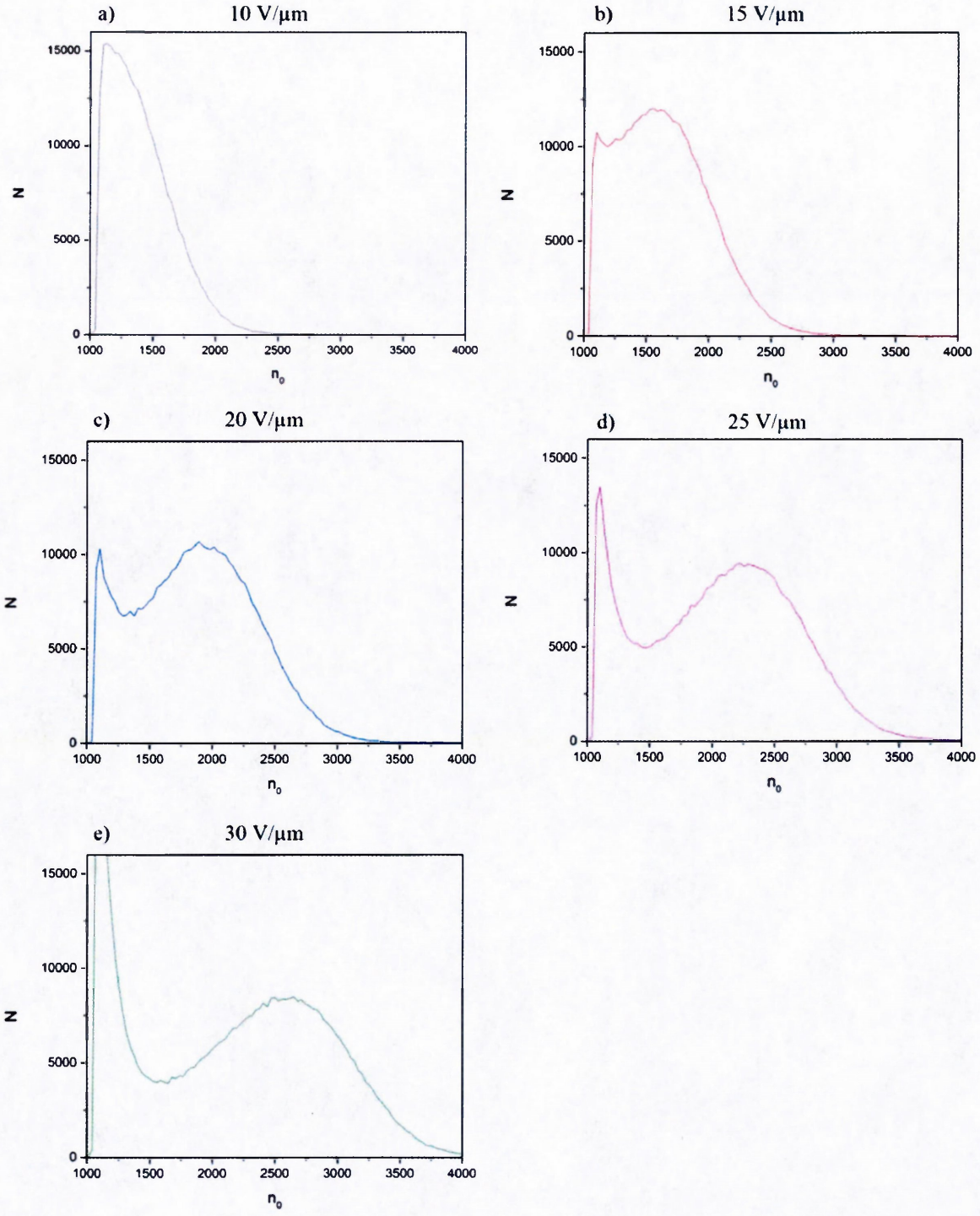

Figure 3.14 PHS signals with electric field dependence at 20 °C for a) 10 V/μm, through e) 30 V/μm, where N is the number of photon counts and n_0 is the number of collected EHPs. The two peaks represent background noise, at the lower EHP region and signal from ^{241}Am (the Gaussian) to the right of this.

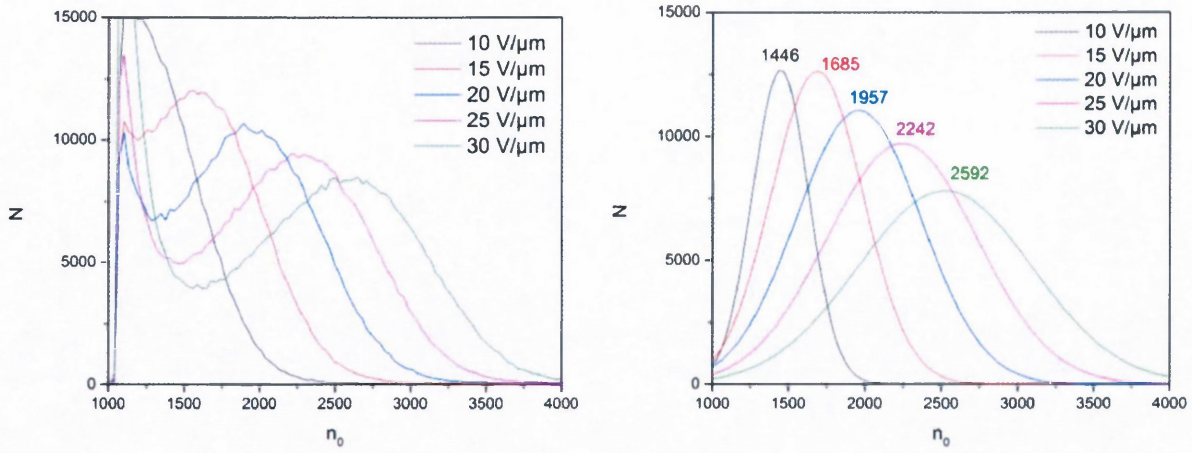

Figure 3.15 Combined PHS signals for all electric fields at 20 °C (left) and the Gaussian-fitted signals (right) with $\langle n_0 \rangle$ indicated for each peak. N is the number of photon counts and n_0 is the number of collected EHPs.

3.3.2. Temperature dependence

The temperature dependence of PHS was investigated to examine the peculiarities of charge collection in a-Se subjected to a temperature range from -20 °C to 30 °C. Figure 3.16 displays the new experimental apparatus, where the previous shielding box is replaced with a temperature controlled stage (Linkam®) for heating, and cooling with liquid nitrogen. Due to the vibration-induced noise from the liquid nitrogen pumping, PHS measurements were taken cumulatively for 60 s duration, at 10 s intervals. Pumping was shut off while the MCA recorded ^{241}Am signal pulses. The PHS results are presented in Fig. 3.17 with a selected electric field of 20 V/μm.

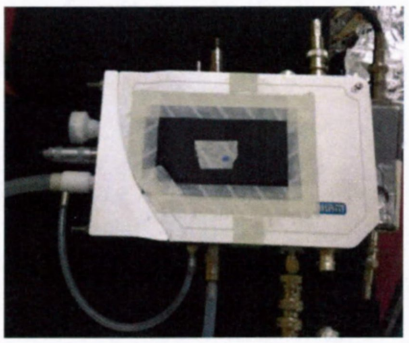

Figure 3.16 Linkam® temperature-contolled stage apparatus replaces the detector box in the previous setup. The a-Se is enclosed inside with electronics outside to prevent damage from extreme temperatures. The stage is supplied with liquid nitrogen which is controlled with a digital controller for cooling and heating cycles.

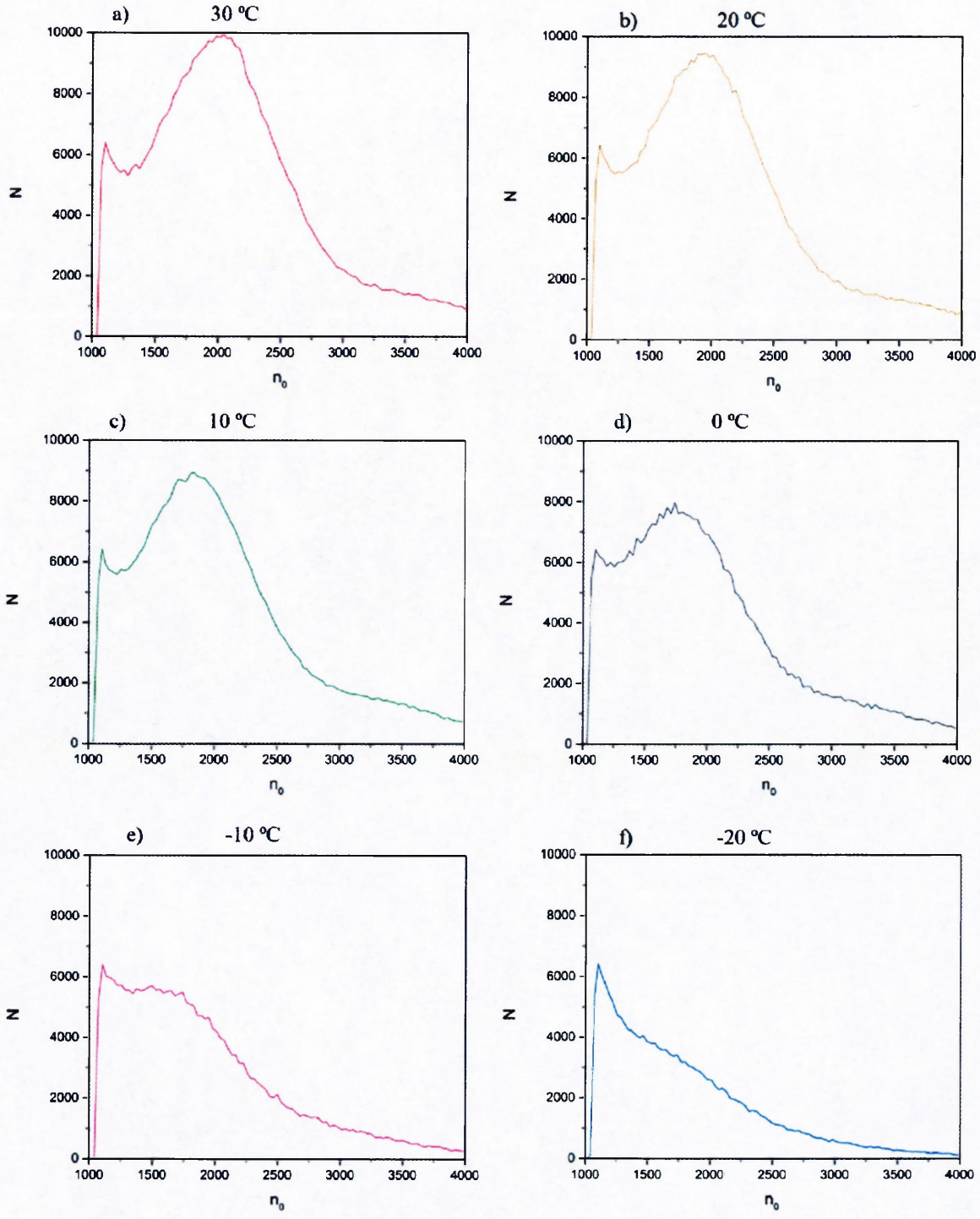

Figure 3.17 PHS signals with temperature dependence at 20 V/μm for a) 30 °C, through f) -20 °C, where N is the number of photon counts and n_0 is the number of collected EHPs.

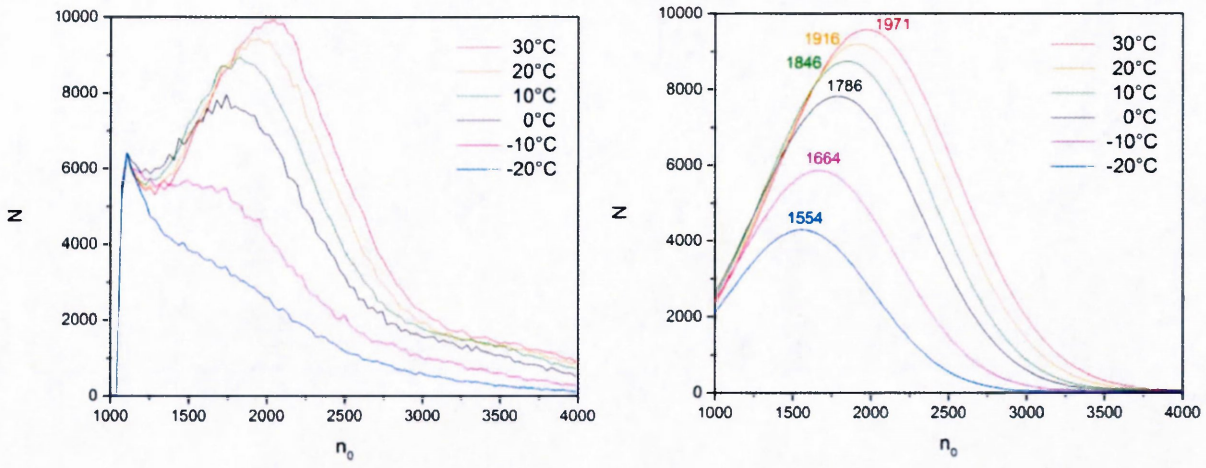

Figure 3.18 Combined PHS signals at 20 V/μm for all temperatures (left) and Gaussian-fitted signals (right) with $\langle n_0 \rangle$ indicated for each peak. N is the number of photon counts and n_0 is the number of collected EHPs.

3.3.3. Photoconversion gain

PHS is the most direct approach in measuring the photoionization energy, $W_{\pm}$, which is presented with both electric field and temperature dependencies. This is experimentally determined by dividing the photon energy, E_γ, by the average number of EHPs, $\langle n_0 \rangle$, at the photopeaks of each pulse-height spectrum [62]:

$$W_{\pm} = \frac{E_\gamma}{\langle n_0 \rangle} \tag{3.3}$$

$W_{\pm}$ has been measured in the range from 10 V/μm to 30 V/μm, shown in Fig. 3.19. The temperature dependence of $W_{\pm}$ at selected 20 V/μm from -20 °C to 30 °C is shown in Fig. 3.20. There is a certain degree of inaccuracy in Gaussian-fitting which is expressed as the variance. In Figs. 3.19 to 3.20, this is illustrated as error bars. A larger variance from Gaussian-fitted parameters results in greater error for $\langle n_0 \rangle$.

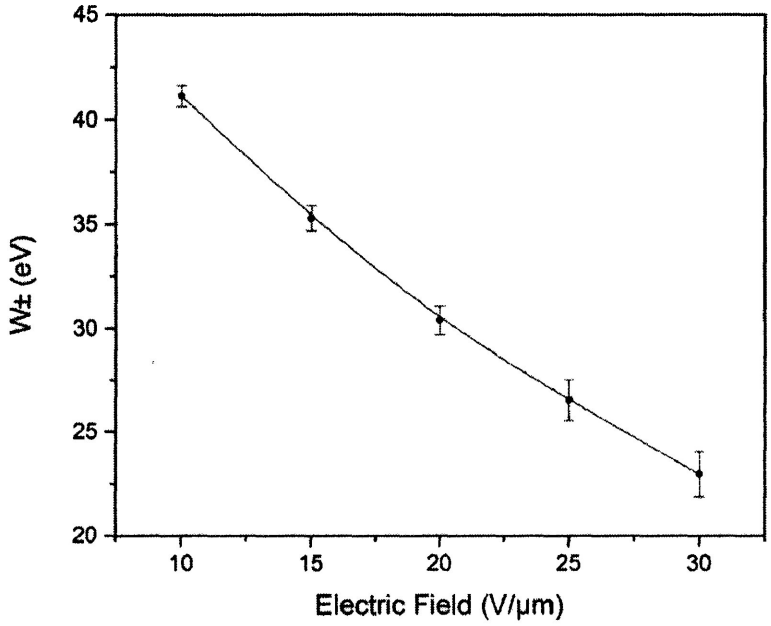

Figure 3.19 $W_{\pm}$ as a function of electric fields from 10 V/μm to 30 V/μm at 20°C. Error bars are associated with variance of the Gaussian-fitted peaks.

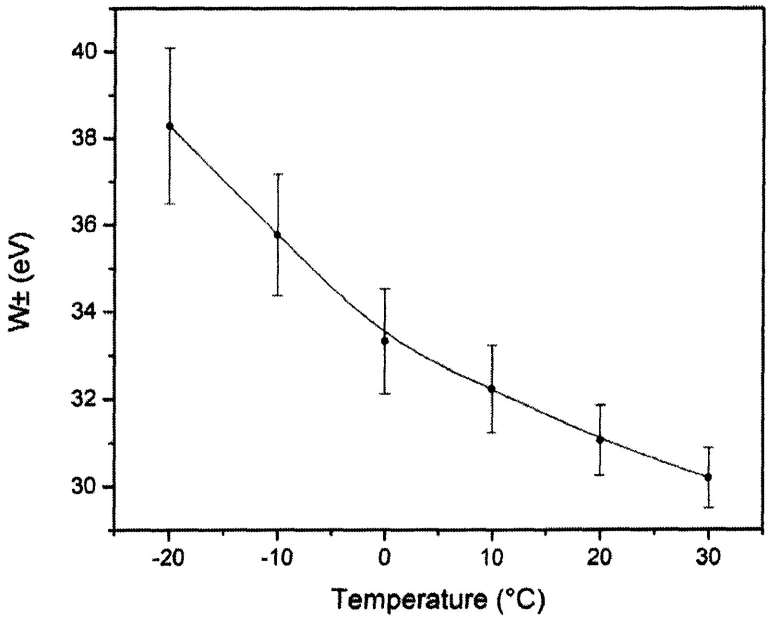

Figure 3.20 $W_{\pm}$ as a function of temperatures from -20 °C to 30 °C at selected electric field of 20 V/μm. Error bars are associated with variance of the Gaussian-fitted peaks.

3.4. Discussion

By examining Figs. 3.14 to 3.17, the total pulse-height spectra are composed of two peaks: signal from ^{241}Am (the photopeak) and signal from background noise. From Fig. 3.15 a) to e), we clearly see that by increasing the electric field, the photopeaks shift toward a greater number of EHPs, n_0. Similarily in Fig. 3.16 a) to f), the increase in temperature at a constant 20 V/μm shows an increase in charge collection. The photopeaks are fit to a Gaussian which gives numerical data for the mean, $\langle n_0 \rangle$ and width, σ_0 of each photopeak. In Fig. 3.14 a), the photopeak is difficult to distinguish from the noise level, suggesting 10 V/μm is too low for photon counting. At 15 V/μm and greater, the peaks are far more separate than the noise level and so peak fitting is accomplished with greater accuracy. Ideally, individual γ-rays, all of the same energy, would each produce a voltage pulse of the same value. Such would be the case as illustrated in Fig. 3.21 a). However, as mentioned at the beginning of this chapter, energy variations from scattering and other stochastic interactions will result in n_0 fluctuations. As a result, there are differences in the amplitude of the signal from ^{241}Am for events in which precisely the same amount of radiation energy is deposited in the photoconductor. Instead of a narrow photopeak in Fig. 3.21, the actual photopeak is a Gaussian-shaped curve, as in Fig. 3.21 b). The width of the photopeak can be related to the energy resolution of the detector.

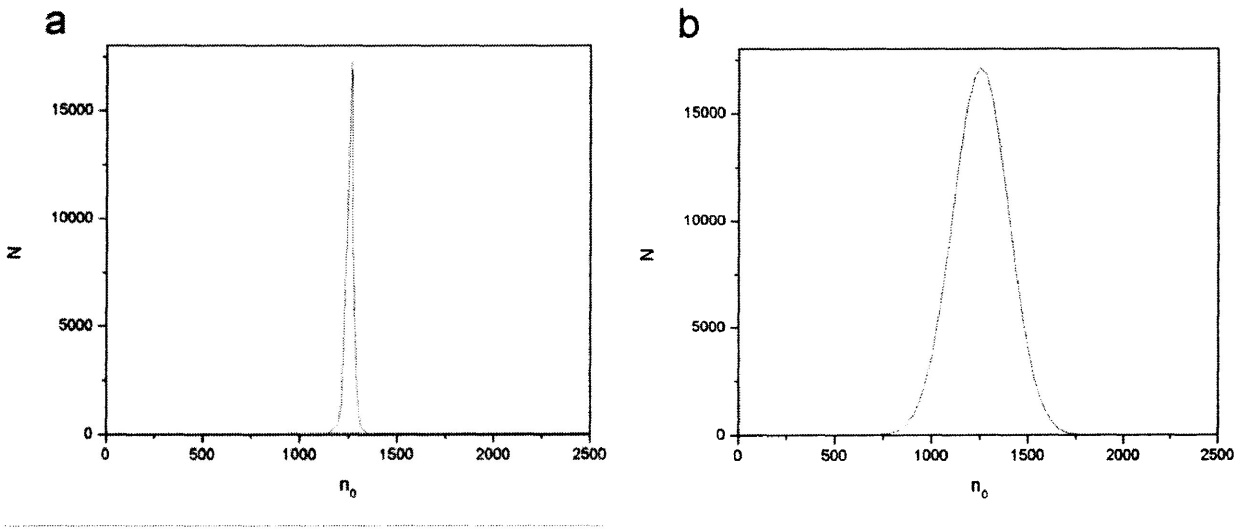

Figure 3.21 The ideal spectrum of measured γ-ray energies due to the photoelectric effect (a) versus the actual distribution (b) due to variations in energy deposition and counting rates.

The peculiarities of charge mechanisms in a-Se directly influence the n_0 parameter in all PHS measurements. The importance of $\langle n_0 \rangle$ is demonstrated from Equation 3.2 to calculate the photoionization energy of a-Se at various fields and temperatures. $W_{\pm}$ is a characteristic of the EHP creation energy for a photoconductor. This is the ratio between the radiation energy absorbed and the average number of EHPs created. We can see as electric field increases, the $W_{\pm}$ decreases. From Fig 3.19, at 10 V/μm, it takes about 41 eV to generate an EHP where at 30 V/μm, it takes roughly half of that. The main point is that as electric field increases, number of EHPs collected increases as well, resulting in a lower $W_{\pm}$. To investigate this, three mechanisms which govern n_0 and thus, $W_{\pm}$, in a-Se are considered. These are EHP generation, recombination and trapping [63], shown schematically in Fig. 3.22 below.

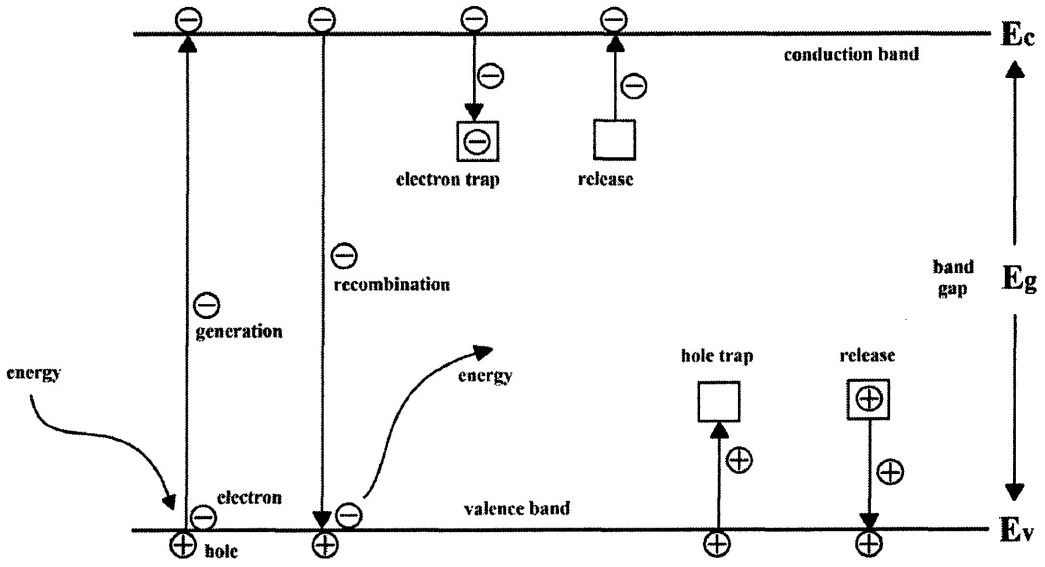

Figure 3.22 The illustrated processes of generation, recombination, trapping (and release) of electons and holes in the band gap of a-Se.

The results acquired here are compared to one which were modeled with a MC simulating the transport of EHPs within an electric field to calculate the dissociation effeciency of EHPs. Our experimental results for $W_{\pm}$ are within 7% agreement with those simulated [64]. Investigation into the photogeneration processes has sought to describe the experimental intrinsic value for a-Se ($W_{\pm}{}^{0}$), which is described by the Klein rule [65]:

$$W_{\pm}{}^{0} \approx \frac{14}{5} E_g + < E_{ph} > \tag{3.4}$$

where E_g is the band gap of a-Se and $< E_{ph} >$ is the energy of phonon generation. In theory, $W_{\pm}{}^{0}$ is approximately 6 eV, for a band gap of 2.2 eV [66]. This is only the case where all the charges generated from ionization are collected. As in Fig. 3.19, the $W_{\pm}$ ranges from about 23 to 41 eV, which is up to ten times that of the intrinsic range. The field dependence of $W_{\pm}$ in a-Se is mainly due to the initial recombination of EHPs, which is termed as dissociation efficiency [62]. This recombination occurs mainly between electrons and holes in excitonic stage as opposed to band-to-band recombination. Models have shown that at low electric fields, only about 10% of generated EHPs survive recombination [65]. This explains why we see at 10 V/μm, $W_{\pm}$ is almost 10x larger than expected (41 eV). At the highest field used in Fig. 3.14 e), we see that $W_{\pm}$ is much lower in Fig. 3.19 and so recombination is suppressed by the EHPs higher drift velocities associated with increased electric potential across the a-Se layer.

Fluctuations in the number of charge carriers generated as a result of absorption of a high energy radiation can be expressed through the Fano factor:

$$F = \frac{\sigma^2}{\langle n_0 \rangle} \tag{3.5}$$

where $\langle n_0 \rangle$ is the mean number of EHPs generated and σ^2 is the variance in the number generated [65]. According to theoretical predictions, the intrinsic value of the Fano factor in selenium is confined within the range of 0.03–0.06, which is superior to the corresponding characteristic in Si, Ge. However, achieving these values practically can be challenging due to the recombination of photogenerated charge carriers, which is present to a large extent in selenium, even at strong electric fields up to 60 V/μm [62,65]. In our case, the Fano factor is greater than 1 since there is a moderate amount of electronics noise in the system as well.

To evaluate the performance of a detector, we can measure its energy resolution. Essentially, this is a measure of detector ablility to differentiate between photons of different energies. For obvious reasons, this characteristic is especially important when measuring a radionuclide of

more than one emission energy. The Fano factor is closely related to the intrinsic limit of the energy resolution, R_E, of the detector, which is the FWHM divided by $\langle n_0 \rangle$ [9]:

$$FWHM = 2.35482\,\sigma_i \tag{3.6}$$

$$R_E = \frac{FWHM}{\langle n_0 \rangle} = \frac{2.35482\,\sigma_i}{\langle n_0 \rangle} \tag{3.7}$$

Before we can acquire an accurate measurement for this however, the PHS signal from the detector needs to be separated from the PHA electronics. This can be accomplished from knowing two things: a) the total PHS signal with the intrinsic noise of the detector plus the noise of the electronics; and b) the electronics noise by itself. Each PHS signal is a convolution of many smaller signals from ^{241}Am, the electronic noise in the PHA and the intrinsic noise of the detector. The most accurate way to eliminate all sources of noise in the analysis would be a deconvolution of each noise signal. This, however, would be very difficult to perform and requires mathematical constructs of the noise in each signal. As the intrinsic noise and electronics noise are statistically uncorrelated, we can add them in quadrature to result in the total noise in the PHS signal:

$$\sigma_0 = \sqrt{\sigma_e{}^2 + \sigma_i{}^2} \tag{3.8}$$

where σ_e is the noise in electronics and σ_i is the noise in the a-Se [9]. The σ for the Gaussian peaks are the widths of the PHS signal. The electronics noise can be found from the σ of the pulser. Then by assuming the electronics noise to the far left of each PHS signal, does not intersect the photopeak signal, we can fit the intrinsic noise to a Gaussian and determine the σ and $\langle n_0 \rangle$. We choose the 30 V/μm measurement for fitting since this signal is most separate from the noise than the other fields. The following fit curve in Fig. 3.23 is assuming the noise counts and the peak counts do not coincide. In the total PHS signal, the noise is fit to a Poisson function and the pulser and photopeak to a Gaussian. We can then use the mean and sigma of the fitting to interpolate σ_i for a-Se to calculate the FWHM.

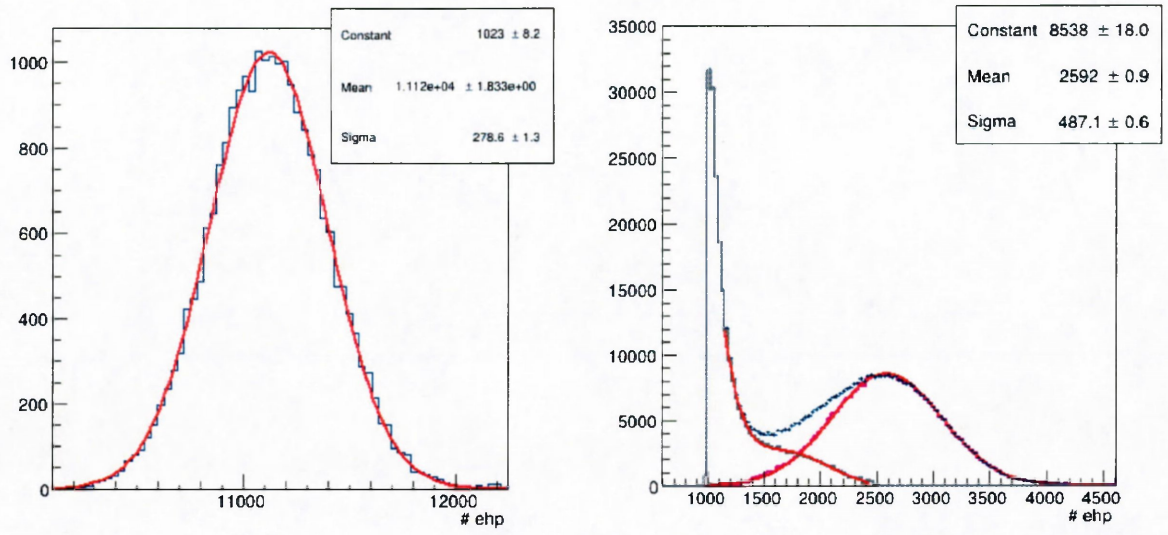

Figure 3.23 The electronics noise attributed to the pulser signal, shown on the left, and the noise in the total PHS signal is fitted in red, for the PHS measurement of 30 V/μm. Assuming the electronics noise does not cross the $\langle n_0 \rangle$ of the total signal, this can be fitted to give the width of the electronics signal, σ_e, and total signal, σ_0, to acquire the intrinsic noise, σ_i. The noise peak is fit to a Poisson function and the pulser and photopeak to a Gaussian.

$$\sigma_i = \sqrt{{\sigma_0}^2 - {\sigma_e}^2} = \sqrt{487.1^2 - 276.6^2} \cong 401\ EHPs \tag{3.9}$$

Then the energy resolution for our a-Se photoconductor, without noise is:

$$R_E = \frac{2.35482\ \sigma_i}{\langle n_0 \rangle} \cong \frac{944\ EHPs}{2592\ EHPs} \cong 0.364 \quad or \quad 36.4\% \tag{3.10}$$

In other PHS experiments (Blevis, Hunt and Rowlands) using ^{241}Am and a 150 μm thick layer of a-Se [67] similar results are obtained for $\langle n_0 \rangle = 3075$ EHP and $\sigma_i = 445$ EHP, with an energy resolution of 34%. The difference from the results presented here are within experimental uncertainties. Since the sample thickness of 150 μm was greater, this can explain the higher charge collection and better energy resolution than those presented here.

This energy resolution is rather poor for a gamma camera as NaI cameras typically have a resolution of ~15% and CdZnTe at ~9% for 60 keV energy [68,69]. However, due to the

relatively low energy of seeds, high energy resolution does not offer any advantages in PBSI imaging. Compton scattering is expected to be much less than if we were using a greater energy since Equation 1.8 shows higher energy photons will scatter more. Since our calculated resolution is only about 17% greater than the required energy window of the discriminator, only a few of these scattering events near the Compton edge will be resolved. These corrspond to mainly backscattered γ-rays which retain most of their energy from incidence to undergo absorption later. Multiple Compton and lower energy scattering events will most likely lie outside of the energy resolution of the detector. For a minumum $W_{\pm}$ of ~22 eV at 30 V/μm this corresponds to ~2700 EHP. Thus, scattered events are expected to appear in the Gaussian part of the PHS signals. In each case, there is no clear indication that the signal is significantly altered by Compton scattering. This is especially true in the PHS setup where the only mediums for ^{241}Am photons to scatter would be in the light Z, aluminum shielding box, and the a-Se detector. From simulation, it was shown at 60 keV, scattering in the a-Se was still less than 1%, as in the 21 keV case. Thus, any scattering events would be negligibly small that they are undetected. Any scattering events would likely be within the LLD threshold, as seen by the increase in noise level with increasing electric fields. Photoelectrons emitted near the edges in the detector can also lose a portion or all of their energy to the walls of the enclosure thus producing a lesser voltage pulse in the detector. Most probably, the scattered events are negligibly small compared to our photopeak which already shows a broad distribution about its central peak so Compton scattering events are obscured from the Gaussian broadening of the photopeaks and within the noise levels in Figs. 3.14 and 3.17.

To correlate these PHS experiments with GATE, we simulate ^{241}Am, using the 0.364 energy resolution calculated at 30 V/μm shown in Fig. 3.24. The source is monoenergetic 60 keV, the sheilding box is set to aluminum and the collimator and phantom geometries are removed from the previous GATE simulation. The majority of Compton scattering counts are apparent less than the 1000 EHP mark, suggesting that in the experimental results, these would not be seen at all due to the LLD rejecting the majority of electronic noise. The Compton edge is likely smeared within the energy blurring of the photopeak. Recall from the digitizer section of GATE that energy blurring will smear the photopeak into a Gaussian of width defined by the energy resolution for the detector. The photopeak width of $\sigma_i = 468\ EHPs$ is calculated, which agrees within 1.2% of the actual PHS results from Fig. 3.23.

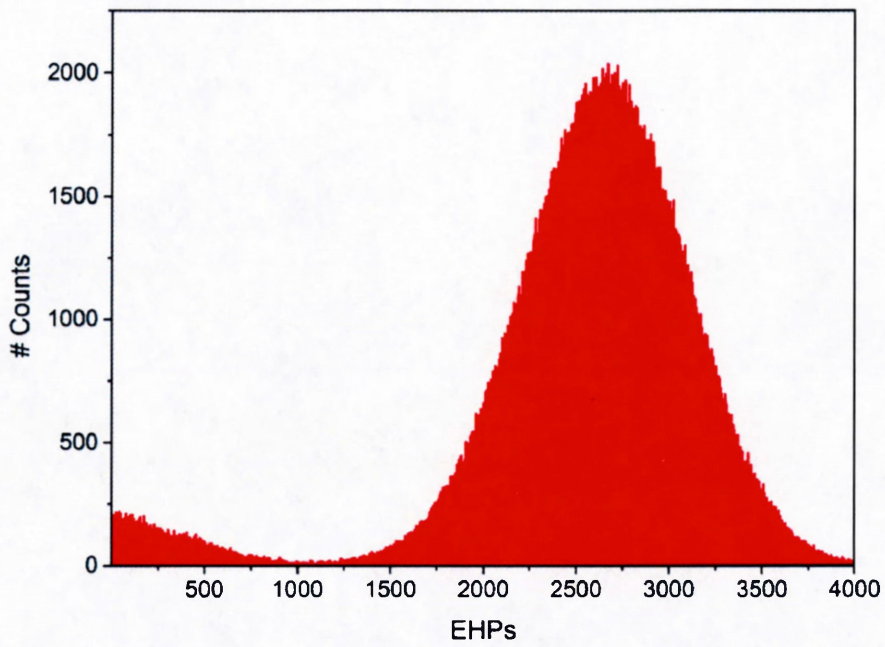

Figure 3.24 The PHS data for ^{241}Am at 30 V/μm, simulated for 10 s with GATE. Compton scattering is largely confined to counts below 1000 EHPs, the noise threshold of the electronics in the PHA. This suggests that scattering in the PHS experiments remains undetected.

To factor energy resolution into the a-Se gamma camera, energy blurring of 0.364, about a mean energy of 20.5 keV is simulated in GATE. This data, both in energy and position, represents the output for an a-Se gamma camera with energy resolution of 36.4%. The final simulation results presented in Fig. 3.25 include the energy and position data for a 60-seed distribution imaged with the proposed a-Se based gamma camera for PBSI.

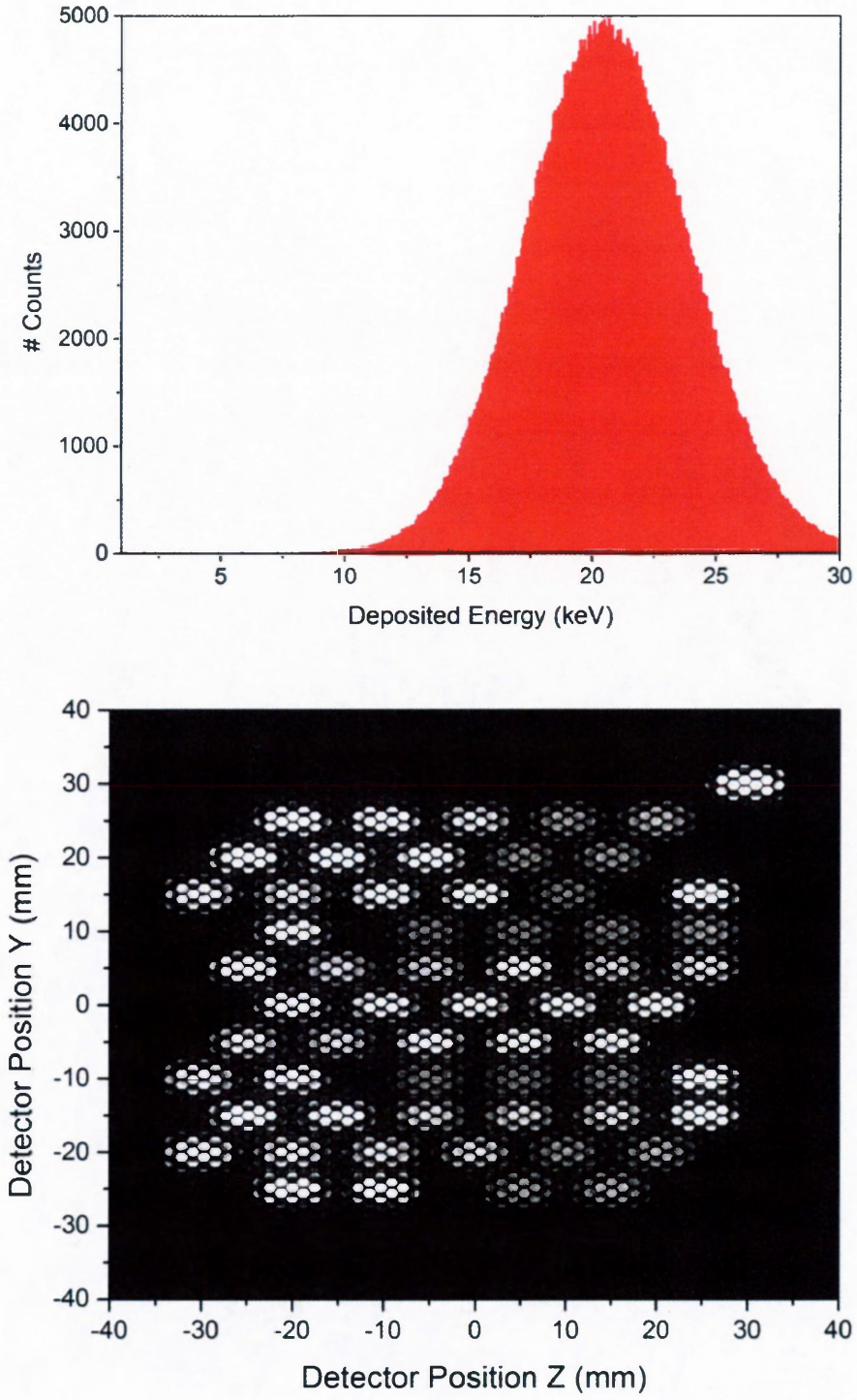

Figure 3.25 The energy and position data for an a-Se gamma camera with 36.4% energy resolution simulated with energy blurring in GATE. Energy data is a Gaussian photopeak with no visible Compton scattering and position data illustrates how the intensity of images depends on their distance to the camera. Brighter images correspond to the ones in the superficial layer (closer to breast surface) while darker images correspond to ones in the deeper layers.

As discussed previously, there is a high electric field required throughout the thickness of the sample to allow charge carriers to drift and be collected. Trapping in the amorphous structure results in losses if we do not wait long enough to collect that charge relating to the shaping time of the amplifier. Higher electric fields should decrease trapping but as mentioned previously in the detector section, biasing the a-Se can introduce extra noise into the photoconductor.

Among the other processes mentioned, another cause of noisy PHS signal can be attributed to the amount of dark current in the a-Se layer. Dark current introduces shot noise and effectively lowers the dynamic range of a photoconductor. High dark current decreases the sensitivity of the detector as it provides unwanted noise that is added to the signal, in turn lowering the SNR. It also restricts the dynamic range by accumulating unwanted charge on the pixel capacitor, and the trapped charges give a spatial charge effect which alters the internal electric field, spreads the photogenerated charges in the bulk and adds noise to the signal [24]. There are two origins of dark current in a-Se photoconductors. The first results from thermally generated carriers in the bulk of the material [20]. The second is due to carrier injection from the metal contacts into the a-Se layers. Since a-Se has a wide band gap, $E_g = 2.2\ eV$, thermal generation is negligible compared to injection at room temperature [24]. The injected carriers would introduce the most significant dark current and thus injection must be prevented. The problem with injection lies in the fact that in order to maximize charge collection of a-Se, high operating fields are required, but injection significantly increases with the nominal applied field. In order to keep dark current low in the a-Se layer, injection must be blocked at the electrode/a-Se interface.

The PHS signals from temperature dependence (Fig. 3.17) shows an increase in charge collection with temperature. Since the field is constant, and the number of EHP collected changes with temperature, there are mechanisms which suppress charge transport. The mechanisms responsible are trapping and recombination, as shown in Fig. 3.22. Then the total number of charge carriers we collect n_0 is the difference of n_c, the number of charge carriers created, n_r, the number which recombine and n_t, the number which are lost to traps without being released:

$$n_0 = n_c - n_r - n_t \tag{3.11}$$

To model the thermal release from those carriers of trap states, an Arrhenius dependence is proposed:

$$n_t \ \alpha \ \exp\left[\frac{-E_a}{k_B T}\right] \tag{3.12}$$

where E_a is the activation energy to release charge carrier from trap state, k_B is the Boltzmann constant and T is the temperature [9]. Then, using n_0 at 30 °C for reference, we can calculate the difference in charge collection with each increase in temperature, Δn_0, and plot the natural log of this with inverse temperature to calculate the activation energy, plotted in Fig. 3.26. By this analysis, we correlate the linear decrease in temperature with the variation in charge collection resulting from the lower thermal excitations of trapped charge. This is under the assumption that EHP generation and recombination processes are independent of temperature. Two major factors which govern EHP generation and recombination are a) the photon energy, and b) the electric field strength. The effects of temperature on charge carrier diffusion and the band gap are assumed to be negligible.

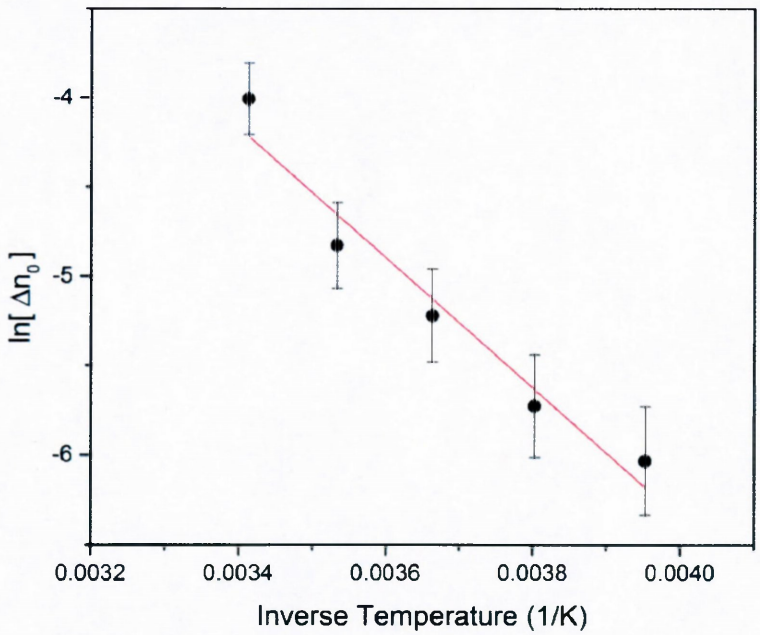

Figure 3.25 The collected charge differences from 30 °C, Δn_0 plotted with inverse temperature. The slope of the Arrhenius dependence is proportional to the activation energy required for trapped carriers, n_t to be thermally released. Error bars are associated to the variance of the Gaussian-fitted peaks in the temperature PHS results.

In Fig. 3.25, the slope results in an activation energy of ~0.3 eV. As interpolated from the density of states (DOS) diagram for a-Se in Fig. 3.26, this energy lies in the shallow electron trap state, previously published by Rowlands and Kasap in *Physics Today* [70]. This demonstrates how release from trap states in a-Se is related to the shallow trap level 0.3 eV from the conduction band level of 2.2 eV. With lower temperatures, charge is trapped for longer durations which results in fewer charge collected, n_0. Since electrons are the slower mobility charge carriers in a-Se, these charges have higher trapping probability than faster-moving holes.

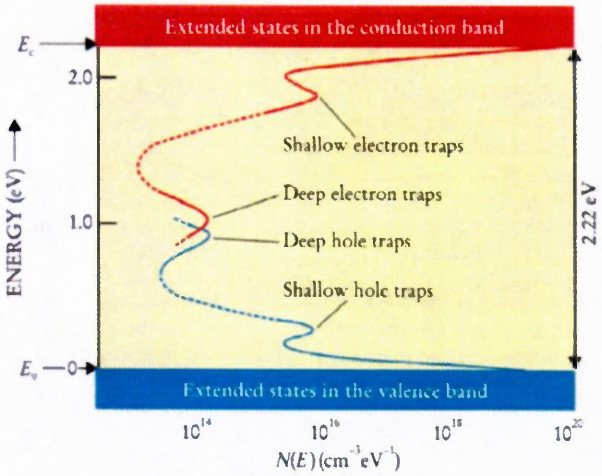

Figure 3.26 The DOS diagram for a-Se, showing localized trap states within the band gap [70].

3.5. Conclusions

The PHS experiments and GATE simulation of ^{241}Am presented in this chapter demonstrates that Compton scattering is too low to be detected by the PHA electronics. Furthermore, the Compton signals are small enough compared to photopeak counts such that energy discrimination, to distinguish between photoelectric and Compton events, is not a requirement for the PHA to achieve a localized signal. a-Se photoconductor is sensitive enough to achieve a count rate of ~160 cpm at the photopeaks for electric field strengths of 10 to 30 V/μm. Good energy resolution is a desirable characteristic for any spectometer system because it permits precise identification and separation of γ-rays with very similar energies which is important for radionuclide identification or scatter rejection [9]. With the on-going trend in nuclear medicine to improve

energy resolution of gamma cameras, this has triggered the transition from the standard NaI scintillation cameras to state-of-the-art semiconductor cameras like CdZnTe. Although, in the peculiarities of this gamma camera for PBSI, high energy resolution does not offer any advantages from the lack of scattering processes observed in the GATE and PHS results. In turn, the implementation of a-Se in this gamma camera would provide the sensitivity and simplicity in the PHA hardware at a reasonably low cost.

There has been theoretical and experimental investigation of the process of photogenerated charge in a-Se [62-67]. This chapter investigates the electric field strength and temperature dependence on PHS signals with a-Se photoconductor. The presented results agree with the general consensus that within the band gap, there exist localized states, which governs the photoconversion process in a-Se. The peculiarities of photoconversion arise due to trapping and recombination. Recombination occurs not only between geminate pairs but also between other pairs created along their track. The mechanisms of EHP recombination are not fully understood [64]. Furthermore, as the photon energy increases, the generated EHPs grow farther apart and thus have a greater probability of escape, leading to a lower $W_{\pm}$ [64,71]. Experimentally, 10 V/μm is the lowest field strength where discernible PHS signals could be counted. The intrinsic limit of $W_{\pm}$ is only possible when these mechanisms are suppressed entirely. With higher electric field strength, and/or specialized structures to limit the noise levels in a-Se, the photoconductive properties can be improved further, making a-Se photoconductors even more desirable in their applications.

Chapter 4

Summary of thesis and future work

The permanent breast seed implantation treatment plan has been shown to be a promising alternative to traditional XRT for breast cancer patients. The aim of this thesis is to develop a novel imaging device for improving the treatment of breast cancer. As in other areas of brachytherapy, such as prostate seed implantation, there is a paradigm shift toward real-time implant optimization. Breast brachytherapy can only become successful if quality implants can be assured by appropriate image guidance. The establishment of PBSI as a standard breast cancer treatment with high quality control could potentially lead to improved quality of life for a significant fraction of all patients with breast cancer. We propose to use a-Se in a gamma camera system for low energy γ-ray detection. Since its current application in FPXIs are sensitive to x-ray mammography energies, very similar to those used in PBSI, it will provide a cost-effective and technological advantage over CdZnTe. The development cost of a selenium based prototype for breast brachytherapy would be relatively low because the current mammography technology can be used with significant simplification and FPXIs are quite flexible in their applications. This thesis employs two methods in examining the performance this a-Se PBSI imager: proof-of-principle using GATE simulation and PHS experiments to characterize the photoconversion gain of a-Se at low γ-ray energy.

GATE simulations were initialized for a typical PBSI procedure: a 60-seed distribution of ^{103}Pd in a phantom volume that mimics the breast of a patient. Results demonstrated a-Se could localize individual seeds to 1.35 mm in just 10 s, comparable to a simulation study with a CdZnTe camera system [6]. At 60 s, the a-Se photoconductor could detect almost $1x10^5$ γ-rays, similar to the expected collimator sensitivity of 1,626 cps. With the specifically designed collimator and a 200x200 μm pixel size, each pixel receives 4.2 cps which translates to 2,205 EHPs, for our measured $W_{\pm}$ of 41 eV from PHS. This is under the assumption the gamma camera operates at 10 V/μm, typical of FPXIs for digital radiography [22]. By increasing the bias to 30 V/μm, each pixel can achieve about 4000 EHP/s, with measured $W_{\pm}$ of 22 eV from PHS. The

collimator can provide a spatial resolution of 2.78 mm, thus, the spatial resolution of the detector was found to be 2.43 mm. In the energy data, Compton scattering is negligible, with ~7% of scattering associated with the phantom and ~0.6% in the a-Se layer. The count rate for scattered events is magnitudes lower than the photopeaks for ^{103}Pd emission spectrum of 20-23 keV.

In PHS, a-Se was able to distinguish the ^{241}Am energy signal of 60 keV from background electronics in less than 10 s. Important solid-state mechanisms such as EHP creation, dissociation and trapping governs the charge collection properties of a-Se based detectors. In measuring the $W_{\pm}$ using PHS, insight was provided into the charge collection peculiarities from electric field and temperature dependence. Increasing the applied electric field lowers $W_{\pm}$ and increases charge collection due to suppressed EHP recombination. The field dependence of $W_{\pm}$ in a-Se is mainly due to the initial recombination of EHPs and occurs mainly between electrons and holes in excitonic stage as opposed to band-to-band recombination. Temperature variations strongly affect the trap states and follow an Arrhenius dependence where the activation energy is the energy required for trapped charge to be released into the conduction band. By varying the electric field and temperature, an a-Se based gamma camera can achieve optimal charge collection at higher fields and room temperatures. With higher electric field strength, and/or specialized structures to limit the noise levels in a-Se, the photoconductive properties can be improved.

Fig. 3.25 demonstrates that even with low energy resolution simulated through GATE's energy blurring method, seeds can be resolved as Compton scattering is absent. In conclusion, poor intrinsic energy resolution of a-Se associated with high recombination is not a limiting factor for the implementation of a-Se photoconductive layer into a PBSI imager. This a-Se based gamma camera for breast brachytherapy has the advantage over CdZnTe due to the reduced cost. In such, the use of a-Se is a cost-effective solution to market an on-line gamma camera dedicated to PBSI imaging.

With the extensive capabilities of Geant4 and GATE software, there is always room for improvement for future work in developing this PBSI imager. With data from a PBSI treatment plan, one can setup a voxelized breast phantom in GATE to specify precisely the dose from a realistic breast implanted with ^{103}Pd seeds. Another option for the photoconductor is to initialize an electric field in the layer. In this thesis, the ionization potentials for the materials used were

specified which relates to the $W_{\pm}$ from our PHS experiments without specifying electric fields at all. If there is a method in GATE v6.1 or later versions to include an electric field, this would provide greater accuracy in results when simulating a highly field dependent photoconductor like a-Se. The 3D reconstruction of the seeds is another task which can be accomplished using a proper algorithm for combining spatial data from each of the two constructed detectors. Although this thesis takes a proof-of-concept approach to evaluate the performance of an a-Se gamma camera, it is a first step to initialize the development of such a device for clinical trials.

In relation to the actual PBSI procedure, there is a need to test this a-Se gamma camera before it is passed onto clinical trials. The simulated and PHS experiment data of this thesis provides a framework for building an a-Se gamma camera prototype for imaging ^{103}Pd seeds. With access to a realistic breast phantom, several ^{103}Pd seeds, a collimator and a-Se detector with electronics, the performance of this fully constructed gamma camera based on a-Se can be accurately evaluated in the lab. When this physical gamma camera is designed, the discriminator electronics can be greatly simplified since Compton scattering is negligible and thus energy discrimination is not of great importance.

Bibliography

1 Canadian Cancer Statistics, National Cancer Institute of Canada, Toronto, Canada, Tech. Rep., 2004.

2 Cancer Treatment and Survivorship Facts and Figures, American Cancer Society, Atlanta, Georgia, 2012.

3 M. Oldham, "Radiation physics and applications in therapeutic medicine," Physics Education, 460-467 (2001).

4 J.P. Pignol, B. Keller, E. Rakovitch, R. Sankreacha, H. Easton and W. Que, "First report of a permanent breast (103)Pd seed implant as adjuvant radiation treatment for early-stage breast cancer," Int. J. Radiat. Oncol. Biol. Phys., 64, 176-182 (2006).

5 P.J. Hoskin, K. Motohashi, P. Bownes, L. Bryant and P. Ostler, "High dose rate brachytherapy in combination with external beam radiotherapy in the radical treatment of prostate cancer: initial results of a randomised phase three trial," Radiotherapy and Oncology 84(2), 114–120 (2007).

6 A. Ravi, C.B. Caldwell, B.M. Keller, A. Reznik and J.P. Pignol, "Online gamma-camera imaging of ^{103}Pd seeds (OGIPS) for permanent breast seed implantation," Phys. Med. Biol., 2008.

7 G.F. Knoll, Radiation Detection and Measurement, 3rd ed. (John Wiley and Sons, New York, 2000).

8 B. Keller, et al., Int. J. Radiat. Oncol. Biol. Phys., 44, 789 –799 (1999).

9 S.R. Cherry, J.A. Sorrenson and M.E. Phelps, Physics in Nuclear Medicine, 3rd ed. (Saunders, Philadelphia, 2003).

10 S. Nath, Z. Chen, N. Yue, S. Trumpore, and R. Peschel, "Dosimetric effects of needle divergence in prostate seed implant using I and Pd radioactive seeds," Medical Physics, 27, 1058-1063 (2000).

11 G. Gilmore and J. Hemingway, Practical Gamma-Ray Spectrometry, (John Wiley and Sons, New York, 1995).

12 A.H. Goldan, K.S. Karim, A. Reznik, C. B. Caldwell and J. A. Rowlands, "Photon counting readout pixel array in 0.18-μ m CMOS technology for on-line gamma-ray imaging of ^{103}palladium seeds for permanent breast seed implant (PBSI) brachytherapy," in SPIE Medical Imaging 2008: Physics of Medical Imaging, abstract submitted.

13 T. Kikawa, A.K. Ichikawa, T. Hiraki and T. Nakaya, "Improvement of the energy resolution of CdTe detectors by pulse height correction from waveform," in Nucl. Instr. and Meth. A, abstract submitted, December, 2011.

14 D. Kopelman, I. Blevis, G. Iosilevsky, A. Reznik, A. Chaikov, N. Weiner, O. Israel and M. Hashmonai, "A newly developed intra-operative gamma camera: performance characteristics in a laboratory phantom study," Eur. J. Nucl. Med. Mol. Imaging, 32, 1217-1224 (2005).

15 I.M. Blevis, A. Reznik, G.Iosilevsky, O. Israel, D. Kopelman and M. Hashmonai, "Evaluation of a CdZnTe intra-operative gamma camera," IEEE Nuclear Science Symposium Conference Record 6, 3555-3558 (2004).

16 R.O. Bell, G. Entini, and H.B. Serreze, "Time-dependent polarization of CdTe gamma-ray detectors," Nucl. Instrum. Meth., 117, 267–271 (1974).

17 H. L. Malm and M. Martini, "Polarization phenomena in CdTe: preliminary results," Can. J. Phys., 51, 2336 (1973).

18 J.A. Heanue, D.A. Pearson and R.E. Melen, "CdZnTe detector array for a scanning-beam digital x-ray system," in Medical Imaging 1999, Proc. SPIE 3659, 718-725 (1999).

19 K.S. Karim, S. Yin, A. Nathan and J.A. Rowlands, "High dynamic range pixel architectures for diagnostic medical imaging," in SPIE Medical Imaging 2004, M. Yaffe, M. J. Flynn, Editors, 5368, 657-667 (2004).

20 J.A. Rowlands and J. Yorkston, "Flat panel x-ray imagers for digital radiography," Chapter 4 Medical Imaging vol. 1, Physics and Psychophysics, SPIE, (Bellingham, 2000).

21 J. A. Rowlands, D. M. Hunter and N. Araj, "X-ray imaging using amorphous selenium: a photoinduced discharge readout method for digital mammography," Med. Phys., 18, 421 (1991).

22 S. Kasap and J. Rowlands, "Direct-conversion flat-panel x-ray image sensors for digital radiography," Proceedings of the IEEE, 90(4), 591-604 (2002).

23 S. Kasap, J. Frey, G. Belev, O. Tousignant, H. Mani, L. Laperriere, A. Reznik, and J. Rowlands, "Amorphous selenium and its alloys from early xeroradiography to high resolution x-ray image detectors and ultrasensitive imaging tubes," Phys. Status Solidi, 246(8), 1794-1805 (2002).

24 M. Yaffe and J. Rowlands, "X-ray detectors for digital radiography," Phys. Med. Biol., 42, 1-39 (1997).

25 P. J. Papin and H. K. Huang, "X-ray sensitivity of halogenated a-Se: as photoreceptors for electroradiography," Med. Phys., 14, 322 (1987).

26 W. Zhao, I.M. Blevis, D.F. Waechter, Z. Huang and J.A. Rowlands. "Digital radiology using active matrix readout of amorphous selenium: construction and evaluation of a prototype real-time detector," Medical Physics, 24, 1834-1843 (1997).

27 K.S. Karim, A. Nathan and J.A. Rowlands, "Amorphous silicon active pixel sensor readout circuit for digital imaging," IEEE Transactions on Electron Devices, 50(1), 200-208 (2003).

28 K.S. Karim, et al., "Active pixel image sensor for large area medical imaging," in Medical Imaging 2003: Physics of Medical Imaging, L. Antonuk, M. Yaffe, Editors, SPIE, 5030(1), 38-47 (2003).

29 U. Neitzel, I. Maack and S. Günther-Kohfahl, "Image quality of a digital chest radiography system based on a selenium detector," Med. Phys., 25, 509 (1994).

30 K.S. Karim, A. Nathan and J.A. Rowlands, "Amorphous silicon pixel amplifier with V_T compensation for low noise digital fluoroscopy," in IEEE International Electron Devices Meeting (IEDM) Technical Digest, 215-218 (2002).

31 M. Li, M.S. Dixit and P.C. Johns, "Photon counting digital radiography using high-pressure xenon filled detectors," Nuclear Instruments and Methods in Physics Research A, 471, 215-21 (2001).

32 F. Arfelli, et al. "A linear array silicon pixel detector: images of a mammographic test object and evaluation of delivered doses," Physics of Medical Biology, 42, 1565-1573 (1997).

33 B. Mikulec, M. Campbell, E. Hiejne, X. Lopart and L. Tlustos, "X-ray imaging using single photon processing with semiconductor pixel detectors," Nuclear Instruments & Methods in Physics Research A, 511, 282-286 (2003).

34 P. Fischer, J. Hausmann, A. Helmich, M. Lindner, N. Wermes and L. Blanquart, "A counting pixel chip and sensor system for x-ray imaging," IEEE Trans. Nucl. Sci., 46 (4), 1070–1074 (1999).

35 C. Roennqvist, et al., "A 64-channel pixel readout chip for dynamic x-ray imaging," Presented at the 1996 IEEE Nuclear Science Symposium and Medical Imaging Conference, Anaheim, CA, 1996.

36 W. Sansen and Z. Chang, "Limits of low noise performance of detector readout front ends in CMOS technology," IEEE Trans. Circuits Syst., 37(11), 1375–1382 (1990).

37 A.H. Goldan, K.S. Karim and J.A. Rowlands, "Photon counting pixels in CMOS technology for x-ray imaging applications," Proc. IEEE CCECE, Saskatoon, Saskatchewan, 2005.

38 A.H. Goldan, K.S. Karim and J.A. Rowlands, "Single photon counter for digital x-ray mammography tomosynthesis," Journal of Vacuum Science and Technology A, 24(3), 854-859 (2006).

39 A.H. Goldan, K.S. Karim and J.A. Rowlands, "Selective photon counter for digital x-ray mammography tomosynthesis," in SPIE Med. Imag. 2006: Physics of Medical Imaging, Proc. SPIE, 6142, 1697-1705 (2006).

40 A. Goldan, L. Ng, J.A. Rowlands and K.S. Karim, "Photon counting pixel architecture for x-ray and gamma-ray imaging applications," in SPIE Medical Imaging 2007: Physics of Medical Imaging, abstract submitted, August 2006.

41 A.H. Goldan and K.S. Karim, "A low noise, high gain complementary folded cascode amplifier for photon counting systems," IEEE Transactions on Circuits and Systems I, revised version under review, September 2006.

42 M.P. Allen and D.J. Tildesley, Computer Simulation of Liquids, (Oxford University Press, New York, 1987).

43 R.Y. Rubinstein, Simulation and the Monte Carlo Method, (John Wiley and Sons, New York, 1981).

44 K. Binder, The Monte Carlo Method in Condensed Matter Physics, (Springer-Verlag, New York, 1992).

45 I. Buvat and I. Castiglioni, "Monte Carlo simulations in SPET and PET," Q. J. Nucl. Med., 46, 48-61 (2002).

46 R. Brun, F. Bruyant, M. Maire, A. C. McPherson and P. Zanarini, "GEANT3 Technical Report," CERN DD/EE 84(1), 1987.

47 S. Agostinelli, et al., "GEANT4 - a simulation toolkit," Nucl. Instr. Meth., 506, 250-303 (2003).

48 G. Santin, D. Strul, D. Lazaro, L. Simon, M. Krieguer, M. Vieira Martins, V. Breton and C. Morel, "GATE: A GEANT4-based simulation platform for PET and SPECT integrating movement and time management," IEEE Trans. Nucl. Sci., 50, 1516-1521 (2003).

49 D. Strul, G. Santin, D. Lazaro, V. Breton and C. Morel, "GATE (GEANT4 Application for Tomographic Emission): a PET/SPECT general purpose simulation platform," Nucl. Phys. B, 125(C), 75-79 (2003).

50 S. Jan, D. Benoit, E. Becheva, T. Carlier, F. Cassol, P. Descourt, et al., "GATE V6: a major enhancement of the GATE simulation platform enabling modelling of CT and radiotherapy," Phys. Med. Biol., 56, 881–901 (2011).

51 S. Staelens, D. Strul, G. Santin, M. Koole, S. Vandenberghe, Y. D'Asseler, I. Lemahieu and R. Van de Walle, "Monte Carlo simulations of a scintillation camera using GATE: validation and application modelling," Phys. Med. Biol., 48, 3021-3042 (2003).

52 D. Lazaro, I. Buvat, G. Loudos, D. Strul, G. Santin, N. Giokaris, D. Donnarieix, L. Maigne, V. Spanoudaki, S. Styliaris, S. Staelens and V. Breton, "Monte Carlo simulation of a CsI(Tl) gamma camera dedicated to small animal imaging using GATE," Phys. Med. Biol., 2003.

53 OpenGATE collaboration. GATE Users Guide V6., Retrieved May 24, 2012, from http://wiki.opengatecollaboration.org/index.php/Users_Guide_V6.

54 NIST Physical Measurement Laboratory, National Institute of Standards and Technology, US Dept. of Comm., Retrieved June 12, 2013, from http://physics.nist.gov/PhysRefData/Xcom/html/xcom1.html.

55 Collimators for Nuclear Medicine, Nuclear Fields, Van Mullekom Group, 2012.

56 Tissue Substitutes in Radiation Dosimetry and Measurement, Report 44, International Commission on Radiation Units and Measurements, (Oxford University Press, 1989).

57 Radionuclide Transformations Energy and Intensity of Emissions, International Commission on Radiological Protection, Report 38, (Pergamon Press, 1983).

58 O. Klein and Y. Nishina, "Scattering of radiation by free electrons according to Dirac's new relativistic quantum dynamics," The Oskar Klein Memorial Lectures, 2, 113–139 (1994).

59 J.H. Hubbell, W.J. Veigele, E. A. Briggs, R. T. Brown, D. T. Cromer and R. J. Howerton, "Atomic form factors, incoherent scattering functions, and photon scattering cross sections," J. Phys. Chem. Ref. Data, 4, 471 (1975).

60 H. Bethe and J. Ashkin, Experimental Nuclear Physics, (John Wiley and Sons, New York, 1953).

61 J.H. Scofield, "Theoretical photoionization cross sections from 1 to 1500 keV," Lawrence Livermore National Laboratory Rep. UCRL-51326 (1973).

62 I.M. Blevis, D.C. Hunt and J. A. Rowlands, "Measurement of x-ray photogeneration in amorphous selenium," J. Appl. Phys. D., 85(11), 7958 (1999).

63 H. Overhof and P. Thomas, Electronic Transport in Hydrogenated Amorphous Semiconductors, (Springer-Verlag, Berlin, 1989).

64 M. Lachaine and B.G. Fallone, "Monte Carlo simulations of x-ray induced recombination in amorphous selenium," J. Appl. Phys. D., 33, 1417–1423 (2000).

65 W. Que and J.A. Rowlands, "X-ray photogeneration in amorphous selenium: geminate versus columnar recombination," Phys. Rev. B., 51, 10500 (1995).

66 A. Darbandi, É. Devoie, O. Di Matteo and O. Rubel, "Modeling the radiation ionization energy and energy resolution of trigonal and amorphous selenium from first principles," J. Phys. Condens. Matter, 24(45), 5502 (2012).

67 I.M. Blevis, D.C. Hunt and J. A. Rowlands, "X-ray imaging using amorphous selenium: determination of Swank factor by pulse height spectroscopy," Med. Phys., 25(5), 2405 (1998).

68 R. Casanovas, J.J. Morant and M. Salvado, "Energy and resolution calibration of NaI(Tl) and $LaBr_3$(Ce) scintillators and validation of an EGS5 Monte Carlo user code for efficiency calculations," Phys. Res. A, 675, 78-83 (2012).

69 C.B. Hruska and M.K. O'connor, "CZT detectors: How important is energy resolution for nuclear breast imaging?," Phys. Med. Biol., 21, 72 (2006).

70 J. Rowlands and S. Kasap, "Amorphous semiconductors usher in digital x-ray imaging," Physics Today, American Institute of Physics, 50(11), 24 (1997).

71 S. Kasap, J.B. Frey, G. Belev, et al., "Amorphous and polycrystalline photoconductors for direct-conversion flat panel x-ray image sensors," Sensors, 11, 5112-5157 (2011).